NOAA Technical Memorandum ERL NSSL-89

A STUDY OF HAIL PRODUCTION IN A SUPERCELL STORM USING A DOPPLER DERIVED WIND FIELD AND A NUMERICAL HAIL GROWTH MODEL

Stephan P. Nelson

National Severe Storms Laboratory
Norman, Oklahoma
December 1980

UNITED STATES DEPARTMENT OF COMMERCE
Philip M. Klutznick, Secretary

NATIONAL OCEANIC AND ATMOSPHERIC ADMINISTRATION
Richard A. Frank, Administrator

Environmental Research Laboratories
Joseph O. Fletcher, Acting Director

TABLE OF CONTENTS

LIST OF ILLUSTRATIONS

LIST OF TABLES

LIST OF SYMBOLS

(exclusive of appendices)

A	Amplitude of cosine function used to simulate a noisy divergence field
A_c	Cross sectional area of hailstone
a	Ventilation coefficient
C_D	Hailstone drag coefficient
C_{pi}	Specific heat at constant pressure for ice
C_{pw}	Specific heat at constant pressure for water
D	Hailstone diameter
D_o	Initial embryo diameter
d_i	Diffusivity of water vapor in air
E_I	Error due to use of trapezoidal rule numerical integration technique
E_i	Ice collection efficiency (collision & coalescence efficiency)
E_w	Water collection efficiency (collision & coalescence efficiency)
F_f	Fraction of accreted water frozen
K	Thermal conductivity of air
L	Wavelength of cosine function used to simulate a noisy divergence field
L_f	Latent heat of fusion
L_s	Latent heat of sublimation
L_v	Latent heat of vaporization
M	Total collected ice and accreted water mass
M_i	Collected ice mass
M_w	Accreted water mass
M_{wu}	Mass of accreted but unfrozen water
M_H	Hailstone mass
dQ_c/dt	Rate of heat change due to conduction

$dQ_{e,s}/dt$	Rate of heat change due to evaporation or sublimation
dQ_i/dt	Rate of heat change due to collected ice
dQ_T/dt	Total rate of heat change of hailstone
dQ_w/dt	Rate of heat change due to accreted water
R_e	Reynolds number
$\vec{R}_i$	Radius vector from radar "i" to the tracer
r_i	Environmental ice water content per unit volume
r_w	Environmental cloud water content per unit volume
T_a	Ambient temperature
T_i	Temperature of collected ice
T_s	Temperature of hailstone surface
T_w	Temperature of accreted water
u	West-east component of motion
$\vec{V}$	Tracer velocity
V_i	Projection of tracer velocity onto radius vector (R_i)
V_T	Hailstone terminal velocity
v	South-north component of motion
W_n^C	Vertical velocity computed at level "n" from triple Doppler analysis
w	Vertical component of motion
x	West-east Cartesian distance
y	South-north Cartesian distance
Z_e	Equivalent radar reflectivity factor
z	Vertical cartesian distance
ε^B	Error in triple Doppler computed vertical velocity due to an erroneous boundary condition
ε^I	Error in triple Doppler computed vertical velocity due to incorrectly integrating $\rho\nabla\cdot v$ with height
ε^N	Error in triple Doppler computed vertical velocity due to numerical integration inaccuracies

ξ	Height at which trapezoidal rule errors maximizes
ρ_a	Ambient water vapor density
ρ_e	Environmental air density
ρ_H	Density of hailstone
ρ_s	Water vapor density over the hailstone surface
ϕ_i	Elevation angle of radar "i"
ω	Tracer vertical component of motion $\omega = w+V_T$
∇	Horizontal divergence operator ($\nabla = \frac{\partial}{\partial x} + \frac{\partial}{\partial g}$)

This report was also a thesis accepted by the University of Oklahoma in partial fulfillment of requirements for the degree of Doctor of Philosophy.

ABSTRACT

An investigation is made into the hail production characteristics of a supercell-type storm that occurred in Central Oklahoma on 29 May 1976. The main research tool employed is a three dimensional numerical hail growth model with the flow field being taken directly from a triple Doppler synthesis. The Doppler data set from this storm is not ideal in that velocities are missing from one or more radars at both the lowest and highest storm levels. In addition, the storm is not geographically well situated with respect to the radars for a triple Doppler synthesis. These factors have little influence in deriving the horizontal flow, but have a major inpact on the computed vertical velocities. Following an extensive error analysis, general procedures are developed to minimize errors in computed vertical velocity. These techniques are computationally fast and are especially well suited for cases with incomplete and/or low quality data.

Storm reflectivity and horizontal flow structure are very similar to those reported for previously studied supercell storms. Near the surface, there is a circulation about a vertical axis with its attendant hook echo. A weak echo region is present at middle levels, and strong divergence causing a large overhang characterizes the highest storm regions. The vertical drafts, however, are more complex than envisioned by conceptual models. The classical updraft/downdraft couplet (extremes of +51 m s^{-1} at 7 km and -25 m s^{-1} at 5 km) dominates the storm complex, but there are other significant subsidiary vertical drafts. These are primarily associated with flanking line cells that form on the storm's gust front boundary.

The hail growth model reveals that embryos which experience significant growth can originate from various locales. Likely sources are hydrometeors from upper level outflows of both flanking line cells and the main updraft. Typically, any embryo that enters an updraft will experience some growth. Those which achieve greatest growth, however, are the ones which remain balanced in the principal growth zone (6 to 8 km) for the longest time periods. In the numerical model, this critical equilibrium occurs where the horizontal gradient of increased terminal velocity (i.e., mass) nearly balances the positive horizontal gradient of vertical velocity as the hailstones traverse the updraft. The model shows this balance is achieved coincident with the measured reflectivity maximum known previously as the "embryo curtain." It appears this area actually demarcates the region of maximum hail growth rather than embryo production and is, therefore, relabeled as the "hail curtain."

Some model embryos grow to large diameters (~5 cm) while their immediate neighbors do not. Due to an ideal set of circumstances the former grow wet in a mixed-phased region. Growth, therefore, occurs at a faster rate than it would if the cloud water were all liquid, since there is no latent heat of fusion associated with the collection of ice crystals. This points out the possible importance of the generally ignored role of ice crystal collection in hail growth.

Results of the model have implications for the three seeding techniques of artificial hail suppression, associated with glaciation, competition, and trajectory lowering, respectively. Glaciation is considered difficult because of the large amount of seeding material required. Use of the "hail curtain" as an indicator of the region where greatest growth occurs, however, may allow the seeding material to be used more efficiently. The model is even less encouraging for the success of beneficial competition since the natural embryos appear to originate from many

different locations making the targeting of seeding material extremely difficult. Trajectory lowering holds some promise. The numerical model shows areas below the prime growth zone where embryos would grow to moderate sizes. A sufficient number of artificially induced embryos injected into this location might deplete enough liquid water to keep large hail from forming at the higher levels.

A STUDY OF HAIL PRODUCTION IN A SUPERCELL STORM USING A DOPPLER DERIVED WIND FIELD AND A NUMERICAL HAIL GROWTH MODEL

1. INTRODUCTION AND BACKGROUND

1.1 Introduction

To most city dwellers a hailfall is no more than a matter of casual interest unless it is unusually severe. For people involved in agribusiness, however, even small hail can have ruinous effects. Crop loss in the United States alone is estimated at about three-quarters of a billion dollars annually with property damage adding about another 10% (1975 dollars; Changnon et al., 1977). The hail problem is far from being unique to this country. To name just a few notable examples, the wheat belt of Russia, some wine grape districts of Italy (Morgan, 1973), and the tea growing area of Kenya (Alusa, 1976) suffer especially heavy damage. Present day knowledge of likely modification methods and the extensive crop damage indicate potentially favorable cost-to-benefit ratios for hail suppression (Borland, 1977).

Hail suppression is hardly a new idea. Attempts have ranged from mystical efforts by ancient civilizations (Morgan, 1973), to use of explosive rockets (Sansom, 1968), to seeding techniques using mainly silver or lead iodide (Sax et al., 1975; Federer, 1977) but overall the efficacy of hailstorm modification has yet to be clearly demonstrated (Sax et al., 1975). Atlas (1977) proposed that one reason for the confusing results from past projects is that a given seeding technique may affect hailstorms with different dynamic structures in different ways. Certainly it is necessary to understand a storm's thermal, moisture, and wind structures in order to determine how hail is produced. It is precisely this knowledge which is lacking.

In this dissertation an investigation is made into the hail production characteristics of what is considered to be the most prolific hail producer--the supercell storm. This is accomplished via a case study of a severe hailstorm that produced 5 cm diameter hail.

Two major tools are necessary for the investigation. The first is a triple Doppler wind analysis. A new synthesis technique for obtaining vertical velocities is developed after an extensive error analysis. This technique is computationally fast and is well suited for the not infrequent circumstance when the Doppler data is of low quality and/or incomplete. The second tool is a numerical hail growth model. It employs the continuous collection process and allows the storm's thermal and moisture fields to vary in all three spatial dimensions. The Doppler synthesis and numerical model are described in Chapters 2 and 3, respectively.

Chapter 4 describes the storm's reflectivity and velocity fields. Overall the storm's structure is similar to previous conceptual models. There are, however, interesting substructures in the vertical velocity field.

In Chapter 5, results of the hail model calculations are presented. In the last chapter these computed hail growth characteristics are compared to previous models along with a discussion on the implications for modification.

1.2 Background: The Hail Production Process-- Theory and Observations

1.2.1 Microphysics

Basic hailstone growth characteristics have been known for some time from studies of internal hailstone structures and applications of microphysical growth equations (e.g., Shuman, 1938, Ludlum, 1958; Macklin, 1963). The initial growth unit is usually a frozen drop or graupel particle about 5 mm in diameter (Knight and Knight, 1970). Origins of these particles are still a matter of speculation. Bulk statistical evidence on embryo types shows that approximately 60% of Oklahoma embryos are frozen raindrops while 20% are graupel with the rest unknown (Knight and Knight, 1978).

Usually, but not always, there is a distinct growth boundary between the embryo and the hailstone. In fact, hailstones are often characterized by several such boundaries. Figures 1a and 1b show a thin section of a hailstone (about 0.5 mm thick) as seen both under ordinary light and between crossed polarizing filters. The embryo in Fig. 1 is unusually large and would be classified as a "frozen drop" (Knight, 1980). It is bounded by the thin layer of bubbly ice in Fig. 1a, or the first ring of very small crystals in Fig. 1b. The crack in the drop running from upper left to lower right also defines the embryo's dimensions. Exterior to the embryo the ordinary light photograph shows alternate layers of clear and opaque ice. The latter is caused by many small bubbles embedded within the ice structure.

Crossed polaroids are used to obtain a view of the hailstone's crystalline structure. Areas displaying the same crystalline orientation appear as regions of constant shading. For example, in Fig. 1b the embryo contains relatively large crystals; whereas, the remainder of the hailstone exhibits alternate layers of medium and small crystals.

In general, it has been shown that clear ice and large crystals are associated with what is termed "wet" growth and opaque ice and small crystals are indicative of "dry" growth (Levi and Aufdermaur, 1970; Carras and Macklin, 1975; Knight et al., 1978). It is obvious from thin sections like that shown in Fig. 1, that hailstones usually experience several changes in their growth environment.

The concepts of wet and dry growth are associated with one of the most critical hailstone growth factors--the heat budget. Hailstones grow mainly by accreting supercooled water. Heat release associated with freezing this water is quite substantial. If the hailstone can dissipate all this released heat, then dry growth occurs. Any net heat gain merely raises the temperature of the hailstone's surface. If, however, all the heat cannot be dissipated, the hailstone surface temperature remains at 0°C and some accreted water remains unfrozen. This unfrozen water may either be shed or remain with the hailstone in cavities.

The occurrence of wet growth has important implications. First of all, it suggests a growth inefficiency. That is, the hailstone cannot accrete all the water it encounters. This is relevant to modification via liquid water depletion since, for a hailstone experiencing wet growth, a decrease in available liquid water does not guarantee a decrease in hail mass. Another factor often overlooked is that ice crystals are readily collected by a hailstone undergoing wet growth. Ice crystal collection may, therefore, be important in mixed phase areas where hailstones are undergoing wet growth.

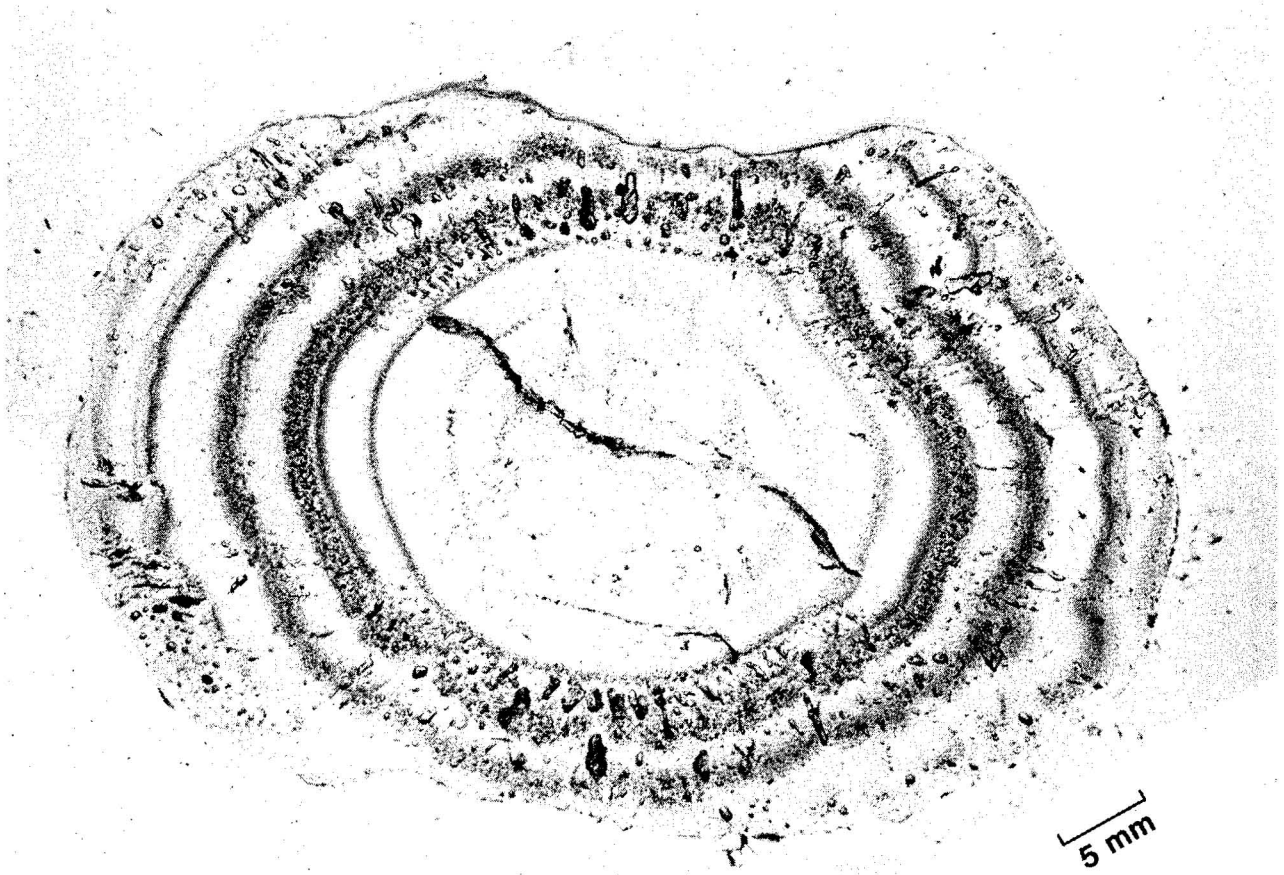

(a)

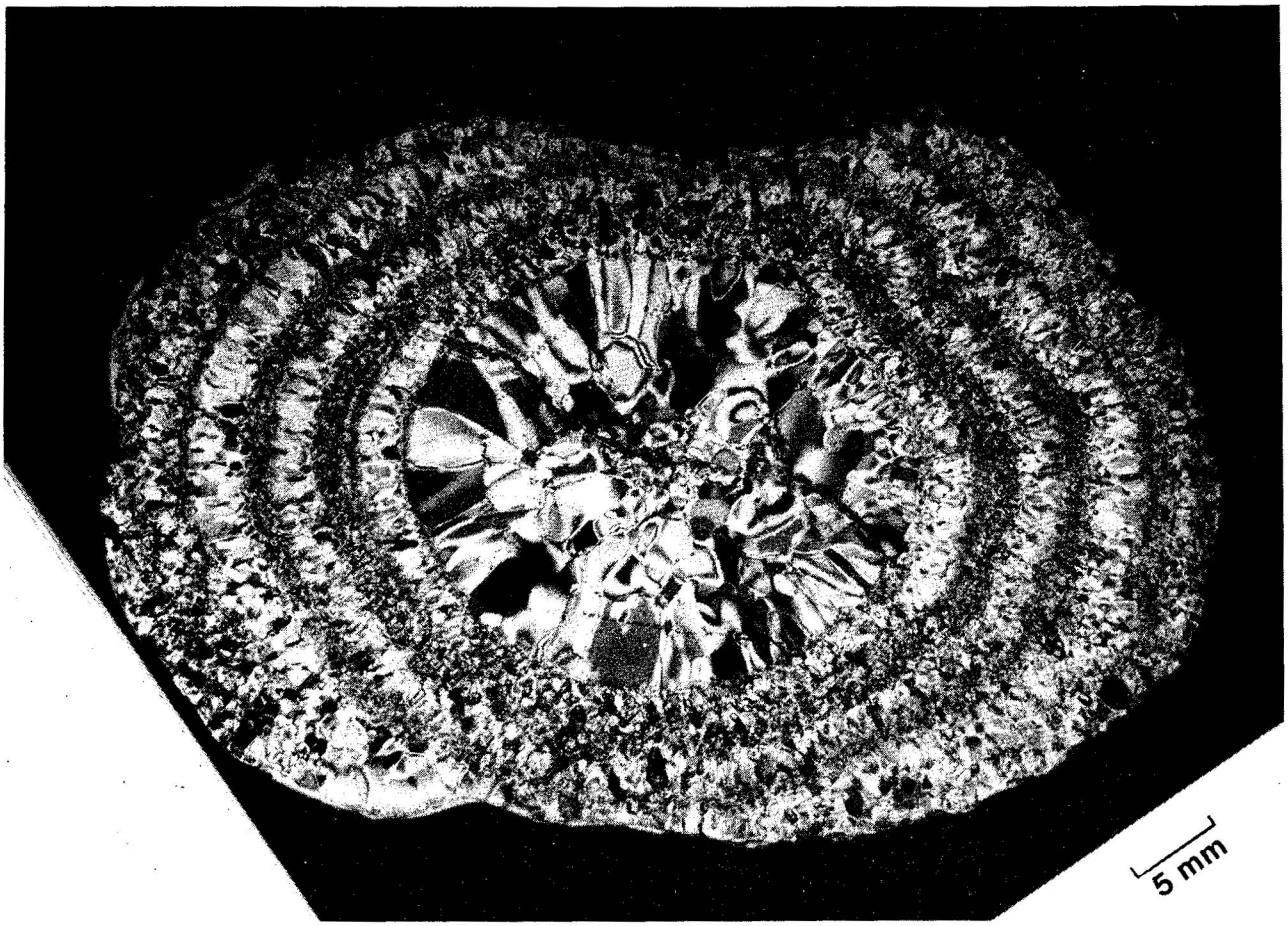

(b)

Figure 1. Thin sections of hailstones: (a) normal light, (b) between crossed polaroid filters. Photographs are courtesy of Nancy C. Knight.

In summary, while it can be said that individual hailstones have complex growth histories, the basic ingredients necessary to form large hail are well known. These are embryos, high liquid water content (or, if the hailstone is growing wet, high ice water content), and cold temperatures. Unanswered, however, is the question of how the storm organizes all these factors to provide growth areas suitable for large hail production.

1.2.2 Hailstorm Structures

Generally speaking, hailstorms are classified into two basic structures--ordinary cell and supercell (see Browning, 1977; Marwitz, 1972a,b,c; Chisholm and Renick, 1972). The ordinary cell has about a 30 min lifetime and evolves through three stages--cumulus, mature, and dissipating (Byers and Braham, 1949; Fig. 2). In the cumulus stage the storm is actively growing and consists almost entirely of updraft. Eventually the produced precipitation and entrainment form a downdraft in part of the storm. This period when there is a mixture of updraft and downdraft is called the mature stage. Finally, as entrainment and precipitation loading increase and the updraft is cut off by the downdraft, the dissipating stage begins. This stage is characterized by weak downdrafts throughout the storm with the low level outflow boundary forming a preferred

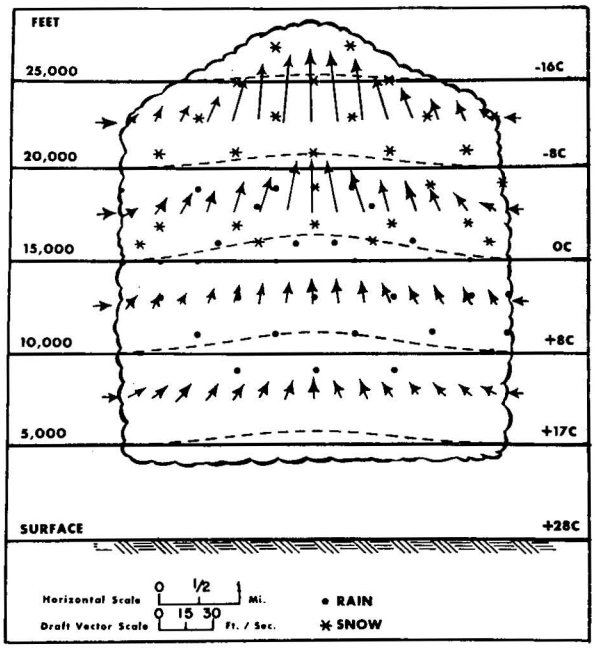

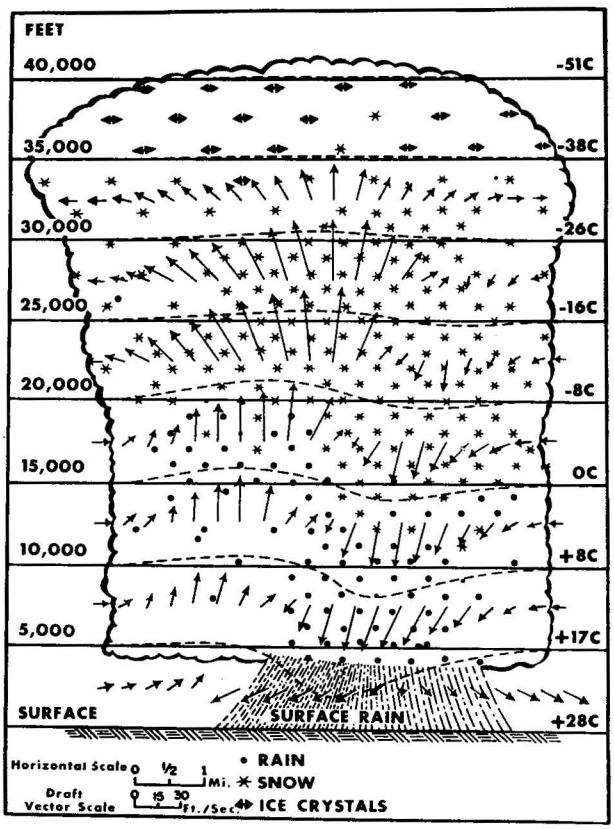

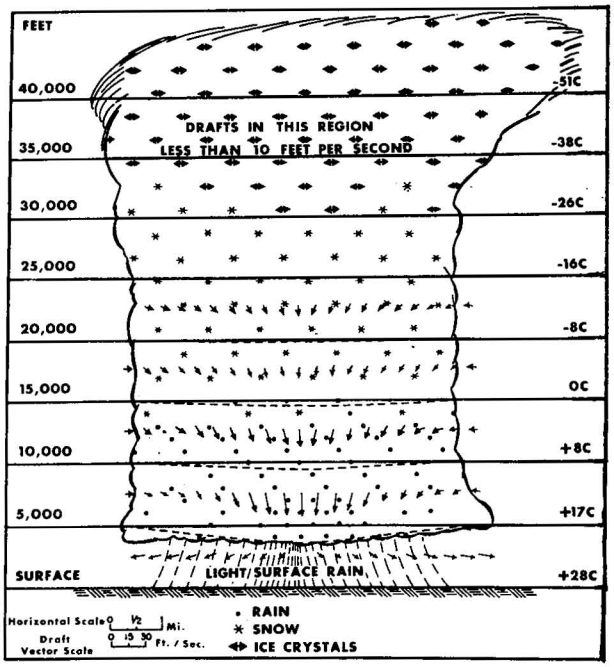

Figure 2. Stages in the lifetime of an ordinary cell (after Byers and Braham, 1949). Top right: cumulus stage; bottom right: mature stage; bottom left: dissipating stage.

region for the growth of subsequent cells. Often these new cells form in a random manner giving rise to a scattered pattern of "single" cell storms.

For reasons yet to be completely determined but believed to be associated with environmental winds, a new cell will sometimes form in a consistent location with respect to the old cell. As each cell grows and decays, it advects with the mean environmental winds. A new cell then forms on the upwind side of the old one on the outflow boundary, resulting in a succession of ordinary cells in various stages of development aligned with the mean environmental winds. This structure has been referred to in the literature as a multicell storm.

Supercell storms were first recognized as entities because of their unusual severity and distinctive appearance on radar. Nelson and Young (1979) showed that the average Oklahoma supercell storm produces larger hail (mean maximum diameter of 4.4 cm) over larger areas (mean maximum swath width 18.1 km) than their ordinary cell counterparts (means of 1.4 cm and 8.1 km, respectively). As described by Browning (1977), the distinguishing dynamical feature of a supercell is believed to be an updraft/downdraft couplet ". . . coexisting symbiotically for a long period (30 min or more)." Figure 3a shows a conceptual two-dimensional vertical section of the updraft/downdraft in a supercell storm (after Browning and Foote, 1976). It is generally thought that the drafts are sloped so that the downdraft

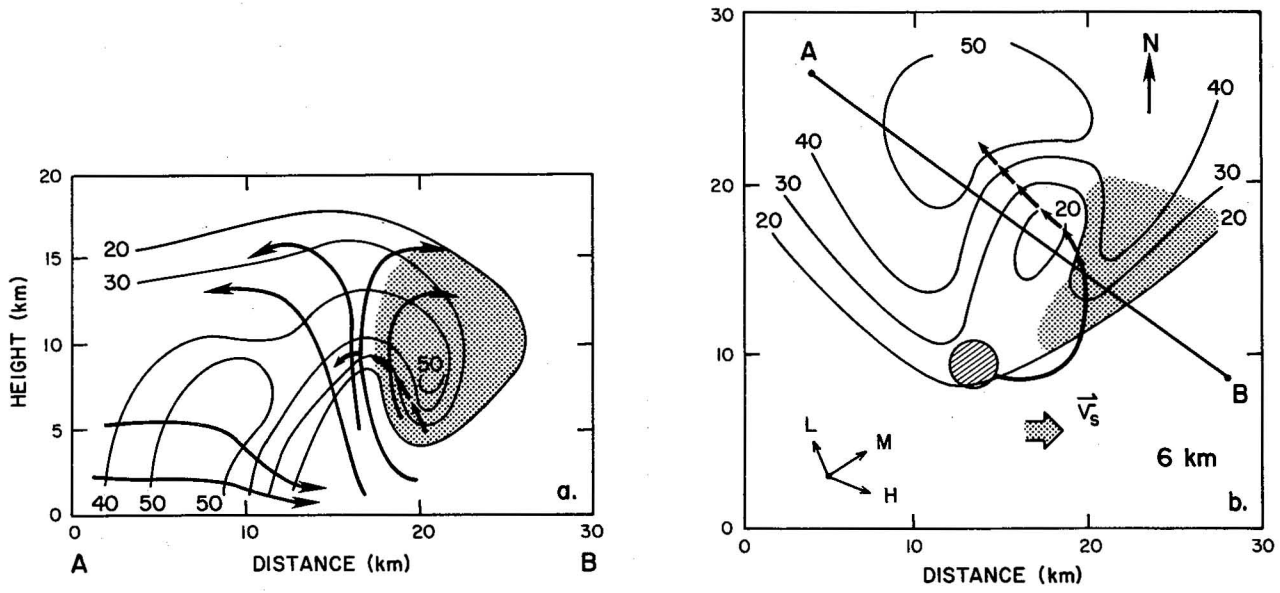

(a) (b)

Figure 3. Vertical (a), horizontal (b), and three-dimensional perspective views (c) of Browning and Foote's (1976) conceptual hailstorm model. Light lines represent the reflectivity factor contoured every 10 dBz. Continuous heavy black lines with arrowheads in (a) are streamlines relative to storm motion (V_s in (b)). Shaded areas in (a) and (b) show the "embryo curtain." Cross-hatched area in (b) is embryo source region with the associated solid line with arrowhead showing plan position of embryo trajectory. This trajectory is also displayed in (c) by the line $\overline{E_1E_2}$. Hail growth trajectories are shown by short lines with arrowheads in (a) and (b) and by line $\overline{E_2H}$ in (c). Note in (c) trajectories hidden by planes appear as dashed lines. Environmental winds relative to storm motion at low (L), middle (M), and high (H) levels are shown by the labeled solid arrows in (b). The location of vertical section AB is shown in (b).

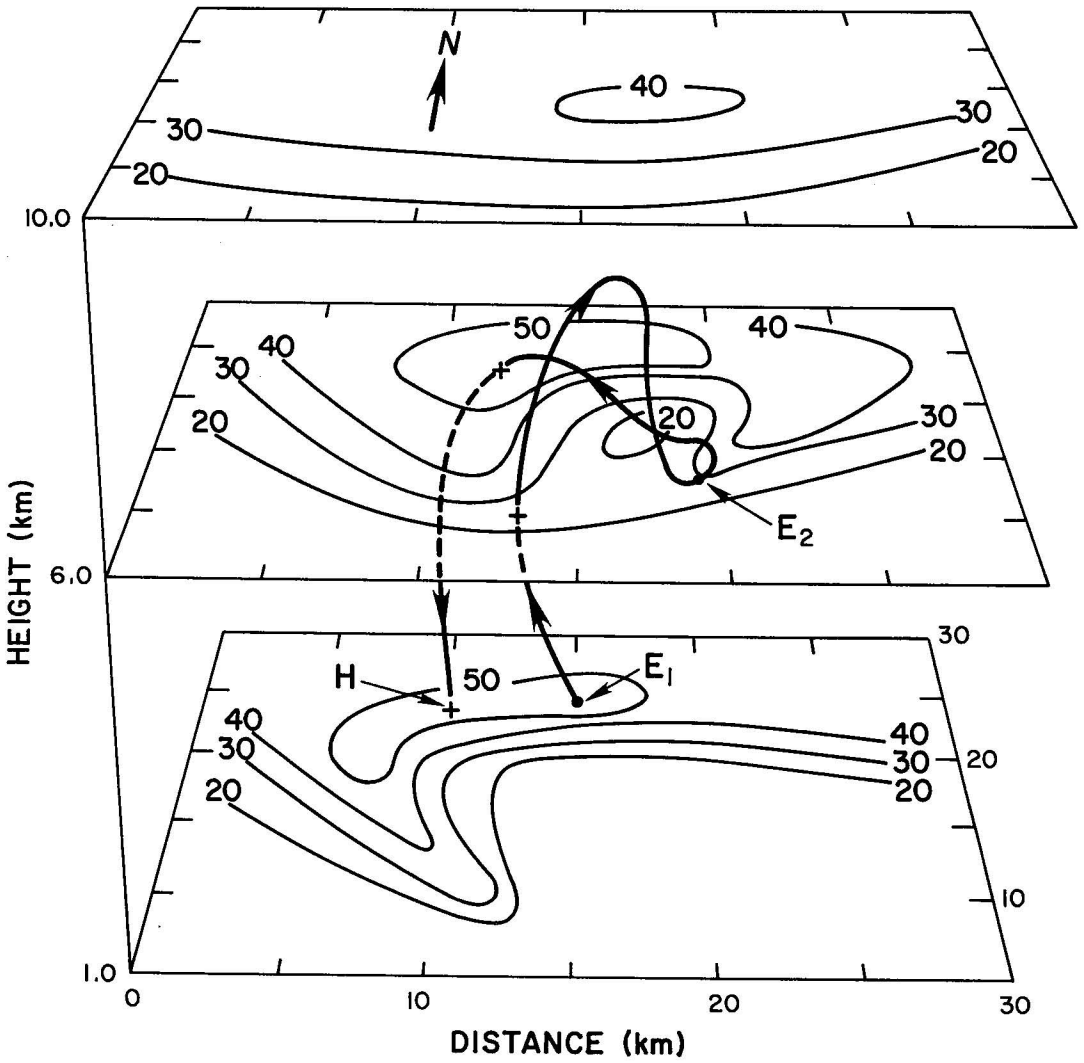

(c)

undercuts the updraft but many structural details are still a matter of conjecture due to a lack of direct evidence. Questions also exist pertaining to the origin, evolution, and steadiness of this flow structure (e.g., Nelson and Braham, 1975; Barge and Bergwall, 1976; Lemon and Doswell, 1979). Nonetheless it is this updraft/downdraft couplet coexisting for long periods of time that differentiates the dynamic structure of the ordinary and supercell storms.

There have been many fine numerical models both of microphysical hail growth processes (e.g., Danielsen et al., 1972; Young, 1978) and of hailstorm dynamics (e.g., Takeda, 1971; Wilhelmson and Klemp, 1978). Computer limitations, however, have prevented a melding of detailed microphysics and storm dynamics into one three dimensional simulation. To study hail growth with respect to storm dynamics previous modelers typically have simplified the microphysics, parameterized the dynamics and reduced the analysis domain to two dimensions (English, 1973; Musil et al., 1975; Sartor and Cannon, 1977). Two studies have made use of Doppler measured wind fields in a three-dimensional framework--Paluch, 1978; Orville et al., 1979. Both dealt with ordinary cell Colorado hailstorms which existed in environments with relatively low adiabatic water contents (surface mixing ratios of 9 g kg^{-1} or less). To date there have been no similar studies of supercell storms.

While no three dimensional numerical models have dealt with hail growth in a supercell storm, a conceptual model based on equivalent reflectivity factor[1] measurements has been synthesized by Browning and Foote, 1976. They propose embryos of the largest hail form between about 5 and 10 km at the upwind stagnation point between the storm and the environmental flow. This region is located at and above the cross-hatched circle in Fig. 3b. In our example, the embryos are advected northeastward or eastward in the middle and upper level flow as shown in plain view by the solid line in Fig. 3b and in three-dimensional perspective between $\overline{E_1E_2}$ in Fig. 3c. As the embryos are transported away from the updraft, they sink and re-enter the updraft at lower levels. This process is termed "injection" of embryos into the hail growth region. Browning and Foote suggest the embryos that produce large hail re-enter the updraft at a fairly low height (6 km). They consider this low trajectory necessary for achieving the balance between updraft speed and embryo terminal velocity, thus preventing the rapid transition of the particles to areas of colder temperatures. Because of the hypothesized presence of embryos, they have termed the high reflectivity area to the east of the updraft the "embryo curtain" (see shaded areas of Fig. 3a and 3b). Browning and Foote propose the largest hail is produced by embryos that advect away from the embryo curtain and over the weak echo region (dashed lines with arrowheads in Figs. 3a and 3b, and $\overline{E_1H}$ in Fig. 3c).

1.2.3 Dissertation Objectives

This dissertation's central theme is the study of hail growth in the context of the kinematical structure of a supercell type storm. Important topics in the hail production process are: embryo sources, embryo growth, embryo injection regions, hailstone growth, and hailstone melting. This work will study embryo injection regions and hail growth using Doppler derived three-dimensional flow fields from a supercell storm in conjunction with a numerical hail growth model. Specifically, the following will be addressed:

1) Comparing measured storm kinematic flow field to the Browning-Foote model.

2) Speculating on embryo growth and sources.

3) Identifying growth trajectories of large hail.

4) Determining important growth parameters along computed trajectories including:

   a) Learning how the storm's wind, thermal, and moisture structures interact to produce favorable growth areas.

   b) Identifying areas of maximum growth.

   c) Identifying relative importance of hailstone - supercooled water versus hailstone - ice crystal growth.

5) Modifying conceptual models of hail growth in supercell storms.

6) Speculating on possible effects of present day modification techniques on supercell storms.

---

[1] Hereafter this quantity will be called reflectivity.

To reiterate, the following two chapters contain details of the Doppler synthesis and hail growth model. Some readers may wish to proceed directly to the chapters containing the storm structure (4), hail growth calculations (5), and discussion (6).

2. ANALYSIS WITH THREE DOPPLER RADARS

2.1 Introduction

The first ingredient necessary for computing hail trajectories is accurate three-dimensional air velocities. Previous investigators using data from two or more Doppler radars have been successful at deriving storm horizontal flow fields (e.g., Brown and Peace, 1968; Lhermitte, 1970; Kropfli and Miller, 1975; Brown et al., 1975; Ray et al., 1975; Brandes, 1977; Burgess et al., 1977; Heymsfield, 1978; Ray et al., 1978; Ziegler, 1978). Obtaining vertical velocities has proven to be more difficult. There are two techniques for calculating the vertical velocity from Doppler data. The more useful of the two methods for severe storm research involves using the measured horizontal flow and the continuity equation. The vertical velocities calculated in this way, however, can become unrealistic through accumulation of small errors at each integra-tion step (Ray and Wagner, 1976; Burgess et al., 1977; Kelly et al., 1978; Ziegler, 1978). O'Brien (1970) attempted to correct this problem for rawinsonde data by using a constraint on the vertical velocity at the top integration limit and the calculus of variations (Sasaki, 1958). A similar technique was applied to Doppler data by Ray et al. (1978) and Ziegler (1978).

The technique of integrating upwards and applying the constraint at the top does have some drawbacks, however. Unless the data is continuous from the surface to the storm top (where the updraft is assumed negligible) adjusted vertical velocities are not possible. In fact, for regions such as "echo overhangs" no solution at all is possible.

The purpose of this chapter is twofold. First, it presents a detailed investigation of potential sources of errors in computing the updraft from continuity. Using this information, data handling and solution techniques are devised to minimize these errors. It is shown that downward integration is inherently superior to upward integration unless one is interested in only the lowest few kilometers. This is especially true when data does not extend through the entire vertical column. These points are illustrated using both actual and simulated data generated from analytical functions.

2.2 Basic Equations

Assuming the earth is a flat plane and using the geometry in Fig. 4, the dot product of the radius vector from radar "i" with the tracer velocity yields (Armijo, 1969):

$$\vec{R}_i \cdot \vec{V} = R_i V_i = ux_i + vy_i + \omega z_i \qquad (1)$$

With three noncolinear radars (i=1,2,3), the following 3 x 3 matrix

$$\begin{bmatrix} x_1 & y_1 & z_1 \\ x_2 & y_2 & z_2 \\ x_3 & y_3 & z_3 \end{bmatrix} \begin{bmatrix} u \\ v \\ \omega \end{bmatrix} = \begin{bmatrix} v_1 R_1 \\ v_2 R_2 \\ v_3 R_3 \end{bmatrix} \tag{2}$$

can be solved to yield

$$\begin{bmatrix} u \\ v \\ \omega \end{bmatrix} = \frac{1}{\chi} \begin{bmatrix} (y_2 z_3 - y_3 z_2) & (y_3 z_1 - y_1 z_3) & (y_1 z_2 - y_2 z_1) \\ (x_3 z_2 - x_2 z_3) & (x_1 z_3 - x_3 z_1) & (x_2 z_1 - x_1 z_2) \\ (x_2 y_3 - x_3 y_2) & (x_3 y_1 - x_1 y_3) & (x_1 y_2 - x_2 y_1) \end{bmatrix} \begin{bmatrix} V_1 R_1 \\ V_2 R_2 \\ V_3 R_3 \end{bmatrix} \tag{3}$$

where

$$\chi = x_1(y_2 z_3 - y_3 z_2) - y_1(x_2 z_3 - x_3 z_2) + z_1(x_2 y_3 - x_3 y_2)$$

There are only two nonfinite solutions to Eq. (3). The first occurs when the solution point is exactly colocated with one of the radar positions ($x_i = y_i = z_i = 0$). This is, of course, not possible since data could not exist there from all three radars. The second case occurs in the unlikely event that all three radars and the data to be analyzed are located at the same height (hence $z_1 = z_2 = z_3 = 0$).

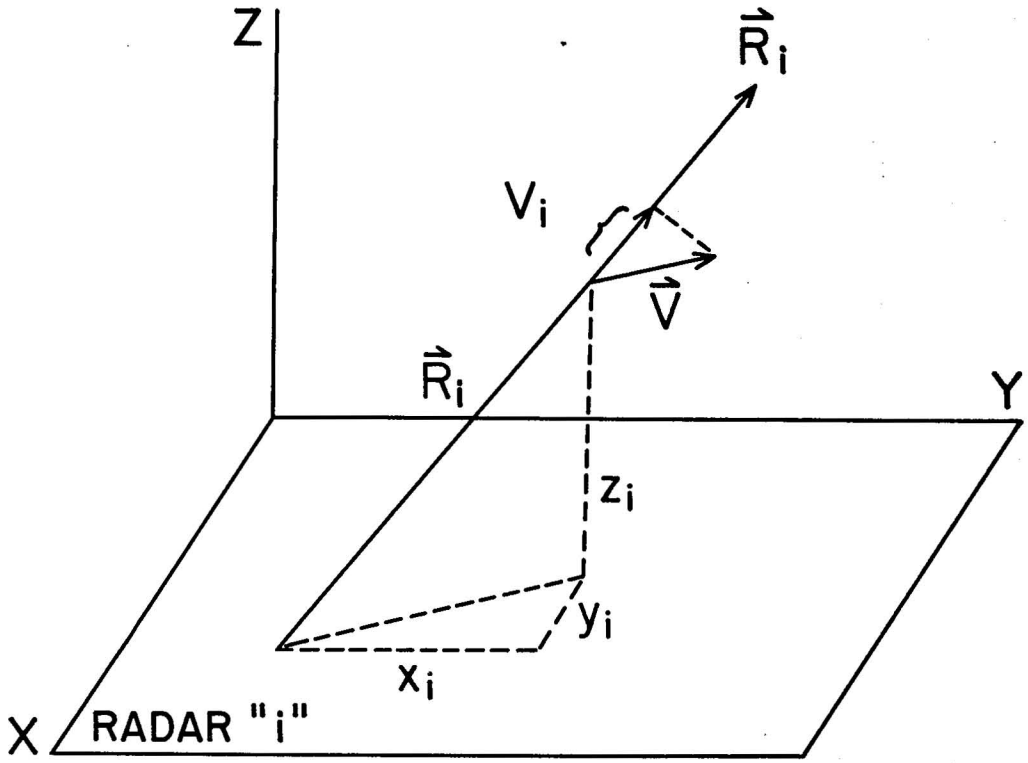

Figure 4. Relationship between radar "i" and tracer velocity $\vec{V}$ at data point x_i, y_i, z_i with respect to the radar. $\vec{R}_i$ - radius vector to the data point; V_i - radial velocity measured by radar.

2.3 Geometric Considerations

Fairly extensive analyses relating radial velocity accuracy, radar/data geometry, and derived wind field accuracy have been presented by Bohne and Srivastava (1975), Doviak et al. (1976) and Ray et al. (1978). For example, Fig. 5 (after Ray et al., 1978) shows the standard deviation of horizontal wind uncertainty for a model triple Doppler network. Actual values are not important to this discussion since they are dependent upon individual radar and analysis characteristics. The significant point is that accuracy in the horizontal velocity deteriorates with distance from the center of the triple Doppler triangle. It should be remembered that only Doppler sampling problems were considered in deriving these error curves. Other error sources such as amplitude changes due to interpolation or filtering, and hardware or software problems will further degrade the analysis.

Calculations have shown the geometry problem to be even more acute for ω. This can be simply shown by using Eq. (1) and letting u=v=0. Assuming the geometry shown in Fig. 6, ω is given by:

$$\omega = \frac{V_i}{\sin(\phi_i)} \qquad (4)$$

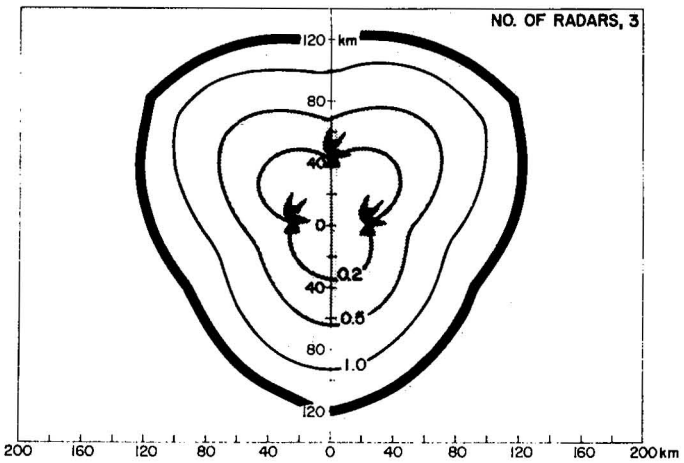

Figure 5. Standard deviation of horizontal wind uncertainty (m s^{-1}) for a model triple Doppler network (after Ray et al., 1978).

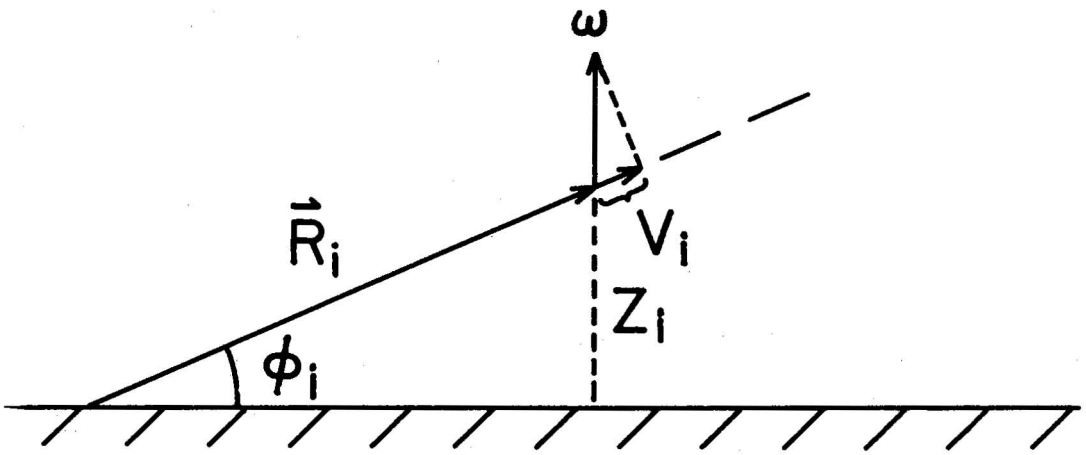

Figure 6. Simplified geometry showing relationship between the radar's elevation angle (ϕ_i), radial velocity (V_i), and the tracer vertical velocity vector (ω).

Figure 7 shows the relationship between radial velocity errors, elevation angle, and ω errors. Even a 1 m s^{-1} error in V_i can cause large problems in ω at elevation angles less than about 10°.

2.4 Solving for Air Velocity

So far, all comments have dealt with the tracer rather than air velocity. Most hydrometeors rapidly acquire the horizontal velocity of the ambient air (Wilson, 1970). The u and v components derived directly from Eq. (3) are, therefore, assumed to be indicative of the horizontal flow.

In severe thunderstorms, however, the same is not true for the vertical component since the hydrometeors' terminal velocity can be quite significant. There are two techniques to retrieve w from the basic measurements (Bohne and Srivastava, 1975). The more simple solution is to make use of the relationship

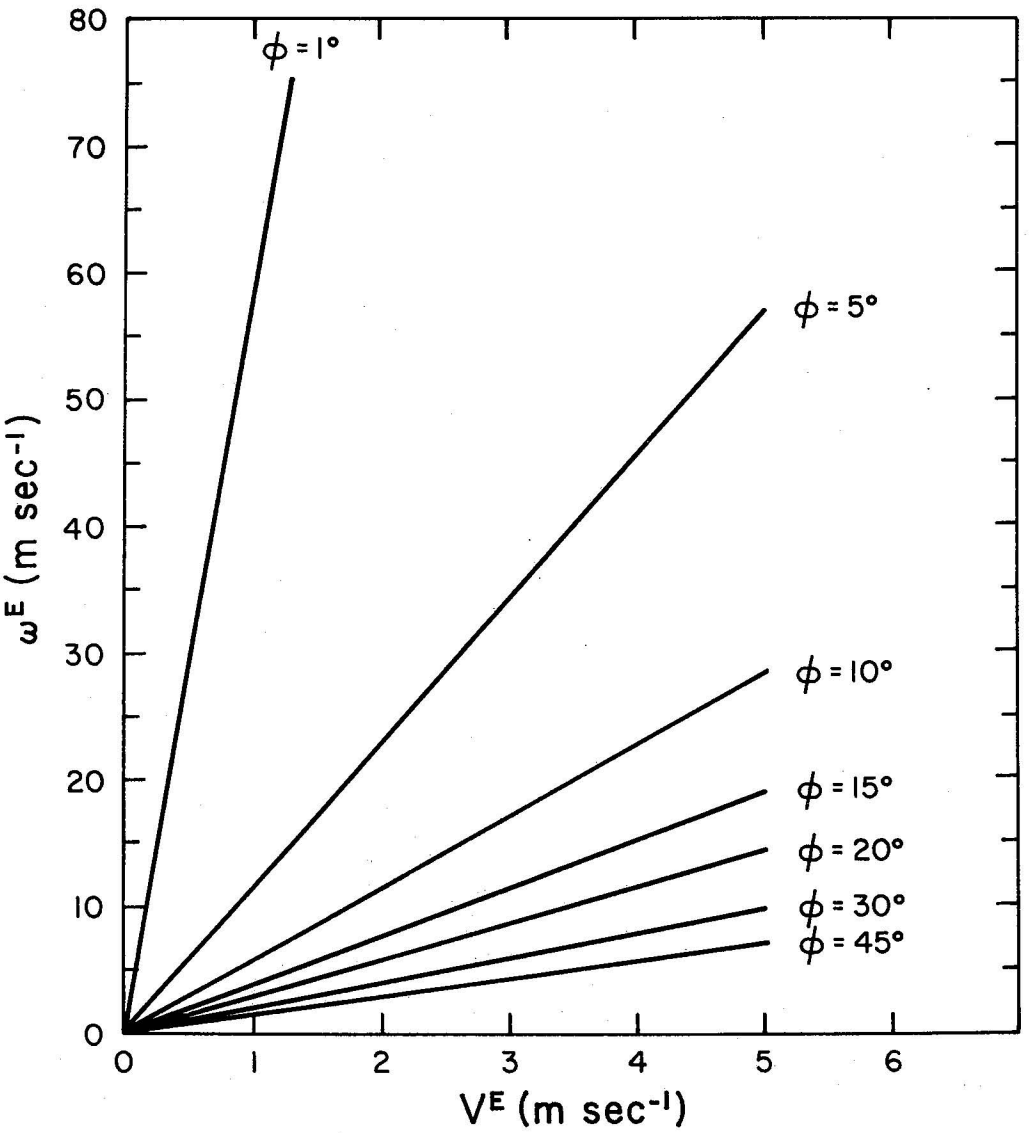

Figure 7. Relationship between radial velocity error (V^E) and tracer vertical velocity error (ω^E) as a function of elevation angle (ϕ_i).

$$w = \omega - V_T$$

where ω is measured directly and V_T can be estimated from the reflectivity field (Z_e). This has the advantage of being computationally simple and is free of numerical problems. As shown in 2.3, however, is reliable only at fairly high elevation angles. When coupled with the uncertainties in the V_T,Z_e relationship, this technique is of marginal value in severe storm research.

The second method involves integrating the simplified continuity equation

$$\frac{\partial(\rho_e w)}{\partial z} + \rho_e \, (\nabla \cdot \vec{v}) = 0$$

to yield

$$w_n = w_B \frac{\rho_B}{\rho_n} - \frac{1}{\rho_n} \int_{Z_B}^{Z_n} \rho_e \, (\nabla \cdot \vec{v}) \, dZ$$

where the subscripts refer to quantities at the integration limits (B-boundary; n-any level "n"). This equation is usually solved over small intervals in a stepwise manner using a numerical approximation for the integral term. For example, using the trapezoidal integration approximation the vertical velocity at level 2 in Fig. 8 is given by

$$w_2 = w_B \frac{\rho_B}{\rho_2} - \frac{1}{\rho_2} \frac{\Delta Z}{2} \left[\rho_B (\nabla \cdot \vec{v})_B + \rho_2 (\nabla \cdot \vec{v})_2 \right] + E_I$$

where E_I is the error term for the numerical approximation. For the moment ignoring E_I, the general expression is

$$w_n = w_B \frac{\rho_B}{\rho_n} + \sum_{i=2}^{n} \Delta w_i \frac{\rho_i}{\rho_n} \qquad (5)$$

where

$$\Delta w_i = \frac{1}{\rho_i} \frac{\Delta Z}{2} \left[\rho_{i-1} (\nabla \cdot \vec{v})_{i-1} + \rho_i (\nabla \cdot \vec{v})_i \right]$$

Note that the w_B and $\sum \Delta w_i$ terms could be combined. They are treated separately, though, because errors in these two terms come from different sources. w_B errors are due to erroneous boundary values and $\sum \Delta w_i$ errors arise from inaccuracies in the integral term at previous levels. These errors will be treated in 2.4.2 and 2.4.3.

To solve Eq. (5), it is necessary to have the u,v fields computed from Eq. (3), a boundary condition for w, numerical techniques for approximating the divergence as well as the integral term, and an expression for density with height. For the present analysis program, this latter term is obtained by a third degree polynomial approximation to the U.S. Standard atmosphere for 30°N in July (ESSA-NASA, 1966). Eq. (5) shows that errors will be introduced into w_n if the approximate density ratio is significantly in error. To test this possibility the density ratios at 150 m intervals in the updraft of a one-dimensional adiabatic model were

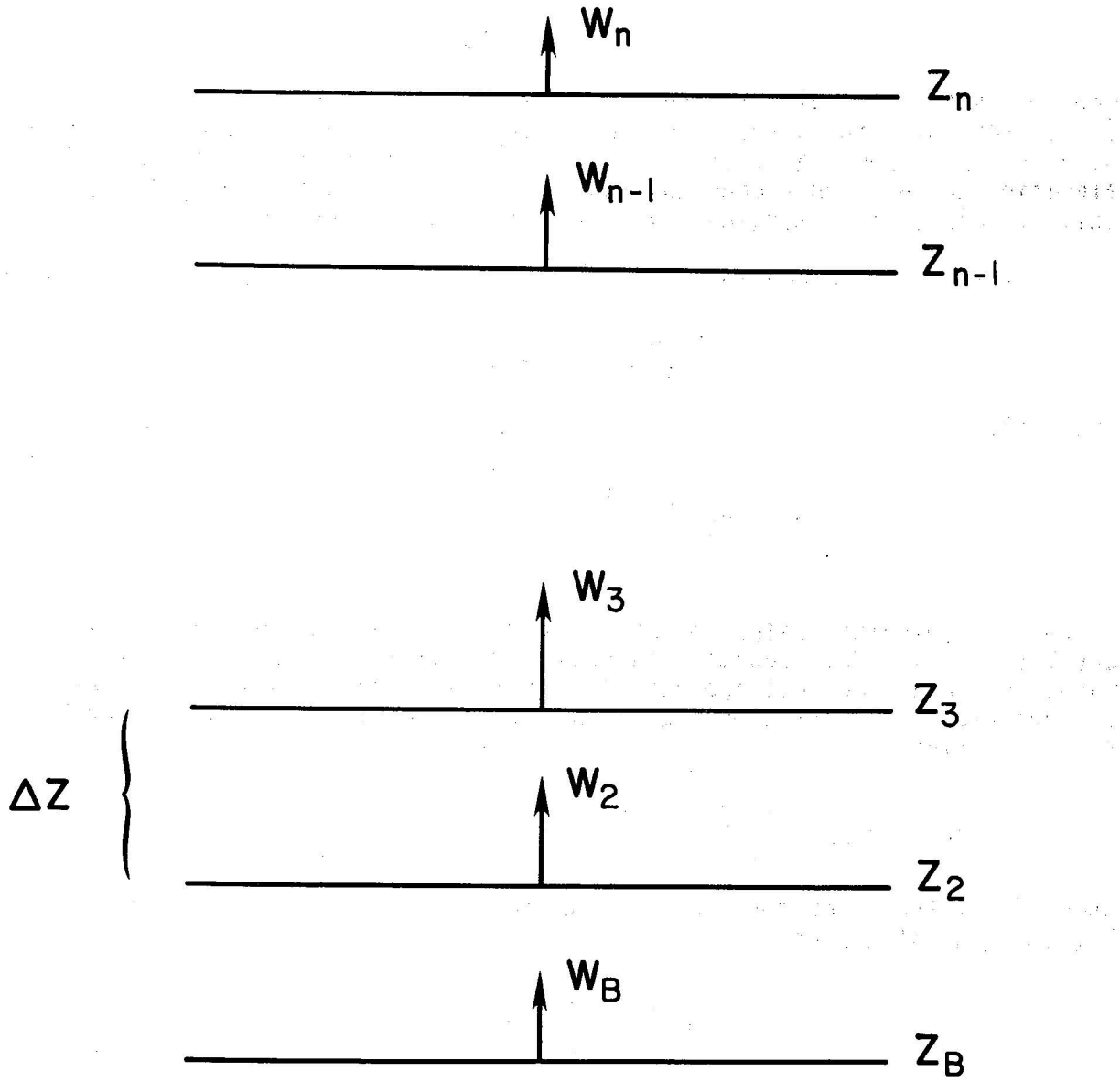

Figure 8. Diagram illustrating stepwise solution of integral form of continuity equation.

compared with the Standard Atmosphere ratios at the same levels. Eleven cases were investigated using National Severe Storm Laboratory's (NSSL) environmental soundings as model input. The density approximations were excellent with the disagreement always less than 1%.

2.4.1 Numerical Approximation Errors

Several different numerical approximations can be used for the derivative and integral terms needed to solve Eq. (5). In this study the 5-point finite difference and the trapezoidal integration approximations are utilized. Assuming a sine wave, the truncation errors (ratio of numerical to analytical first derivative) as a function of data spacing (Δx) have been calculated for 3 and 5-point finite difference approximations (Fig. 9; Haltiner, 1971). Even the 5-point estimator does not adequately reproduce waves of the order $4\Delta x$ and less. These scales should be eliminated by filtering.

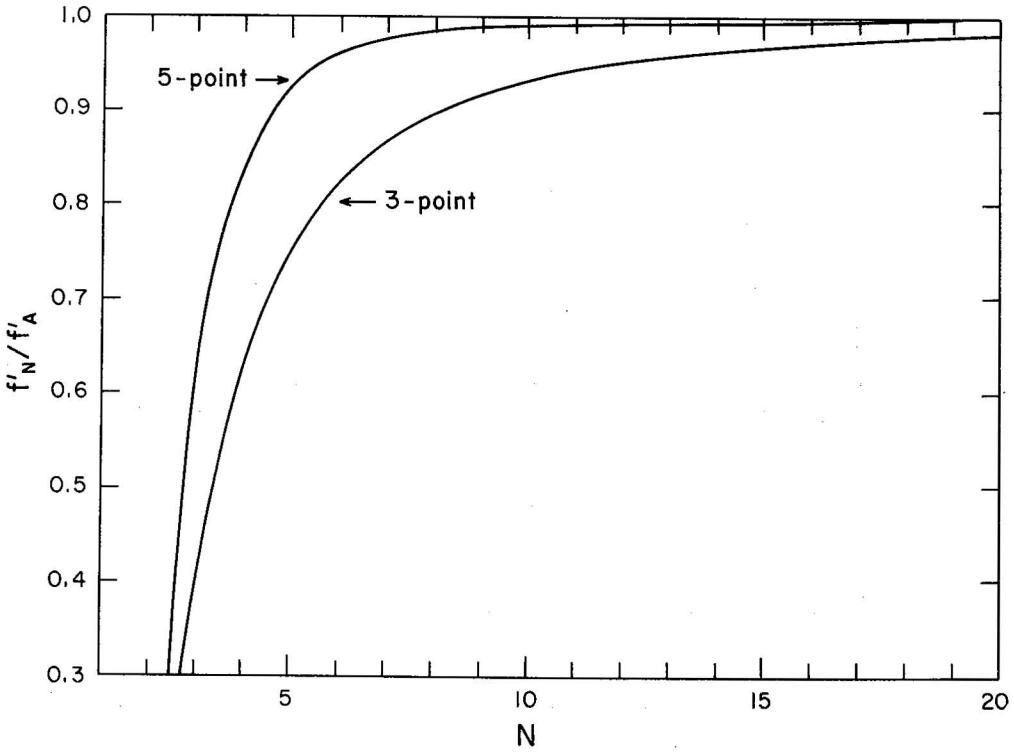

Figure 9. Three and five point finite difference operators' truncation errors (ratio of numerical to analytical derivative, f'_N/f'_A). N is the ratio of the analytical sine wave's wavelength to the data spacing (Δx).

For the trapezoidal rule, the integration error (E_I) is given by (e.g., Carnahan et al., 1969)

$$E_I = \frac{(\Delta z)^3}{12} \frac{\partial^2[\rho_\xi (\nabla\cdot\vec{v})_\xi]}{\partial z^2}$$

or

$$E_I = \frac{(\Delta z)^3}{12} \left[(\nabla\cdot\vec{v})_\xi \frac{\partial^2 \rho_\xi}{\partial z^2} + 2 \frac{\partial \rho_\xi}{\partial z} \frac{\partial (\nabla\cdot\vec{v})}{\partial z} + \rho_\xi \frac{\partial^2 (\nabla\cdot\vec{v})_\xi}{\partial z^2} \right] \quad (6)$$

where z - integration height interval (z_1 to z_2), ξ is the height at which the error maximizes and $z_1 \leq \xi \leq z_2$. In principle it is not possible to evaluate Eq. (6) since the first and second derivatives of the density and divergence with height are not known. An estimate of the magnitude of Eq. (6) can be made, however, by making assumptions about the nature of the density and divergence. For this analysis, we assume the density (kg m^{-3}) is well represented by:

$$\rho_a = a + b\,Z + c\,z^2 \quad (7)$$

and the divergence varies as a cosine wave function:

$$\nabla \cdot \vec{v} = A \cos\left(\frac{2\pi}{L} z\right) \quad (8)$$

The constants in Eq. (7) were obtained by a polynomial least squares fit to a standard atmospheric density (a = 1.1 kg m^{-3}; b = 0.9 10^{-4} kg m^{-3} m^{-1};

$c = 0.2\ 10^{-8}$ kg m^{-3} m^{-2}. Substituting Eq. (7) and (8) into Eq. (6), assuming $A \approx 10^{-2}\ s^{-1}$, $\rho = \rho_\xi \approx 1$ kg m^{-3}, $\Delta Z = 10^3$ m, $\xi \approx 10^4$ m, we obtain the vertical velocity error due to E_I at each integration step to be

$$\varepsilon^N(m\ s^{-1}) = \frac{1}{\rho_n} E_I \approx 0.4 \cdot 10^{-2} - \frac{2 \cdot 10^3}{L} + \frac{6 \cdot 10^6}{L^2} \qquad (9)$$

The first term is always small and can be neglected. Table 1 shows ε^N as a function of L due to the last two terms. As will be shown later, errors as small as 1 m s^{-1} at each integration level can sum into fairly high erroneous vertical velocities. It is, therefore, beneficial to filter scales of the order $4\Delta Z$ or less. This, of course, places a lower limit on the detail that can be resolved by the model.

Table 1. Errors in computed vertical velocity at each integration step (ε^N, m s^{-1}) due to trapezoidal rule integration error. L - wavelength of divergence term.

L (m)	ε^N (m s^{-1})
1000	8.0
2000	2.5
5000	0.6
10000	0.2

2.4.2 Boundary Condition Errors

Using Eq. (5) the vertical velocity error at the second integration level (ε_2^B) due only to the boundary condition error (ε_1^B) is

$$\varepsilon_2^B = \varepsilon_1^B \frac{\rho_1}{\rho_2}$$

and for level 3

$$\varepsilon_3^B = \varepsilon_2^B \frac{\rho_2}{\rho_3} = \varepsilon_1^B \frac{\rho_1}{\rho_3}$$

or generally

$$\varepsilon_n^B = \varepsilon_1^B \frac{\rho_1}{\rho_n} \qquad (10)$$

Figure 10 shows ρ_1/ρ_n (standard atmosphere) versus height for integration from low-to-high (dashed lines) and high-to-low altitudes (solid lines). For example, integrating from the surface upward, a 5 m s^{-1} boundary error becomes 7.9, 13.8, and 27.3 m s^{-1} at 5, 10, and 15 km. Whereas, integrating downward from 15 km the errors are 2.6, 1.4, and 0.9 m s^{-1} at 10, 5, and 0 km.

As can be seen, for like boundary inaccuracies downward integration results in smaller errors than upward integration. In fact, an interesting relationship exists between the boundary errors for the two integration directions. When integrating from the surface upward (Z_1 = 0.0 km) and the storm top downward (Z_T = "T" km), the respective boundary condition errors at each level "n" are given by Eq. (10) as

$$\varepsilon^B_{n_1} = \varepsilon^B_1 \frac{\rho_1}{\rho_n}$$

and

$$\varepsilon^B_{n_T} = \varepsilon^B_T \frac{\rho_T}{\rho_n}$$

ε^B_T and ρ_T are the boundary condition error and air density at the storm top. Equating $\varepsilon^B_{n_1}$ and $\varepsilon^B_{n_T}$ we obtain the expression

$$\varepsilon^B_T = \varepsilon^B_1 \frac{\rho_1}{\rho_T} \qquad (11)$$

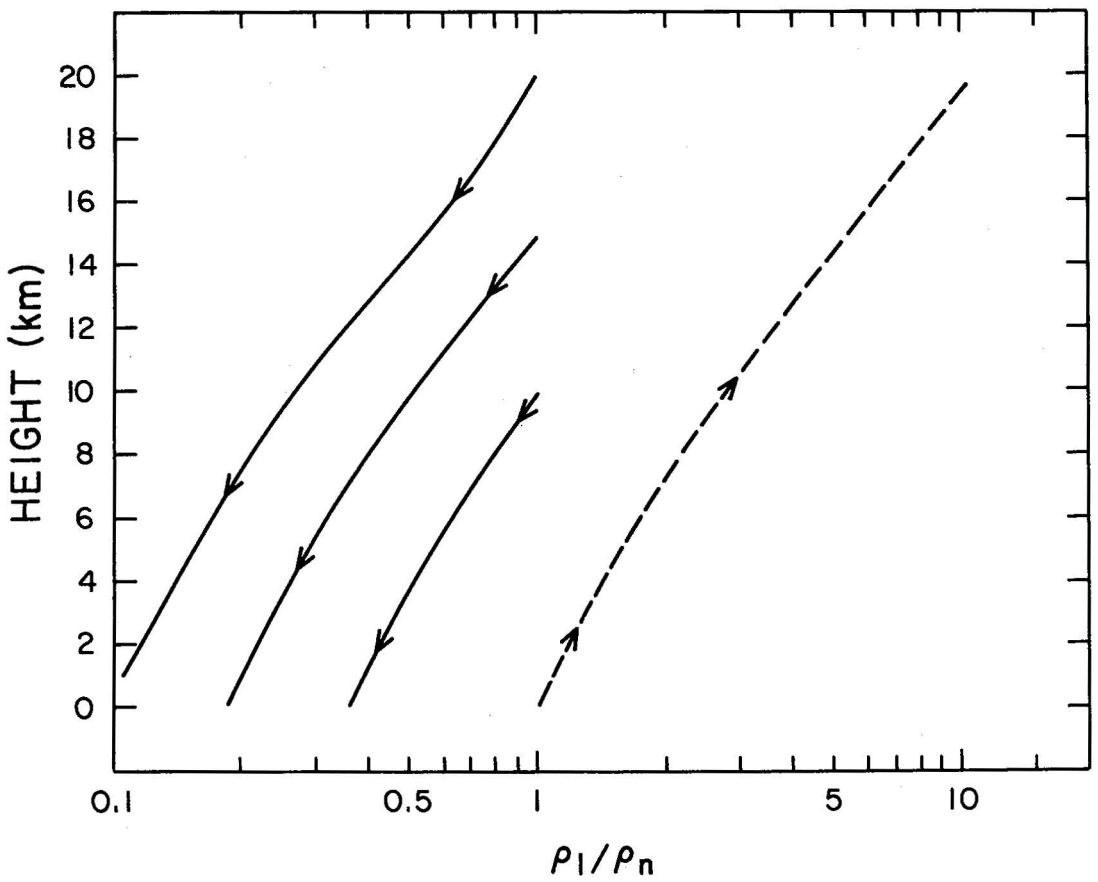

Figure 10. Ratio of standard atmosphere air density at top or bottom boundary (ρ_1) to air density at height "n" (ρ_n). Dashed line corresponds to upward integration (ρ_1 at 0 km). The three solid lines correspond to downward integration (ρ_1 = 10, 15, and 20 km).

That is, for the vertical velocity errors to be equal at each level irrespective of integration direction, the top boundary condition error must be larger than the bottom boundary condition error by a factor of ρ_1/ρ_T. The ρ_1/ρ_T ratio is the same as the dashed curve of Fig. 10. For example, beginning at 15 km and integrating downward, the top boundary condition error can be 5.4 times as large as the bottom boundary condition error and still give the same vertical velocity errors at all levels. Since the top boundary condition is usually less well known than the bottom, this relationship is an important consideration when choosing the integration direction.

2.4.3 Errors Due to Integrated Divergence

The last error source considered is that due to the second term on the right hand side of Eq. (5) (hereafter referred to as the "integral" term). These errors can come about due to incorrect density or divergence values, or to any of the previously described numerical approximation errors. The errors at each integration step are amplified or suppressed in the same way as the boundary condition errors described in 2.4.2. In a manner similar to that used in deriving Eq. (10), the total vertical velocity error at any level "n" (ε_n^I) due to the integral term is given by

$$\varepsilon_n^I = \sum_{Z_{i+1}}^{Z_n} \varepsilon^I(z) \frac{\rho_z}{\rho_n} \tag{12}$$

where Z_{i+1} is just above (or below if integrating downwards) the level at which the integration is started, $\varepsilon^I(z)$ - the vertical velocity error at each level due to the integral term of Eq. (5). Figure 11 shows $\sum \rho_z/\rho_n$ versus height (standard atmosphere). For example, assume for simplicity that $\varepsilon^I(Z)$ is 0.5 m s^{-1} at each height. The vertical velocity error will be about 20 m s^{-1} at 15 km integrating from the surface upwards. Integrating downwards from 15 km the error will be about 4 m s^{-1} at the surface. If the $\varepsilon^I(z)$ are random then ε_n^I will tend toward zero, but any bias error will produce a finite ε_n^I.

The bias error can be corrected by assuming the boundary condition error is small ($\varepsilon_n^B \approx 0$) and the error in the integral term is independent of height [$(\varepsilon^I(z) = \varepsilon^I)$]. The relationship between the computed and actual vertical velocities becomes

$$w_n^c = w_n + \varepsilon_n^I$$

substituting from Eq. (12)

$$w_n^c = W_n + \varepsilon^I \sum_{Z_{i+1}}^{Z_n} \frac{\rho_z}{\rho_n} \tag{13}$$

Assuming W_n is zero at the earth's surface or the storm top ($Z_n = Z_B$) and rearranging Eq. (13)

$$\varepsilon^I = \frac{w_B^c}{\sum_{Z_{i+1}}^{Z_B} \frac{\rho_z}{\rho_B}} \tag{14}$$

Substituting Eq. (14) into Eq. (13) and solving for W_n

$$W_n = W_n^c - \frac{W_B^c \sum_{Z_{i+1}}^{Z_n} \frac{\rho_z}{\rho_n}}{\sum_{Z_{i+1}}^{Z_B} \frac{\rho_z}{\rho_B}} \qquad (15)$$

which yields an equation to correct w at each level for bias errors in the integral term of Eq. (5). This equation is similar to the one derived by O'Brien (1970) in the x,y,p coordinate system. Note that this correction technique assumes you have two boundary conditions but it does not require data exist through the entire storm depth.

2.5 Vertical Velocity Solution Techniques

Analysis in sections 2.4.2 and 2.4.3 specified errors involved in solving Eq. (5) for vertical velocity. The relationship between computed and actual vertical velocities at any level "n" is given by

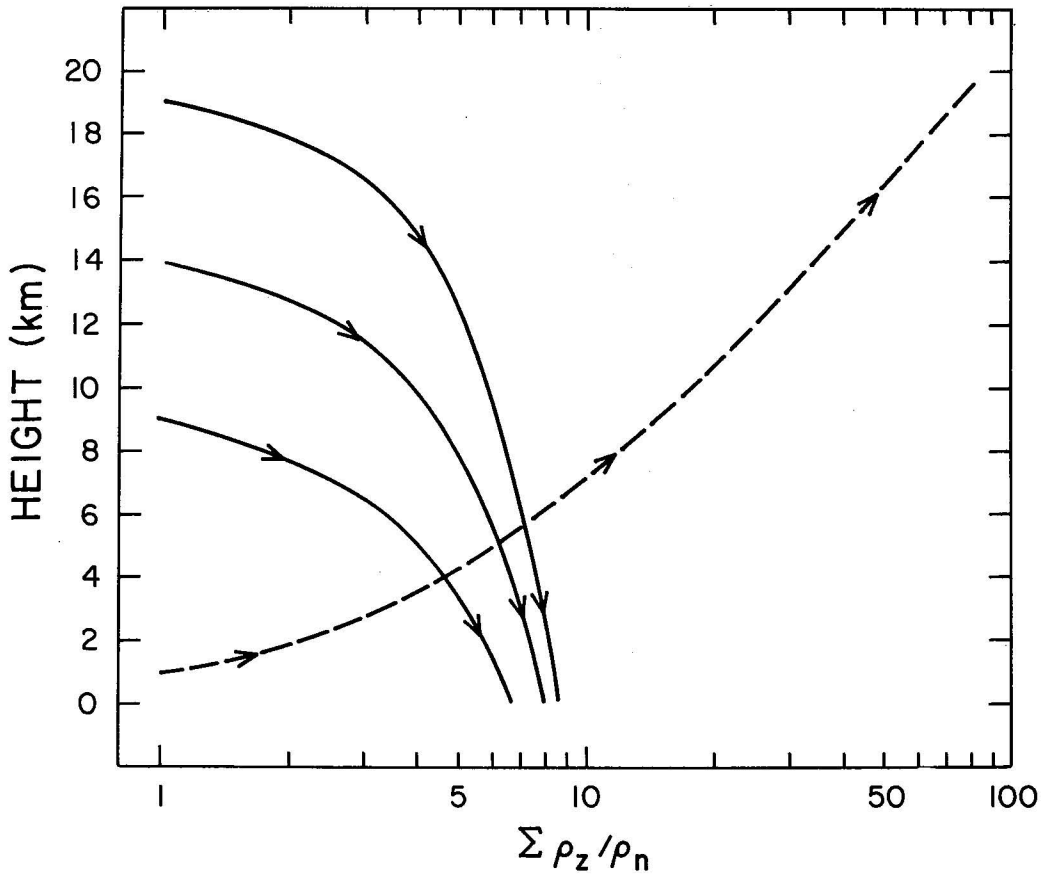

Figure 11. $\sum_{Z=Z_{i+1}}^{Z_N} \rho_Z/\rho_n$ *versus height for upwards summation* (Z_i = 0 km, *dashed line) and downwards summation* (Z_i = 10, 15, *and* 20 km, *solid lines).*

$$w_n^c = w_n + \varepsilon_n^B + \varepsilon_n^I \qquad (16)$$

The analyst's task is to retrieve w_n either by minimizing or correcting for ε_n^B and ε_n^I. Equation (5) can be solved by integrating either upward or downward. Each solution has its own unique advantages and disadvantages. There is no universally "best" method. The proper approach depends on the nature of the data and where the most accurate vertical velocities are desired.

Before proceeding further, a description should be given of the data characteristics likely to be encountered. The following comments deal specifically with updrafts, but similar arguments can be used for downdrafts. Figure 12 shows idealized structures of an intense updraft, its associated divergence field, and the environmental air density. Past work indicates updrafts are characterized by a shallow convergence area capped by strong divergence aloft (e.g., Brandes, 1977; Heymsfield, 1978; Harris et al., 1978; Wood et al., 1979). Figure 12 also graphically illustrates why errors grow when integrating Eq. (5) upward and are suppressed when integrating downward. A small false updraft induced at low levels must increase continuously with height because of the constraint of mass conservation. This erroneous updraft will not decrease because there is no compensating divergence aloft. The opposite is true if Eq. (5) is solved by integrating downward. Even a large incorrect updraft aloft will become fairly small at the lower levels. This point is demonstrated with examples in 2.6.

2.5.1 Upward Integration: Advantages and Disadvantages

Despite the amplification of ε^B and ε^I with height, solving Eq. (5) by upward integration is well suited for studying the vertical velocity in the storm's lowest levels. The main advantage is that with flat terrain the boundary condition should be fairly accurate. Figure 13 shows two possible sources of error. The analysis grid's lower boundary is positioned at some intermediate level between the highest and lowest terrain features; therefore, barriers such as small hills can cause nonzero vertical velocities at "z = 0." For the area of this study the

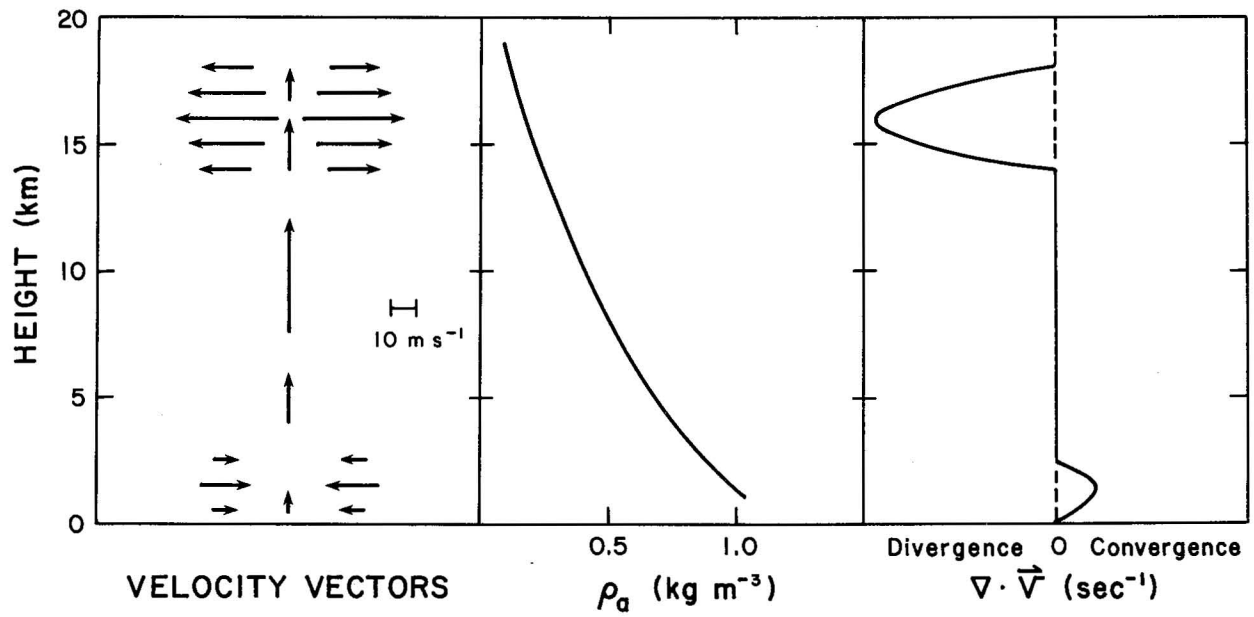

Figure 12. Idealized vertical structure of an intense updraft, its associated divergence field, and the environmental air density (ρ_a).

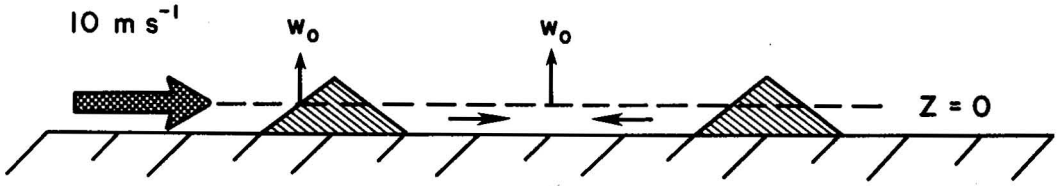

Figure 13. Diagram showing possible error sources in assuming the updraft is zero at the "earth's surface." Dashed horizontal line is "Z=0" as defined for the Doppler analysis. The cross-hatched triangles represent terrain features. The w_o's represent non-zero vertical velocities at Z=0. See text for further explanation.

largest elevation change is about 300 m in altitude over 10 km in horizontal range. Assuming a 10 m s^{-1} horizontal wind, this gives rise to a vertical velocity of less than 0.5 m s^{-1} which will not cause significant problems. Vertical velocities at z = 0 can also appear because of convergence below the analysis plane (see center of Fig. 13). Strong surface convergence can be of the order 10^{-2} s^{-1}. Assuming this operates over a 100 m depth below z = 0 yields a boundary vertical velocity of about 1 m s^{-1} which could cause moderate errors at very high levels.

ε^I presents a more serious problem for upward integration. Figure 11 illustrates the substantial growth of the errors. Integrating upward, ε^I values exceed those obtained by integrating downward above about 5 km. In fact, the actual errors may be greater than those shown since the curves in Fig. 11 assume the errors in the integral term of Eq. (5) to be the same at each level. This is probably a good approximation except for the lowest level. Unless the radar is very close to the storm, there will be no data at z = 0. This requires the analyst to estimate the divergence; hence, the largest error will probably be at this level. These errors will, of course, suffer the greatest amplification.

A final disadvantage is that it is not possible to compute vertical velocities in overhang regions which are often extensive and meteorologically important (Fig. 14). A solution can be obtained if a boundary value is specified at the bottom of the overhang, but this is dangerous since these areas often possess high vertical velocities and any errors will be amplified.

2.5.2 Downward Integration: Advantages and Disadvantages

Downward integration potentially yields its best results at mid and high levels. The main advantages are ε^B is suppressed, ε^I minimized, and solutions are possible in overhangs.

The most serious problem with downward integration lies in establishing the top boundary condition. If data exists through the storm top, assuming a zero vertical velocity is probably a good approximation. In cases where the highest data level is below the storm top, however, some other initialization method must be found. Described below are three techniques which can be used independently or collectively to obtain this boundary condition.

1. The most objective and easiest procedure is to use $w = \omega - v_T$ as described in section 2.4. This method is only valid, though, when all three radars have a high viewing angle.

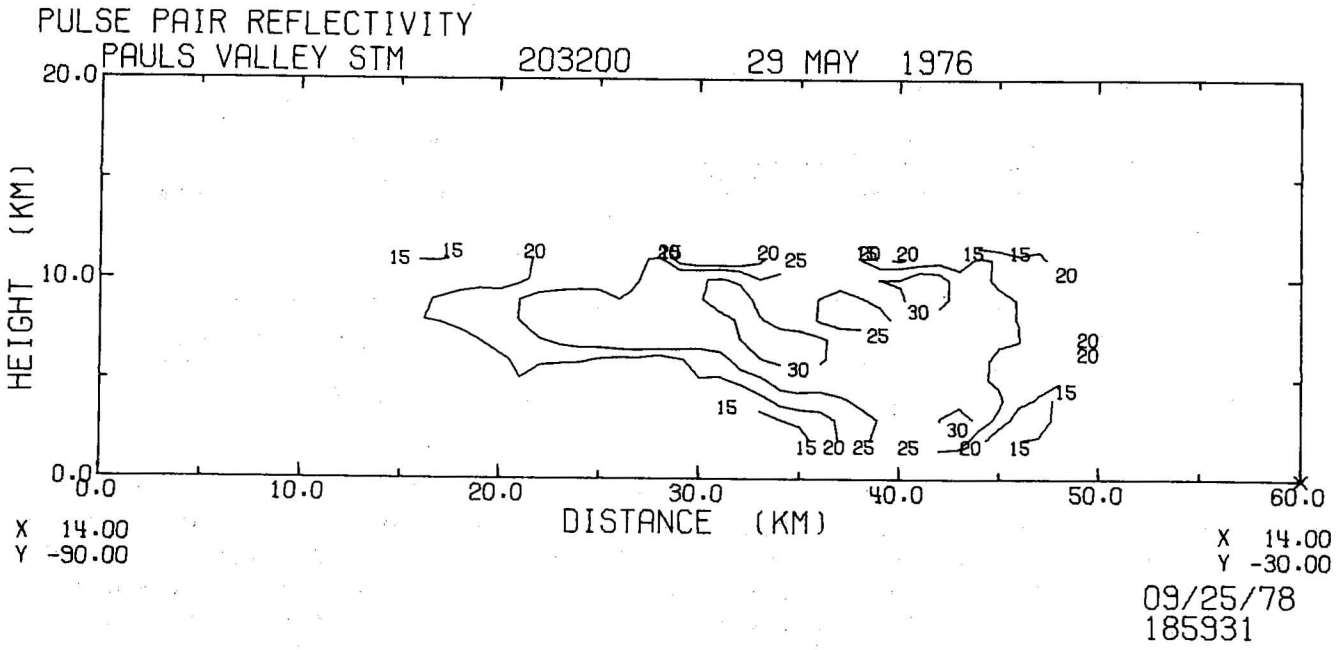

Figure 14. Vertical cross-section of storm reflectivity field contoured at 5 dBZ intervals. Note the large overhang between horizontal distances 15 and 35 km.

2. If data exists either before and/or after the time of interest, then those derived vertical velocities can be used to begin the integration. This assumes the method used to obtain the "off-time" boundary vertical velocities is superior to the one available for the data of interest.

3. The location of each strong vertical draft is established by analyzing the data using any arbitrary top boundary condition (usually 0.0 m s^{-1}). Since the effects of the arbitrary boundary values lessen with decreasing height, the analyst can obtain a good idea of the updraft's horizontal extent at the lower levels. This view of the updraft's dimensions can then be extrapolated to the top data level. An ellipse is then fitted to each strong updraft core at the top data level. The updraft is assumed to vary from a maximum in the center of each ellipse to 0.0 m s^{-1} at and beyond a distance from the cell's centers determined from the extrapolation. The maximum value in the center is determined using a numerical model in conjunction with an environmental sounding. As always, care should be taken in applying or comparing a numerical model with an actual atmospheric situation.

4. This is the same as technique (3) except that a different method is used to establish the maximum updraft value. In this case one analyzes the data using several different boundary values. The updraft profile at the top is then extrapolated back to 0.0 m s^{-1}. The chosen profile is the one that gives a 0.0 m s^{-1} updraft at the observed storm top if it is known from another source.

All of the above methods can yield boundary values that are in error by a few or even a few tens of meters per second. As shown in Fig. 10, however, the effects of any error decreases with decreasing height. The exact boundary value is especially not critical if data extend above the level of maximum divergence. For example, assume data are available only up to 17 km in Fig. 12. Since the divergence values are so strong at and below this level the integral term in Eq. (5) will dominate over the boundary value. After a few integration steps, the contribution to the updraft of the boundary value will be so small that even large errors will be insignificant. This will be demonstrated in the next section.

2.6 Solution Examples

The programming system that produces the triple Doppler derived wind fields is described in Appendix A. Inputs to the triple Doppler synthesis program are the edited radial velocity data from three radars. This data has already been objectively analyzed to a common cartesian grid. The output is a data tape that contains the u,v,w and ω fields on the same grid. This data can be displayed in any one of several ways. Reflectivity fields from one or all three of the radars can also be analyzed by programs in the analysis system, but outside the triple Doppler synthesis loop. The reader is referred to Appendix A for additional details on grid construction, data handling and display.

2.6.1 Simulated Data[2]

When using a complex programming system it is beneficial to perform tests using as input simulated radial velocity data computed from known analytical functions. This process is useful not only to gain confidence in the system, but also to isolate and study various error sources. A myriad of tests can be performed, but for this work we will examine only four aspects of the Doppler synthesis:

1. Test correctness of basic program.

2. Test magnitude of errors due to flat plane assumption.

3. Show effects of erroneous boundary condition.

4. Show errors in computed vertical velocity due to localized errors in the data.

The radar configuration used for the tests is shown in Fig. 15. This was chosen primarily because of its similiarity to the three Doppler network used in this study. The analysis grid is indicated in the upper left hand corner of Fig. 15. The grid contains 61 x 61 points in the horizontal and 18 grid points in the vertical. The grid spacing is 1 km in all three directions. For each radar the appropriate radial wind components have been computed directly at the grid points. This bypasses the necessity of interpolating the data; hence, any errors associated with this process are avoided. In addition, since we are interested in seeing the effects of the cumulative errors, the correction described by Eq. (15) is not employed in the solutions unless explicitly stated.

The simulated horizontal wind field is from 180° at 5 m s^{-1} at the surface (0.0 km, AGL). It is constant in the horizontal, but veers with height at the rate of 10° km^{-1} and increases in magnitude by 5 m s^{-1} km^{-1}. The vertical velocity is zero everywhere. Since there are no horizontal gradients and vertical gradients are linear, the derivative and integral numerical approximations are exact. This field is used for tests 1 through 3. For test 4, localized erroneous data is superimposed on this basic field. This modification will be discussed later.

Tests 1 and 2 are considered together. As explained in Appendix A the analysis grid is established using the actual distances along the earth's curved surface. For simplicity, we assume the earth is a flat plane which causes slightly

---

[2]Simulated data were constructed by Rodger Brown of NSSL for testing of a dual Doppler program. The author used the same test data for verification.

erroneous relationships between the data and the radars. For most distances involved in multi-Doppler analysis, these errors are small. Table 2 shows the exact and computed u, v, and w values (computed w is from upward integration). The velocity means and standard deviations are computed over each horizontal plane. The Doppler synthesis faithfully reproduces the velocities, usually within a tenth of a m s^{-1}.

The simulated data can also be used to demonstrate the effect of an incorrect boundary condition. Table 3 shows the vertical velocities computed from the simulated data using an incorrect 5 m s^{-1} boundary condition. As is expected, the error is minimized when integrating downwards.

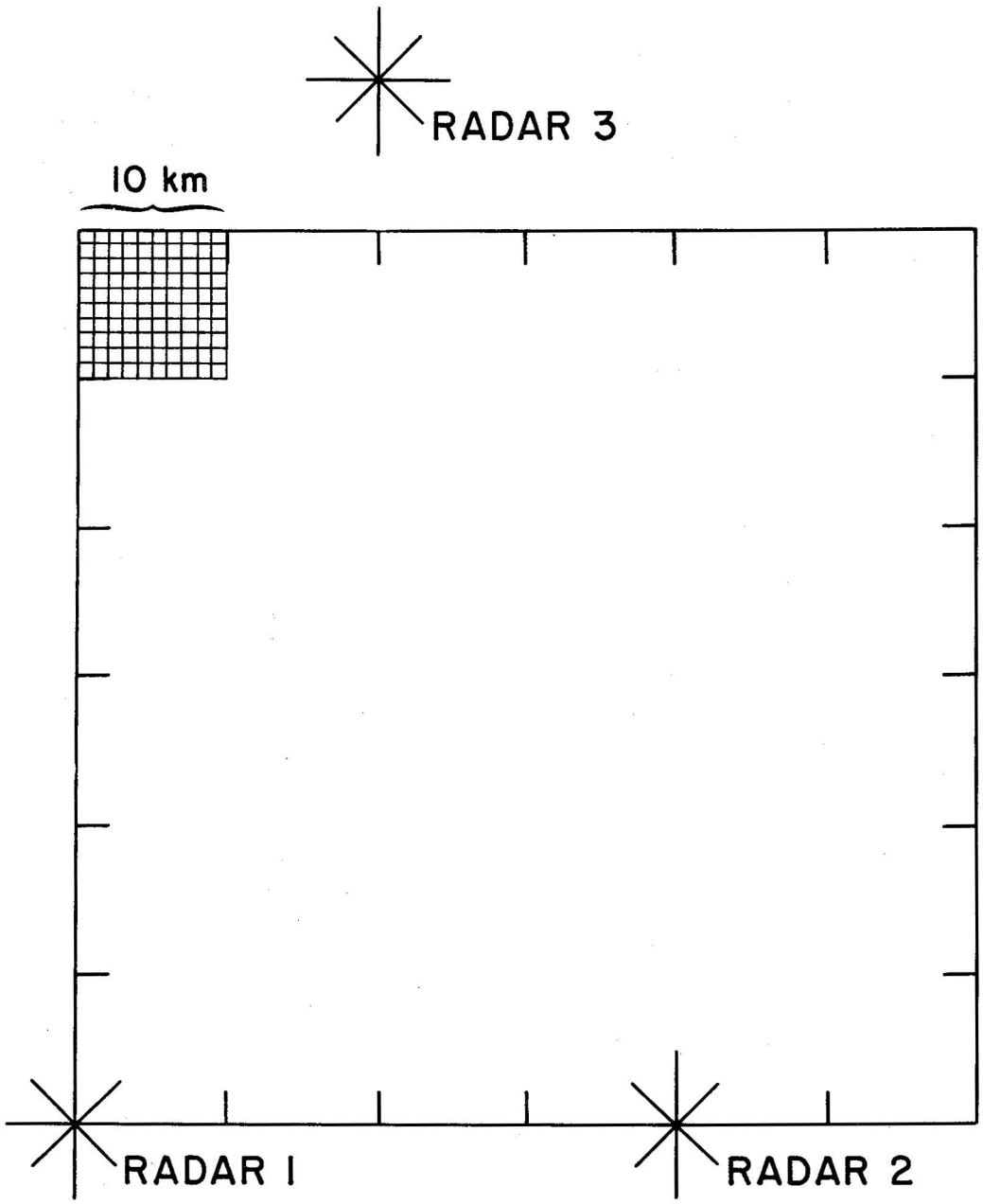

Figure 15. Radar and analysis grid configuration for simulated data tests. Analysis grid domain is bounded by heavy black lines with tick marks at 10 km intervals. Example of 1 km grid spacing is shown in the upper left hand corner.

Table 2. Comparison of exact u, v, and w wind components at grid points derived from analytical functions and Doppler synthesis values computed from radial velocities. The given Doppler values are means (standard deviations) over 60 x 60 km grid (1 km grid spacing).

Height (km,AGL)	$u(\sigma_u)$ (m s^{-1}) Exact	Computed	$v(\sigma_v)$ (m s^{-1}) Exact	Computed	$w(\sigma_w)$ (m s^{-1}) Exact	Computed
17.4	9.6	9.7(0.14)	-91.5	-91.6(0.04)	0.0	0.0(0.00)
14.4	45.3	45.2(0.13)	-62.3	-62.3(0.03)	0.0	-0.0(0.01)
10.4	55.3	55.2(0.11)	-13.8	-13.7(0.02)	0.0	-0.0(0.01)
6.4	33.3	33.1(0.08)	16.2	16.3(0.02)	0.0	-0.0(0.01)
2.4	6.9	6.9(0.05)	15.5	15.5(0.02)	0.0	-0.0(0.01)
0.4	0.5	0.5(0.03)	7.0	7.0(0.02)	0.0	0.0(0.02)

Table 3. Computed vertical velocities at different heights integrating from the bottom up ($\int\uparrow$) and from the top down ($\int\downarrow$). Input is analytical radial velocities. The correct vertical velocity is zero everywhere. Shown are triple-Doppler synthesis, means (standard deviations), using incorrect (5.0 m s^{-1}) boundary conditions. Values are averages over each horizontal level.

Height (km,AGL)	$\int\uparrow$	$\int\downarrow$
17.4	38.0(0.13)	5.0(0.00)
14.4	25.1(0.08)	3.0(0.01)
10.4	14.6(0.05)	1.6(0.01)
6.4	9.1(0.03)	1.0(0.01)
2.4	6.1(0.01)	0.6(0.01)
0.4	5.2(0.01)	0.5(0.02)

Test 4 is used to show the effect of a localized error. In this particular case we simulate the consequence of a bad point in the radial velocity of radar 3. The velocity is assumed to be in error by +5 m s^{-1} at the center grid point of the first integration level. To simulate the effect of the objective analysis, the error varies linearly from 5 m s^{-1} to 0.0 m s^{-1} at a distance 2 km from the center point. The same holds true for the second integration level except the peak error magnitude is +3 m s^{-1}. No radial velocity error is present beyond the second integration level. Figure 16 shows the peak updraft magnitude at each level integrating upward (errors in bottom two levels) and downward (errors in top two levels). Note that a substantial but false updraft can be produced when integrating upward.

Even though we are simulating a bad radial velocity point, this type of error can arise in other ways. For example, local small scale turbulence can cause the numerical derivative and/or integral approximations to be in error causing errors that amplify. Filtering can help alleviate this problem. The interpolation technique filters the data somewhat. Since, however, the relationship

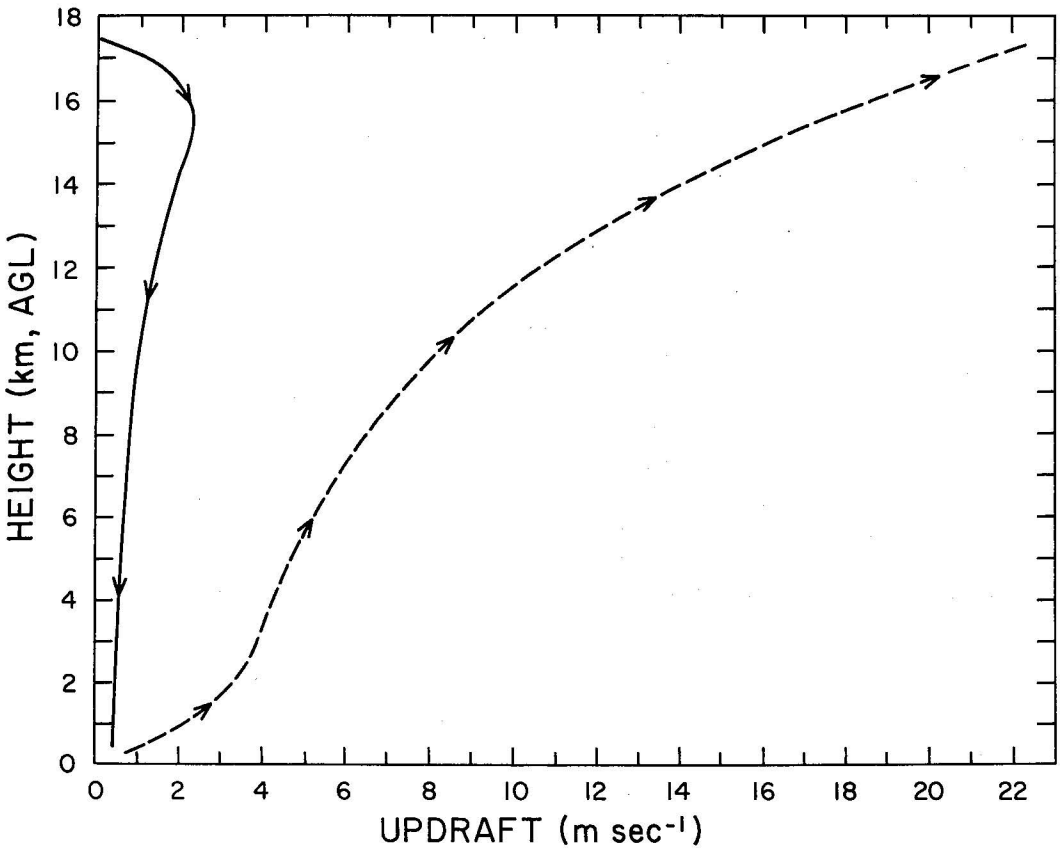

Figure 16. False updrafts caused by localized errors in radial velocity field. The arrowheads indicate the direction of integration.

between the data and the grid varies, the exact nature of the filtering is difficult to predict. It was found to be convenient to apply a separate three dimensional Shuman filter (see Appendix B).

2.6.2 Actual Data

The data chosen is from a supercell type storm (Marwitz, 1972; Browning, 1977) that occurred on 29 May 1976 in central Oklahoma. It produced a funnel cloud and 4-5 cm hail. The NSSL Norman and Cimarron Doppler radars along with the CHILL radar were used as data sources. A description of the particulars of the storm day and the characteristics of the NSSL Dopplers can be found in Alberty et al. (1979). Due to the vagaries of data collection, the lowest data level is at 1.0 km and highest at 11 km even though the storm extended to about 14-15 km as revealed by NSSL's WSR-57 radar. It is instructive to use a case with some missing data since, while this is not the norm, it is not an uncommon occurrence. Such a data set points out the strengths and weaknesses of the different analysis techniques. For illustrative purposes, we will consider the vertical profile of one updraft core. At the analysis time (2032 CST) this core is associated with a cell that possesses a hook echo and is producing large hail.

The results of the calculations are shown in Fig. 17 for integrating upward (A) and downward (B). In both cases, the data are unfiltered, uncorrected by Eq. (15), and the boundary conditions are 0.0 m s^{-1} at 0 and 11 km, respectively. Note that even though curve B's magnitude is probably not correct due to the arbitrary boundary condition, its shape is more realistic than curve A's which appears to be increasing without bound. One pass with the three dimensional

filter decreases the magnitude of both curves, but does not change their shape (A',B').

Undoubtedly, some of the error mechanisms described in the previous sections are active in these data. The downward integration (curve B) provides a better first guess to use for correction to a final form. The adjustment described by Eq. (15) can be applied easily. The computed vertical velocity at 0.0 km [W_B^C in Eq. (15)] is derived using the same divergence at the surface as that of the last data level (1.0 km in this case). Even if this value is significantly in error, it will cause only a small error in the absolute value of W_B^C.

The main obstacle to obtaining a final corrected updraft profile is establishing the upper boundary condition. Fortunately, the data extend above the level of maximum divergence. The choice of upper boundary condition is, therefore, not as critical as it otherwise would be. Figure 18 shows the same updraft as curve B of Fig. 17 with various boundary conditions and incorporating Eq. (15). It is gratifying to see that even substantial differences in the boundary values result in only small updraft differences at and below 7 km. This is especially fortunate for this study since most hail growth occurs near this level.

The actual data used here particularly demonstrate the advantages of downward integration. Data is missing in both the lowest and highest levels. Using downward integration the only effect of the missing low level divergence is to cause a slight error in the computed vertical velocity at the surface. This small error will then be spread throughout the vertical depth via the density weighting described in Eq. (15). For upward integration, however, any large error in the low level divergence is amplified substantially.

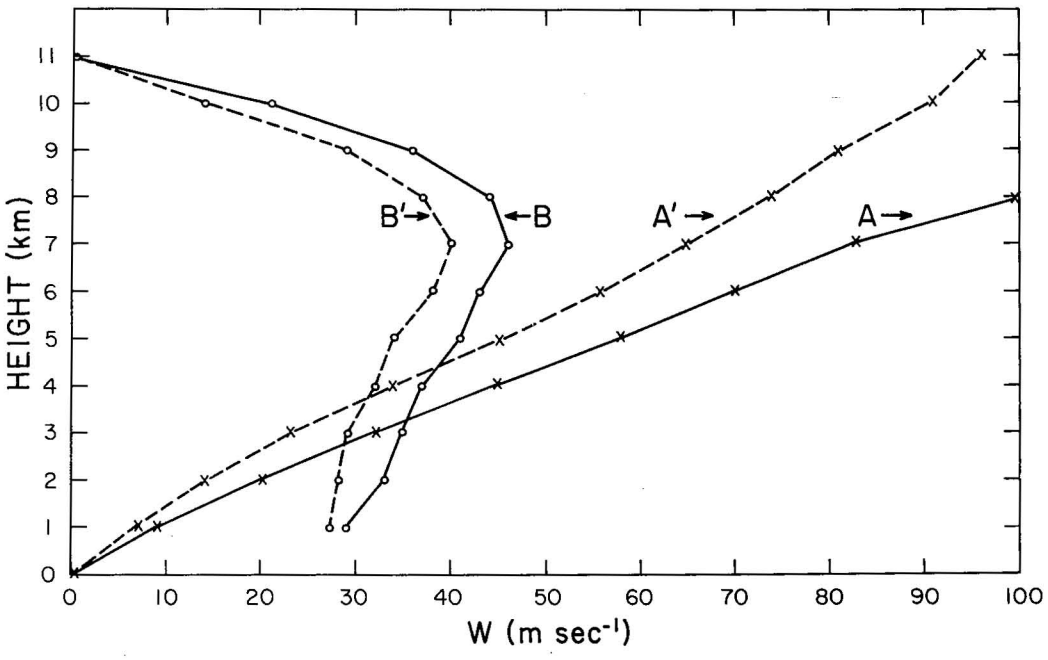

Figure 17. Vertical profiles of an updraft core synthesized from triple-Doppler data. Line A shows results from integrating upward and line B for downward integration. The primed curves are the same as the unprimed except the horizontal velocities were filtered before solving for w.

Missing data at the highest levels present a boundary condition problem for downward integration. Fortunately, however, even large errors become small with decreasing altitude. Using upward integration the data can be corrected by Eq. (15) only if boundary values are assigned at the top. In this eventuality, it would be better to use these values to initialize the downward integration.

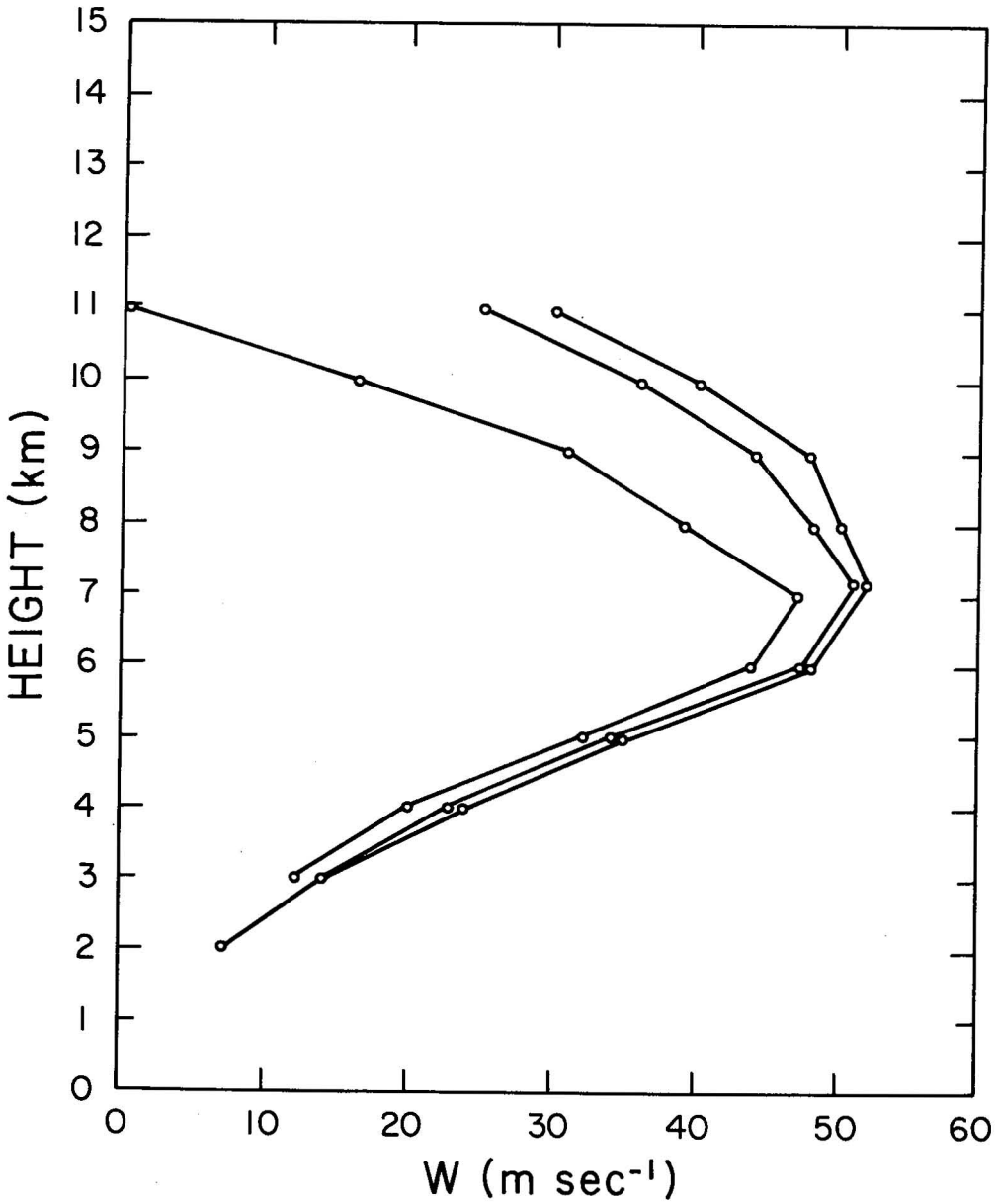

Figure 18. Updraft core of Fig. 17 (curve B) with three different top boundary conditions. The profiles have also been adjusted using the constraint w=0 at Z=0.

3. HAIL GROWTH MODEL: GENERAL DESCRIPTION

3.1 Introduction

The two steps in the numerical model are

1. Hailstone advection
2. Growth based on the microphysical model

To calculate the growth, there are two modelling techniques which can be employed--continuous (Fletcher, 1966) and stochastic (Danielson et al., 1972). The continuous model assumes all "collectible" water and ice are distributed evenly throughout a given volume. The more complex stochastic model progresses a step further in realism in that it takes into account the entire hydrometeor spectrum and its evolution, allowing for those chance collisions between like-sized particles that can accelerate precipitation growth. The simpler and more computer efficient continuous collection process is chosen since the stochastic model-predicted hailstone spectrum evolution are beyond the scope of this work. Also, the chance collisions of similarly sized particles is practically non-existent in the process of hailstones (past the embryo stage) collecting smaller cloud hydrometeors.

The next two sections describe the assumptions pertaining to storm and microphysical parameters. Following this, advection and growth processes are described in more detail.

3.2 Storm Parameters

The model requires three storm parameters be specified in three-dimensional space. These are the wind, thermal, and moisture fields. The wind field is obtained from triple Doppler data using analysis techniques described in Chapter 2. The wind vectors and, hence, all trajectories are calculated relative to storm motion (275°/15.7 m s^{-1}). The wind field is assumed to be steady throughout the hail growth periods. For most growth times (10-20 min) this is probably a good assumption. Details of the storm wind field are given in Chapter 4.

Observational evidence of thermal and moisture structure inside deep convection is limited. Using radiosonde data from Oklahoma storms, Davies-Jones (1974) showed the thermal structures of strong updraft cores are adiabatic in nature. Sailplane data in Colorado indicate vigorous updrafts contain adiabatic cores (both thermal and water) that become mixed with environmental air near the updraft's periphery (Heymsfield et al., 1978). In addition, T-28 penetrations of Colorado hailstorms during the National Hail Research Experiment showed a moderate correlation (correlation coefficient of 0.67) between updraft velocity and cloud water content (Musil et al., 1977). The basic question is whether the cloud water is significantly depleted before it reaches the prime hail growth areas. We consider three ways for this to occur--mixing, conversion to millimeter sized precipitation (hence sedimentation), and depletion by hailstone and/or graupel particles. Since the thermal structure is adiabatic, mixing is probably not significant in the updraft's core, nor is sedimentation likely to be a factor. Cloud base is approximately 2 km and the prime growth region is below 8 km. Cloud water that begins at cloud base will have only 5 min to grow assuming a 20 m s^{-1} updraft. It is unlikely that large precipitation particles could form in such a short time (Twomey, 1966; Ryan, 1974). In fact, the weak echo region itself is evidence of a slow conversion

process from cloud to precipitation particles. It will be assumed, therefore, that no depletion due to production of large liquid precipitation particles occurs in the strong updraft cores.

Information on graupel and hail spectra aloft is sparse. This makes it difficult to estimate possible cloud liquid water depletion through collection by ice particles. List et al. (1968) used a one-dimensional model to show depletion could be significant 3 km above the freezing level if the number of 0.5 cm hailstones is greater than 10 m^{-3} and the updraft is less than 25 m s^{-1}. As noted by Browning (1977), since the rate of depletion at a given level is inversely proportional to the updraft speed, depletion in storms with strong updrafts may not be significant. He further supports this point by noting the low precipitation efficiencies reported for supercell type storms. For this model, we assume depletion is not significant in the updraft core.

The adiabatic updraft cores are defined as areas interior to ellipses fitted to the +20 m s^{-1} contours of the major updrafts. Adiabatic values are determined from a simple one-dimensional model coupled with an environmental sounding. Secondary ellipses are also fitted to the +10 m s^{-1} updraft contours. The temperature excess and water content are assumed to decrease linearily from adiabatic to 0.2 of adiabatic at and exterior to the secondary ellipses. Figure 19 shows horizontal sections of the cloud water and temperature in relation to the major updrafts at 4, 6, and 8 km. The adiabatic values are given in the upper right hand corners of each section. The reader may wish to compare the figures to the overall storm structure described in Chapter 4.

3.3 Microphysical Parameters

Both initial embryos and hailstones are assumed to grow with densities of 0.9 g cm^{-3}. For hailstones as a whole, this is in agreement with most measurements (Macklin, 1977). Graupel can grow at densities somewhat less than 0.9 g cm^{-3} (Braham, 1963; Pflaum, 1978) and hence, have lower terminal velocities. While accounting for this lower density is important for the study of graupel, it is likely much less important for growth of the hailstone itself.

Along these same lines is the question of "spongy growth." Some researchers have proposed that accreted, but unfrozen water may be incorporated in the hailstone in various cavities. The liquid water can then either be frozen at a later time or remain liquid (Orville, 1977). Hailstones with high liquid water contents are not supported by observations in Oklahoma (Browning et al., 1968). It is, therefore, assumed accreted but unfrozen water is shed immediately.

For this model all hailstones are assumed to be spherical. English (1973) showed that allowing for hailstone oblateness usually results in enhanced growth; therefore, in this respect the sizes may be underestimated. To simulate the freezing process, the water mass is converted linearly from all water at -10°C to all ice at -25°C. Again, direct evidence of this water/ice question is somewhat scarce. Studies have shown that much liquid water still exists at -10 to -15°C in deep convective systems (Sand, 1976; Sarter and Cannon, 1977).

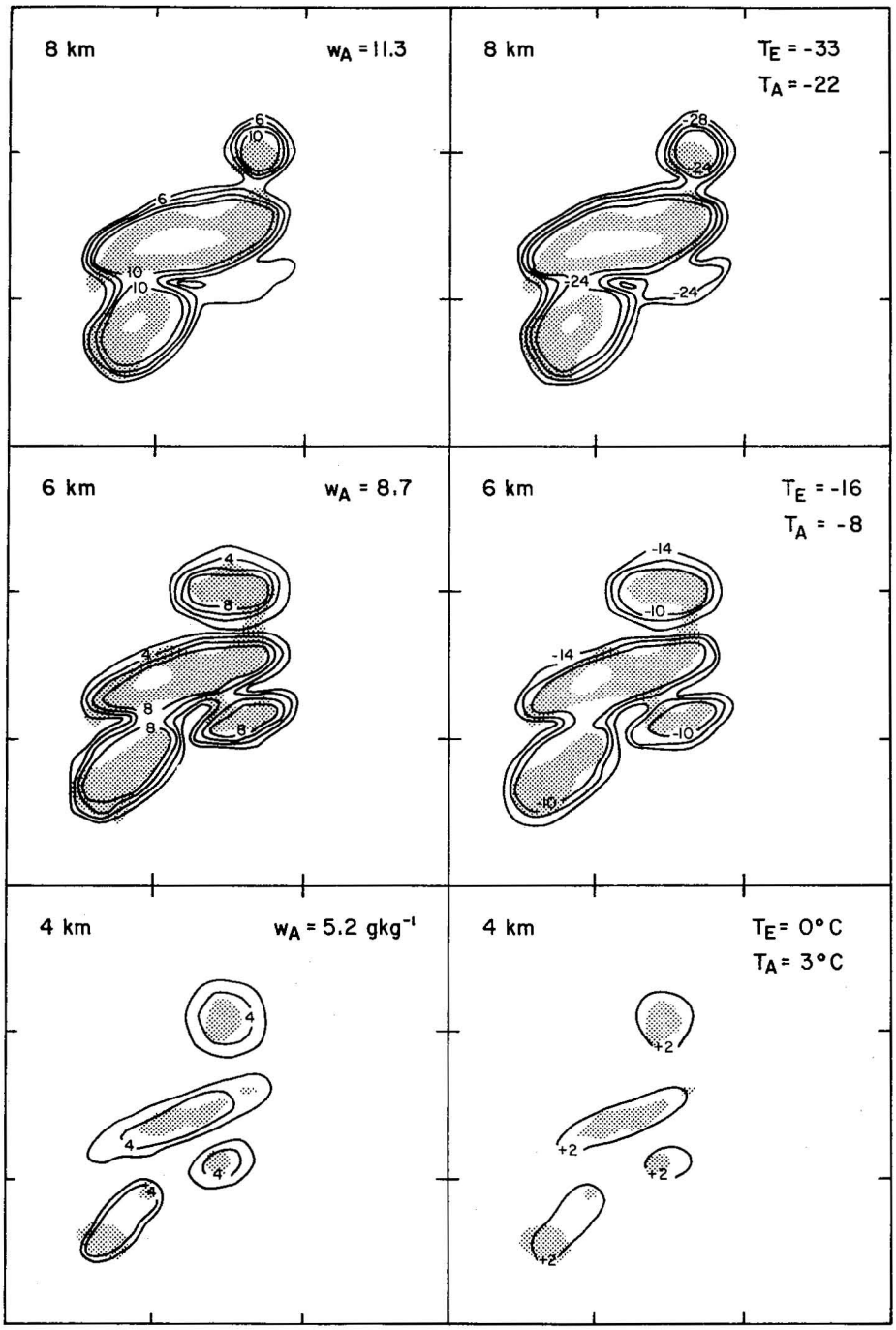

Figure 19. Horizontal sections (4, 6, and 8 km) showing relationship between computed storm updrafts, cloud water mixing ratio (left, g kg^{-1}) and temperatures (right, °C). Shaded areas indicate updrafts greater than 20 m s^{-1}. Interior light areas are updrafts greater than 40 m s^{-1}. Mixing ratios and temperatures are contoured in steps of 2 g kg^{-1} and 4°C, respectively. W_A - adiabatic water mixing ratio; T_E - environmental temperature; T_A - adiabatic core temperature. (The reader may wish to compare this figure to the storm reflectivity and velocity structure shown in Fig. 26).

3.4 Hailstone Advection

Hailstone displacements are found using the Doppler derived wind field and:

$$\frac{dx}{dt} = u \tag{17}$$

$$\frac{dy}{dt} = v \tag{18}$$

$$\frac{dz}{dt} = w - V_T \tag{19}$$

V_T is calculated by equating the gravitational and drag forces exerted on a bluff body in an air stream (Batchelor, 1967):

$$M_H\, g = \frac{1}{2}\, \rho_e\, A_c C_D V_T^2$$

or assuming a spherical particle

$$V_T = \left(\frac{4}{3}\frac{\rho_H\, g}{C_D}\frac{D}{\rho_e}\right)^{1/2} \tag{20}$$

All terms on the right hand side of Eq. (20) are known quantities.

Figure 20 (after Matson and Huggins, 1979) shows measured drag coefficients for actual hailstones and smooth spheres as a function of Reynolds number (Re). Over the range of Re for most naturally occurring hailstones (10^3 to 10^5), C_D for smooth spheres (solid line in Fig. 20) remains at a fairly constant value of about 0.45. This is somewhat lower than that measured from actual hailstones with deviations being most significant at lower values of Re. Almost all ice particles in this model have Reynolds numbers greater than 10^4 (about 5 mm in diameter and above 6 km in height). A constant value of 0.55 for C_D was, therefore, chosen for all hailstones. This is in the range of values for spherical hail found by Macklin and Ludlam, 1961 (Fig. 20).

At higher values of Re ($>10^5$) smooth spheres experience a sharp drop in C_D. This occurs in the transition between a laminar and turbulent boundary layer at the hailstone's surface. There is some evidence that hailstones with 4 to 6 cm diameters may enter this critical flow regime depending on their surface roughness (Young and Browning, 1967; Bailey and Macklin, 1967). No allowance is made for this sharp drop in C_D since few hailstones reach Reynolds numbers near this critical value and required information on surface roughness is not available.

3.5 Hailstone Growth

The mass budget of a hailstone is given by

$$\frac{dM}{dt} = \frac{dM_i}{dt} + \frac{dM_w}{dt}$$

where

$$\frac{dM_w}{dt} = \frac{\pi D^2}{4} r_w E_w V_T \qquad (21)$$

$$\frac{dM_i}{dt} = \frac{\pi D^2}{4} r_i E_i(T_s) V_T \qquad (22)$$

It is assumed that all the collected water and ice mass are composed of small hydrometeors that have negligible terminal velocities with respect to the hailstones. The cloud and ice water contents are determined from the cloud and ice water mixing ratios (see 3.2 and 3.3).

The collection efficiency is the product of the probability of a collision (collision efficiency) and the probability of the collected hydrometeor remaining with the collector (coalescence efficiency). For hailstone-supercooled water interactions, the latter term is generally assumed to be 1.0 (e.g., English, 1973). Laboratory experiments have shown that the collision efficiency decreases with increasing collector size and decreasing collected droplet size (Macklin and Bailey, 1966; Fig. 21). In order to evaluate the hailstone-supercooled water collection efficiency, some knowledge of the water droplet spectra is necessary. To date, little in situ information is available. Measurements from Colorado storms indicate a substantial amount of liquid water exists in droplets <30μ in diameter (Heymsfield et al., 1978a; Heymsfield et al., 1979; Heymsfield, 1979). Similar results from Oklahoma storms are not available. The actual droplet spectrum depends on several factors (e.g., cloud condensation nuclei, growth time)

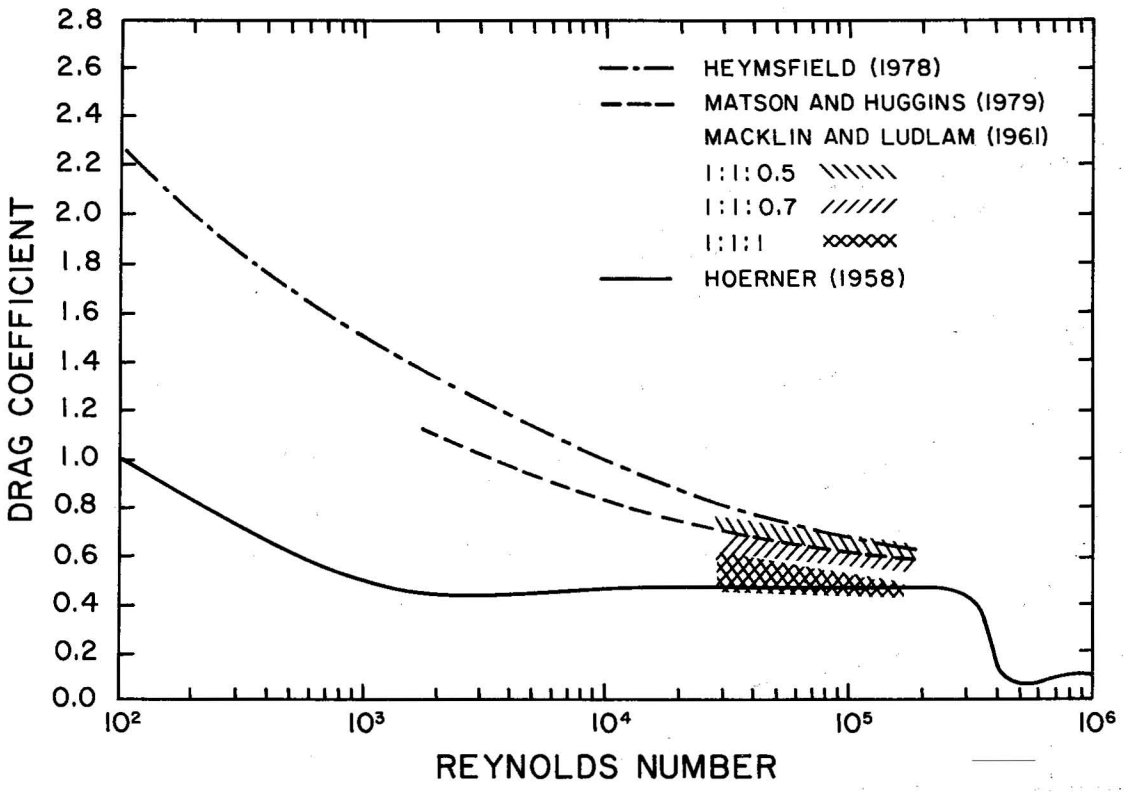

Figure 20. Drag coefficients for hailstones and smooth spheres (after Matson and Huggins, 1979). The numbers below Macklin and Ludlum show the axial ratios of the particles used in their work.

that are generally unknown. Due to the uncertain knowledge of the collected droplet sizes, a unity collision efficiency is assumed for simplicity. This is somewhat justified since few model hailstones exceed 3 cm in diameter and the collision efficiencies at and below this diameter are fairly high for most droplets.

For hailstone-ice hydrometeor collection efficiency, the same collision efficiency (1.0) is used as for water droplets. The "sticking" or coalescence efficiency, however, is dependent on the temperature of the collector (Latham and Saunders, 1970; Rogers, 1974; Passarelli, 1978). This is because an ice particle is likely to bond to another ice particle only if there is a thin layer of water between them. Almost all ice has a thin layer of water on its surface. The warmer the surface temperature, the thicker this layer, and the more likely it is that another ice particle will adhere to it. In general, these and other researchers have found the coalescence efficiency varies from 1.0 at 0°C to 0.0 somewhere between -15 to -30°C. For this study, the overall collection efficiency varies linearly from 1.0 at 0°C to 0.0 at -25°C.

A hailstone's growth characteristics are critically dependent upon its heat budget. This is given by (Macklin, 1963; List, 1963; English, 1973).

$$\frac{dQ_c}{dt} + \frac{dQ_{e,s}}{dt} + \frac{dQ_i}{dt} + \frac{dQ_w}{dt} = 0 \qquad (23)$$

where

$$\frac{dQ_c}{dt} = -\pi Da\ K(T_a - T_s) \qquad (24)$$

$$\frac{dQ_{e,s}}{dt} = \pi D\ a\ L\ d_i(\rho_s - \rho_a) \qquad (25)$$

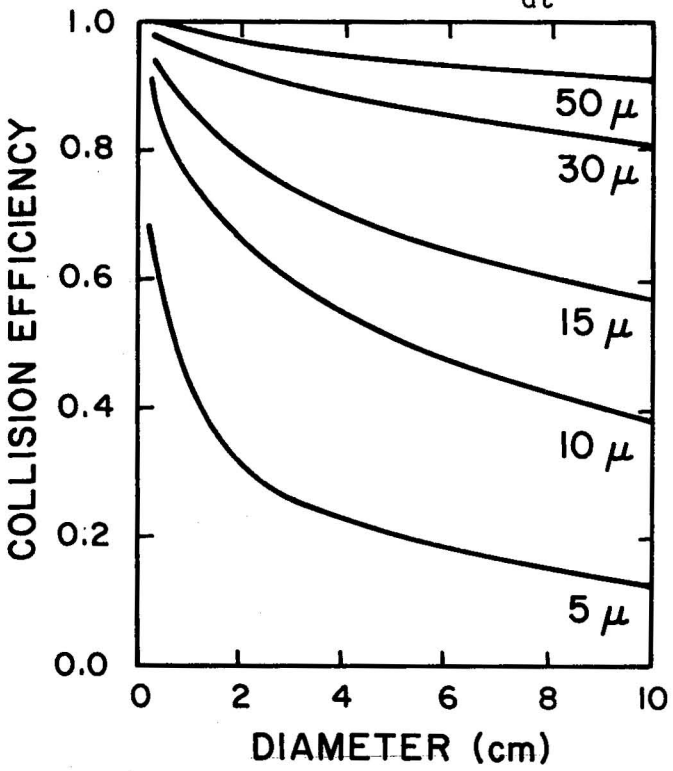

Figure 21. Collision efficiencies of hailstones and cloud droplets as a function of their diameters (after Macklin and Bailey, 1966).

L is either the latent heat of vaporization or sublimation;

$$\frac{dQ_i}{dt} = \frac{dM_i}{dt} C_{pi} (T_a - T_s) \tag{26}$$

$$\frac{dQ_w}{dt} = \frac{dM_w}{dt} [F_f L_f + C_{pw}(T_a - T_s)] \tag{27}$$

The accreted water and collected ice masses are assumed to be at the ambient temperature. The constants in (24-27) are allowed to vary with temperature and/or pressure as appropriate. The ventilation coefficients for conduction and evaporation/sublimation processes are the Nusselt (Nu) and Sherwood (Sh) numbers, respectively. For conditions of hailstone growth, however, it has been shown that (Mason, 1971):

$$a = Nu \approx Sh \approx 0.58 R_e^{1/2}$$

A hailstone's growth history is determined by the following steps:

1. The hailstone is advected using Eqs. 17-19.

2. Ambient thermal and moisture parameters are derived from their predetermined three dimensional structure. Pressure is obtained via the hydrostatic approximation. Appropriate constants needed to solve Eq. (23) are calculated using this information.

3. Dry growth is assumed ($F_f = 1.0$) and T_s computed from Eq. (23).

$$T_s = \frac{\pi Da[KT_a - L_s d_i(\rho_s - \rho_a)] + \frac{dM_i}{dt} C_{pi} T_a + \frac{dM_w}{dt} [L_f + C_{pw} T_a]}{2\pi DaK + \frac{dM_i}{dt} C_{pi} + \frac{dM_w}{dt} C_{pw}} \tag{28}$$

where dM_w/dt and dM_i/dt are calculated from (21,22). Note this is an iterative process since ρ_s on the right hand side of Eq. (28) is dependent on T_s. The first guess for the iteration is the old temperature. The calculations are stopped when the temperature difference between successive iterations is less than 0.05°C. If T_s is less than 0°C, then the growth calculations for that time step are terminated. The new hailstone mass is simply the old mass plus dM_w and dM_i. If T_s is greater than 0°C, proceed to Step 4.

4. Wet growth is assumed ($T_s = 0°C$) and F_f is computed from Eq. (23).

$$F_f = \frac{-\pi Da[K(T_a - T_s) - L_v d_i(\rho_s - \rho_a)] - \frac{dM_i}{dt} C_{pi}(T_a - T_s) - \frac{dM_w}{dt} C_{pw}(T_a - T_s)}{\frac{dM_w}{dt} L_f} \tag{29}$$

where, again, dM_w/dt and dM_i/dt are from (21,22). In this case the newly added mass is

$$dM_w F_f + dM_i$$

Figure 22. Example of hail growth model output. Keys to the labels used on the following page are shown below.

LABEL	*DEFINITION*
TIME	*Elapsed time (sec)*
DIAM	*Hailstone diameter (cm)*
MASS	*Total hailstone mass (g)*
LOCATION X Y Z	*Cartesian coordinates of hailstone with respect to grid (km; note Z is height above ground level)*
GROWTH MODE	*Hailstone growth mode: DRY, WET, or MLT (no growth)*
XMUW	*Running total of water mass accreted, but not frozen (g; shed water)*
F-FROZ	*Fraction of accreted water frozen in one time step*
TEMP-A	*Ambient temperature (°C)*
TEMP-S	*Hailstone surface temperature (°C)*
RW	*Cloud liquid water content (g cm^{-3})*
RI	*Cloud ice water content (g cm^{-3})*
AWM	*Cloud liquid water mass intercepted in one time step (g)*
AIM	*Cloud ice mass collected during one time step (gm)*
TAWM	*Running total of accreted water (g)*
TAIM	*Running total of collected ice (g)*

PARTICLE NUMBER 1

TIME (SEC)	DIAM (CM)	MASS (GM)	LOCATION(KM) X	Y	Z	GROWTH MODE	XMUW	F-FROZ	TEMP-A (DEG C)	TEMP-S (DEG C)	RW (GM/CM**3)	RI (GM/CM**3)	AWM (GM)	AIM (GM)	TAWM (GM)	TAIM (GM)
0	0.60	0.102	20.000	14.000	8.000		0.000	1.00	999.99	-27.00	0.9990E 02	0.9990E 02	0.0000	0.0000	0.000	0.000
10	0.60	0.102	20.018	14.123	7.864	DRY	0.000	1.00	-29.75	-29.76	0.0000E 00	0.1342E-05	0.0000	0.0000	0.000	0.000
20	0.60	0.102	20.027	14.251	7.745	DRY	0.000	1.00	-28.76	-28.76	0.0000E 00	0.1344E-05	0.0000	0.0000	0.000	0.000
30	0.60	0.102	20.028	14.384	7.631	DRY	0.000	1.00	-27.80	-27.80	0.0000E 00	0.1345E-05	0.0000	0.0000	0.000	0.000
40	0.60	0.102	20.021	14.523	7.520	DRY	0.000	1.00	-26.87	-26.87	0.0000E 00	0.1346E-05	0.0000	0.0000	0.000	0.000
50	0.60	0.102	20.007	14.668	7.414	DRY	0.000	1.00	-25.97	-25.97	0.0000E 00	0.1347E-05	0.0000	0.0000	0.000	0.000
60	0.60	0.102	19.984	14.819	7.311	DRY	0.000	1.00	-25.11	-25.11	0.0000E 00	0.1347E-05	0.0000	0.0000	0.000	0.000
70	0.60	0.102	19.953	14.977	7.211	DRY	0.000	1.00	-24.28	-24.05	0.6506E-07	0.1282E-05	0.0003	0.0000	0.000	0.000
80	0.60	0.103	19.914	15.142	7.115	DRY	0.000	1.00	-23.46	-23.00	0.1381E-06	0.1206E-05	0.0006	0.0002	0.001	0.000
90	0.60	0.104	19.867	15.314	7.017	DRY	0.000	1.00	-22.64	-21.94	0.2119E-06	0.1135E-05	0.0009	0.0004	0.002	0.001
100	0.61	0.106	19.813	15.495	6.916	DRY	0.000	1.00	-21.82	-20.89	0.2837E-06	0.1056E-05	0.0012	0.0005	0.003	0.001
110	0.61	0.108	19.749	15.686	6.812	DRY	0.000	1.00	-20.98	-19.82	0.3571E-06	0.9754E-06	0.0015	0.0007	0.004	0.002
120	0.62	0.111	19.675	15.887	6.704	DRY	0.000	1.00	-20.11	-18.73	0.4322E-06	0.8925E-06	0.0018	0.0008	0.006	0.003
130	0.62	0.114	19.591	16.098	6.593	DRY	0.000	1.00	-19.21	-17.61	0.5084E-06	0.8077E-06	0.0022	0.0009	0.008	0.003
140	0.63	0.117	19.497	16.315	6.482	DRY	0.000	1.00	-18.30	-16.50	0.5836E-06	0.7235E-06	0.0026	0.0009	0.011	0.004
150	0.64	0.121	19.393	16.535	6.374	DRY	0.000	1.00	-17.43	-15.44	0.6550E-06	0.6420E-06	0.0029	0.0010	0.014	0.005
160	0.64	0.125	19.279	16.759	6.272	DRY	0.000	1.00	-16.61	-14.45	0.7211E-06	0.5676E-06	0.0033	0.0010	0.017	0.006
170	0.65	0.130	19.155	16.985	6.180	DRY	0.000	1.00	-15.86	-13.56	0.7803E-06	0.4998E-06	0.0037	0.0010	0.021	0.007
180	0.66	0.135	19.021	17.213	6.100	DRY	0.000	1.00	-15.16	-12.69	0.8564E-06	0.4493E-06	0.0041	0.0010	0.025	0.008
190	0.67	0.141	18.880	17.440	6.036	DRY	0.000	1.00	-14.65	-12.07	0.8952E-06	0.4021E-06	0.0044	0.0010	0.029	0.009
200	0.68	0.146	18.734	17.660	5.991	DRY	0.000	1.00	-14.34	-11.75	0.8988E-06	0.3655E-06	0.0046	0.0010	0.034	0.010
210	0.69	0.152	18.582	17.874	5.962	DRY	0.000	1.00	-14.15	-11.51	0.9152E-06	0.3496E-06	0.0048	0.0010	0.039	0.011
220	0.70	0.158	18.426	18.081	5.948	DRY	0.000	1.00	-13.93	-11.08	0.1004E-05	0.3569E-06	0.0055	0.0010	0.044	0.012
230	0.71	0.167	18.266	18.282	5.943	DRY	0.000	1.00	-13.46	-9.89	0.1320E-05	0.3966E-06	0.0074	0.0012	0.052	0.014
240	0.72	0.179	18.104	18.474	5.948	DRY	0.000	1.00	-12.89	-8.34	0.1778E-05	0.4249E-06	0.0105	0.0015	0.062	0.015
250	0.75	0.196	17.941	18.659	5.965	DRY	0.000	1.00	-12.20	-6.34	0.2429E-05	0.4180E-06	0.0152	0.0017	0.077	0.017
260	0.78	0.220	17.776	18.837	5.996	DRY	0.000	1.00	-11.34	-3.75	0.3372E-05	0.3306E-06	0.0227	0.0017	0.100	0.018
270	0.82	0.255	17.608	19.009	6.042	DRY	0.000	1.00	-10.38	-0.75	0.4595E-05	0.1203E-06	0.0343	0.0008	0.134	0.019
280	0.85	0.294	17.437	19.178	6.099	WET	0.007	0.84	-9.99	0.00	0.5345E-05	0.0000E 00	0.0454	0.0000	0.173	0.019
290	0.89	0.336	17.262	19.346	6.171	WET	0.021	0.75	-9.86	0.00	0.5836E-05	0.0000E 00	0.0560	0.0000	0.215	0.019
300	0.93	0.383	17.083	19.516	6.257	WET	0.041	0.70	-10.01	0.00	0.6190E-05	0.2417E-08	0.0668	0.0000	0.262	0.019
310	0.98	0.439	16.899	19.691	6.359	WET	0.061	0.73	-10.53	0.00	0.6104E-05	0.2250E-06	0.0738	0.0027	0.315	0.022
320	1.03	0.508	16.710	19.874	6.467	WET	0.079	0.78	-11.24	0.00	0.5837E-05	0.5239E-06	0.0786	0.0071	0.377	0.029
330	1.08	0.592	16.515	20.064	6.571	WET	0.094	0.83	-11.91	0.00	0.5575E-05	0.8156E-06	0.0863	0.0126	0.449	0.042
340	1.14	0.693	16.313	20.265	6.664	WET	0.106	0.87	-12.51	0.00	0.5340E-05	0.1075E-05	0.0944	0.0190	0.531	0.061
350	1.20	0.813	16.102	20.476	6.731	WET	0.117	0.89	-12.95	0.00	0.5167E-05	0.1264E-05	0.1047	0.0256	0.624	0.086
360	1.26	0.951	15.881	20.695	6.774	WET	0.126	0.92	-13.33	0.00	0.4958E-05	0.1416E-05	0.1151	0.0329	0.730	0.119
370	1.33	1.115	15.651	20.923	6.795	DRY	0.126	1.00	-13.77	-0.26	0.4622E-05	0.1554E-05	0.1226	0.0412	0.853	0.160
380	1.40	1.284	15.410	21.161	6.791	DRY	0.126	1.00	-14.59	-2.12	0.3892E-05	0.1710E-05	0.1179	0.0515	0.971	0.212
390	1.45	1.441	15.157	21.409	6.751	DRY	0.126	1.00	-15.56	-4.81	0.2994E-05	0.1766E-05	0.1018	0.0549	1.072	0.267
400	1.49	1.569	14.890	21.668	6.674	DRY	0.126	1.00	-16.47	-7.86	0.2128E-05	0.1615E-05	0.0792	0.0486	1.152	0.315
410	1.52	1.665	14.607	21.940	6.560	DRY	0.126	1.00	-16.88	-10.07	0.1535E-05	0.1299E-05	0.0609	0.0353	1.212	0.351
420	1.55	1.744	14.307	22.227	6.405	DRY	0.126	1.00	-16.37	-10.30	0.1324E-05	0.9772E-06	0.0547	0.0241	1.267	0.375
430	1.57	1.815	14.001	22.517	6.206	DRY	0.126	1.00	-15.22	-9.40	0.1267E-05	0.6764E-06	0.0539	0.0169	1.321	0.392
440	1.58	1.875	13.692	22.804	5.963	DRY	0.126	1.00	-13.80	-8.52	0.1151E-05	0.3904E-06	0.0501	0.0106	1.371	0.402
450	1.60	1.933	13.390	23.076	5.664	DRY	0.126	1.00	-12.02	-6.79	0.1183E-05	0.1846E-06	0.0522	0.0054	1.423	0.408
460	1.62	1.988	13.097	23.322	5.330	DRY	0.126	1.00	-9.98	-4.77	0.1245E-05	0.0000E 00	0.0554	0.0000	1.479	0.408
470	1.63	2.040	12.817	23.534	4.983	DRY	0.126	1.00	-7.75	-3.20	0.1151E-05	0.0000E 00	0.0516	0.0000	1.530	0.408
480	1.64	2.090	12.552	23.704	4.629	DRY	0.126	1.00	-4.79	-0.81	0.1111E-05	0.0000E 00	0.0500	0.0000	1.580	0.408
490	1.65	2.114	12.306	23.819	4.276	WET	0.148	0.52	-1.87	0.00	0.1008E-05	0.0000E 00	0.0455	0.0000	1.604	0.408
500	1.65	2.114	12.075	23.876	3.917	MLT	0.188	0.00	1.08	0.00	0.8827E-06	0.0000E 00	0.0396	0.0000	1.604	0.408
510	1.65	2.114	11.860	23.878	3.549	MLT	0.222	0.00	4.10	0.00	0.7680E-06	0.0000E 00	0.0339	0.0000	1.604	0.408
520	1.65	2.114	11.660	23.830	3.180	MLT	0.250	0.00	7.04	0.00	0.6544E-06	0.0000E 00	0.0284	0.0000	1.604	0.408
530	1.65	2.114	11.471	23.743	2.845	MLT	0.273	0.00	9.76	0.00	0.5370E-06	0.0000E 00	0.0230	0.0000	1.604	0.408
540	1.65	2.114	11.298	23.627	2.516	MLT	0.291	0.00	12.23	0.00	0.4181E-06	0.0000E 00	0.0176	0.0000	1.604	0.408
550	1.65	2.114	11.146	23.491	2.207	MLT	0.303	0.00	14.55	0.00	0.2991E-06	0.0000E 00	0.0124	0.0000	1.604	0.408
560	1.65	2.114	11.014	23.340	1.912	MLT	0.311	0.00	16.27	0.00	0.1982E-06	0.0000E 00	0.0081	0.0000	1.604	0.408
570	1.65	2.114	10.902	23.177	1.631	MLT	0.317	0.00	16.80	0.00	0.1415E-06	0.0000E 00	0.0057	0.0000	1.604	0.408
580	1.65	2.114	10.807	23.004	1.371	MLT	0.320	0.00	17.29	0.00	0.8567E-07	0.0000E 00	0.0034	0.0000	1.604	0.408
590	1.65	2.114	10.727	22.820	1.130	MLT	0.321	0.00	17.75	0.00	0.3090E-07	0.0000E 00	0.0012	0.0000	1.604	0.408

The time step used is 10 sec. Tests show that decreasing this interval does not result in significant changes in the growth process. This agrees with English (1973). These steps are repeated until the hailstone exits any of the model's boundaries. When the hailstone falls below the melting level, advection is continued, but all growth is terminated. Melting is not considered since this study is focused in the growth phase only. Melting calculations also require knowledge of the thermal structure in the downdraft, and, since this storm did not pass over any surface instruments such information is not available. Temperature retrieval methods (Hane and Scott, 1978; Gal-Chen, 1978) show promise of acquiring thermal structure from Doppler measurements, but they are still in the developmental stage and have not produced results from actual data.

An example of the model is shown in Fig. 22. The large difference in the first two hailstone temperatures is due to initial temperature assigned to the hailstone. For simplicity initial T_s for all hailstones at a given level is defined to be the average of the environmental and adiabatic core temperatures. Note that the hailstone undergoes a transition from dry to wet growth at 270 sec. This occurs because the hailstone is entering the storm's major updraft as is evidenced by the higher temperatures and liquid water.

As with all numerical models, this one is only as good as its assumptions. Weaknesses of the model include the steady state assumption, lack of knowledge of microphysical parameters and the distribution of the thermal and moisture fields. The main model strength is its three-dimensionality, including the actually measured Doppler wind field. The critical factor is the specification of parameters with sufficient accuracy so that their interactions in producing large hail may be studied. It is not believed (nor necessary) that the computed trajectories are related one-to-one to actual hailstones at the surface.

4. STORM CHARACTERISTICS

4.1 General Features and Environmental Conditions

The supercell storm that is the subject of this investigation occurred in central Oklahoma on the evening of 29 May 1976. It produced 4 to 5 cm hail and a funnel cloud. Synoptically, at the surface, a low pressure center was located in northwestern Kansas at 0600 (all times are CST) on the morning of the storm. During the next 24 hours, this low slowly deepened and settled into the Texas panhandle. By 1800 the cold front associated with the low stretched from southwest to northeast across the northwest corner of Oklahoma. A north-south dryline existed in the Texas panhandle and moved slowly eastward during the day until it reached the Texas-Oklahoma border (Weaver, 1979). Storms appeared to form on this dryline with the approach of a moderately strong short wave (500 mb height falls of 30 m over 12 hours).

The local storm environment was revealed by a sounding launched at 1730 from the NSSL Elmore City rawinsonde site located approximately 60 km due south of NSSL. Figure 23 shows the temperature and dewpoint profile with height on a Stuve diagram. The lifting condensation level (Petterssen, 1956) is at 830 mb or about 1.5 km. The instability was high with a lifted index of -8 (Galway, 1956). The hodograph in Fig. 24 shows sharp veering of the wind in the lowest few kilometers with fairly high winds aloft. This structure is typical of that usually found in supercell storm environments (Chisholm and Renick, 1972; Barnes, 1978; Barnes and Nelson, 1978).

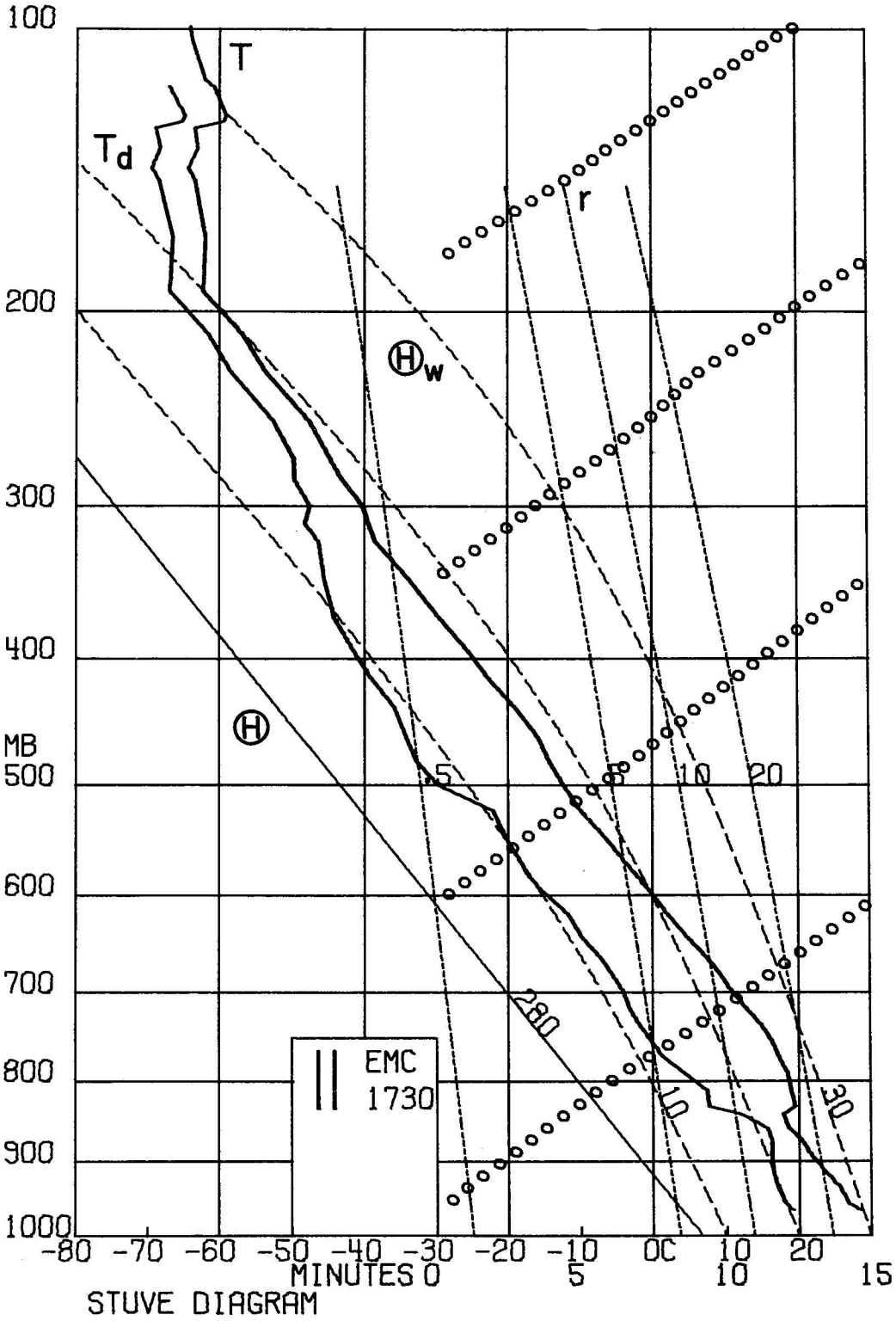

Figure 23. Sounding data from Elmore City radiosonde site. Instrument package was launched at 1730 CST on 29 May 1976. T - temperature; T_d - dewpoint; θ, θ_w - dry and wet adiabats; r - mixing ratio (g kg^{-1}); Open circles give time - pressure height profile of balloon (use time diagram on abscissa).

The storm first became recognizable as an entity near 1900. Figure 25 shows the radar reflectivity (0° tilt) of the WSR-57 incoherent radar at 15 min intervals from 1915 to 2100. The storm grew rapidly between 1915 and 2015 at which time it formed a hook echo which persisted until almost 2100. At this time, the cell began to weaken slowly as another cell to its south started to grow. The storm continued to propagate to the east and still possessed a large 55 dBZ core as late as 2130.

4.2 Reflectivity and Velocity Structure

Data analysis has been performed at 2032 over a 30x30x11 km box centered on the hook echo. The storm is near its most intense stage at this time. Figure 26 shows horizontal planes of reflectivity and velocity structure spaced at 1 km intervals in the vertical. The left hand grids display reflectivity at 5 dbZ intervals along with the vertical velocities. Updrafts ≥ 20 m s^{-1} are shaded with interior unshaded areas ≥ 40 m s^{-1}. Downdrafts ≤ -10 m s^{-1} are cross-hatched with interior white areas ≤ -20 m s^{-1}. The reflectivity contours (unlabeled) are repeated on the right hand grid along with the storm's relative horizontal velocity vectors. The reader may note anomalous vectors on the storm's periphery at some levels. These are caused by bad radial velocity estimates due to low returned signal that were inadvertently missed in the editing process (see Appendix A, section 2). The reflectivity field is from the Norman Doppler radar. The Norman Doppler reflectivity values are 5 to 10 dBz lower than the WSR-57 and Cimarron Doppler radars. Since the reflectivities are used only qualitatively, however, the Norman reflectivities have been retained because they have the best spatial resolution. The horizontal

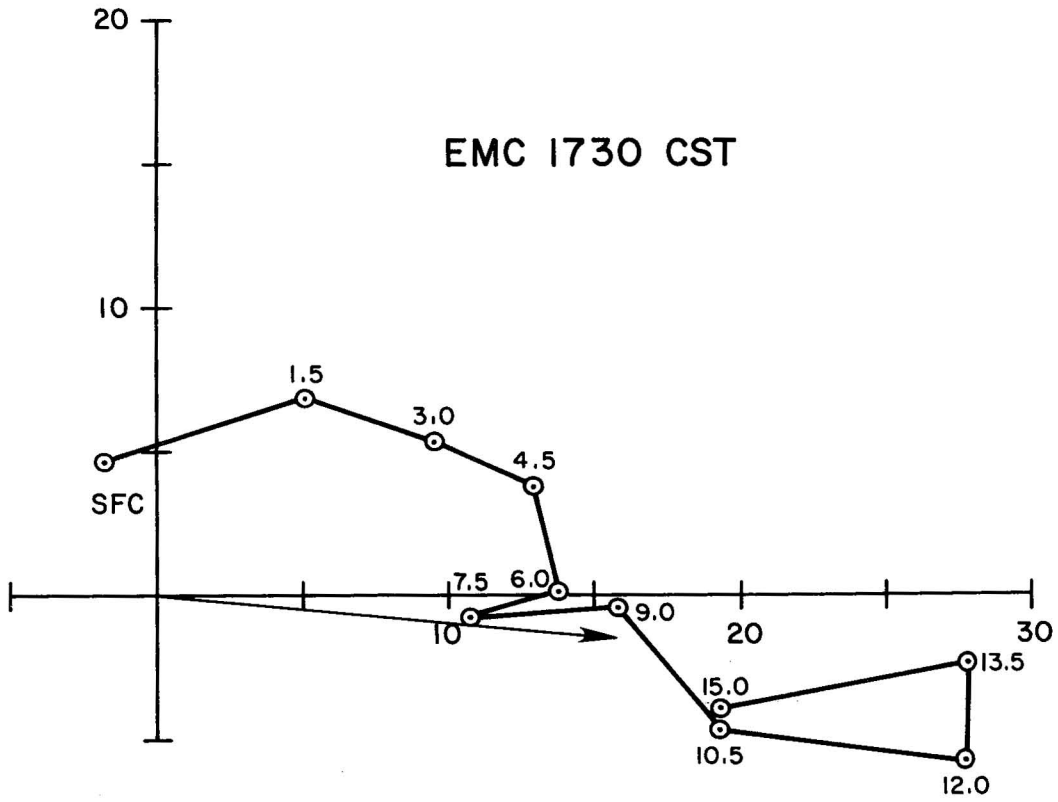

Figure 24. Hodograph of wind data from radiosonde of Fig. 23. Velocities are in m s^{-1}. Vector shows storm motion (275°/15.7 m s^{-1}).

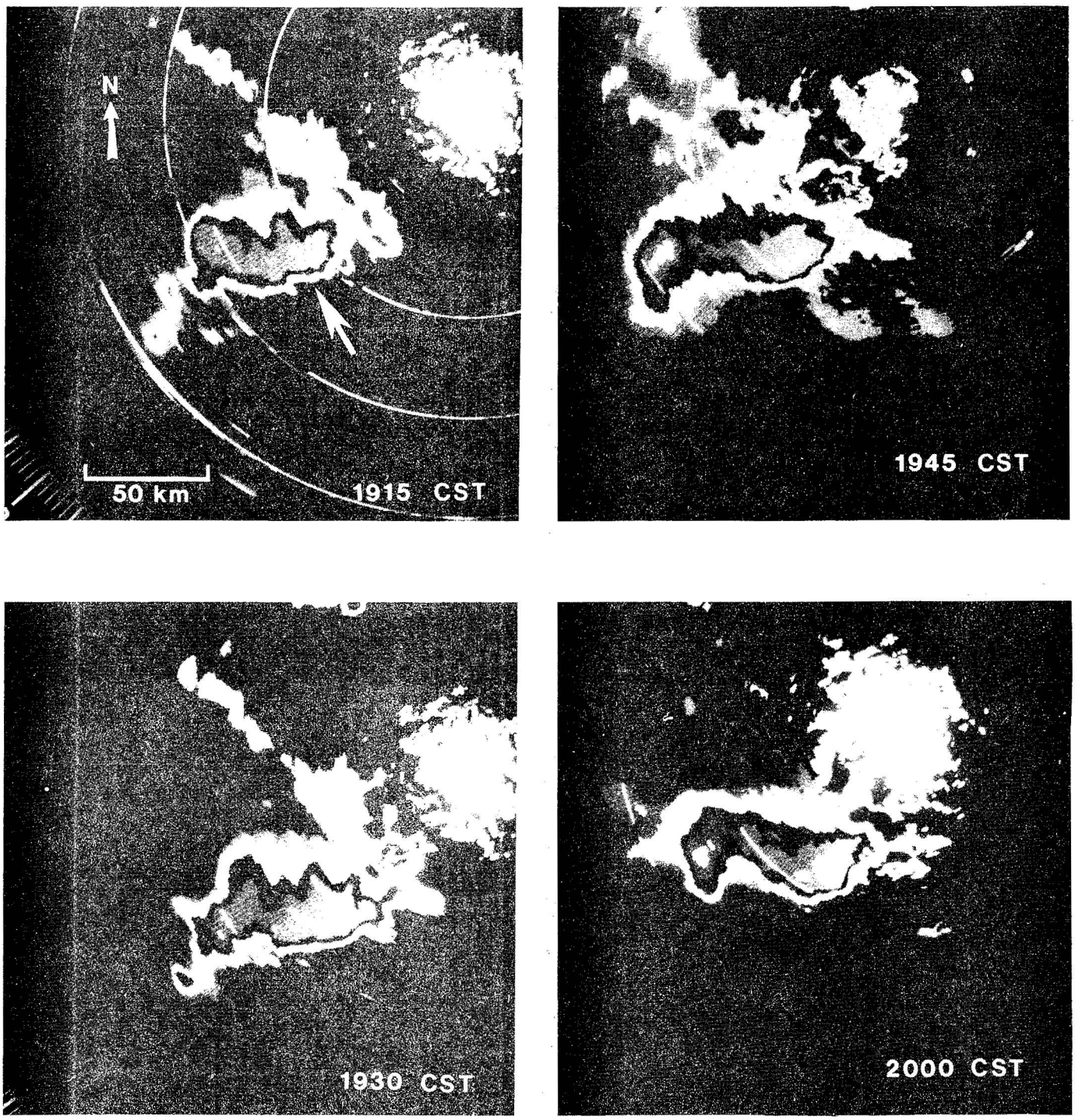

Figure 25. Radar reflectivity (0° tilt) from NSSL WSR-57 radar. Gray shade calibrations in dBZ are: dim 8-14; bright 20-28; cancel (dark) 29-39; dim 40-50; bright 51-61. The arrow on the 1915 picture shows the beginnings of the storm of interest. The "hook" is indicated by the arrows in the 2015-2045 pictures. The location of the Norman (NOR), Cimarron (CMF), and CHILL (CHL) radars are shown on the 2030 picture.

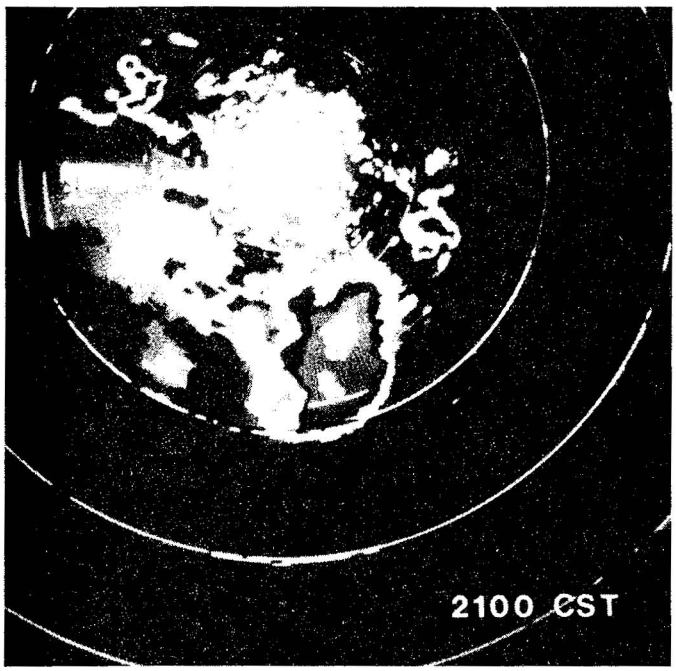
2100 CST

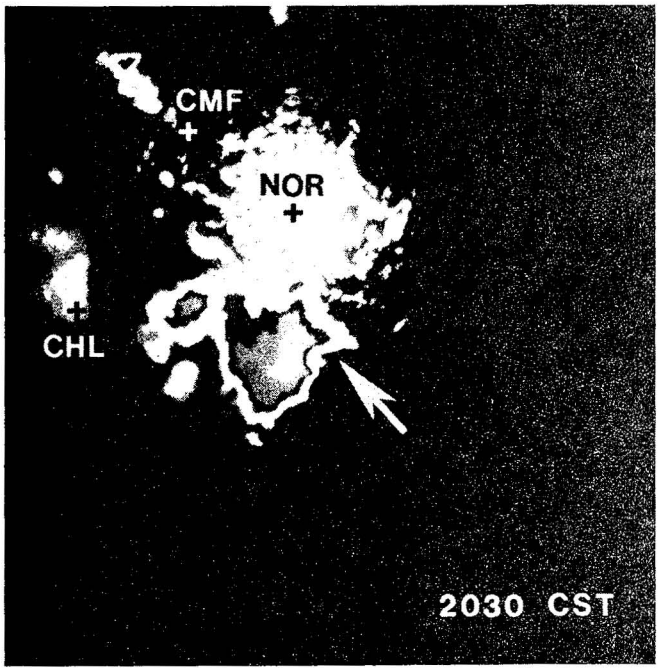
CMF
NOR
CHL
2030 CST

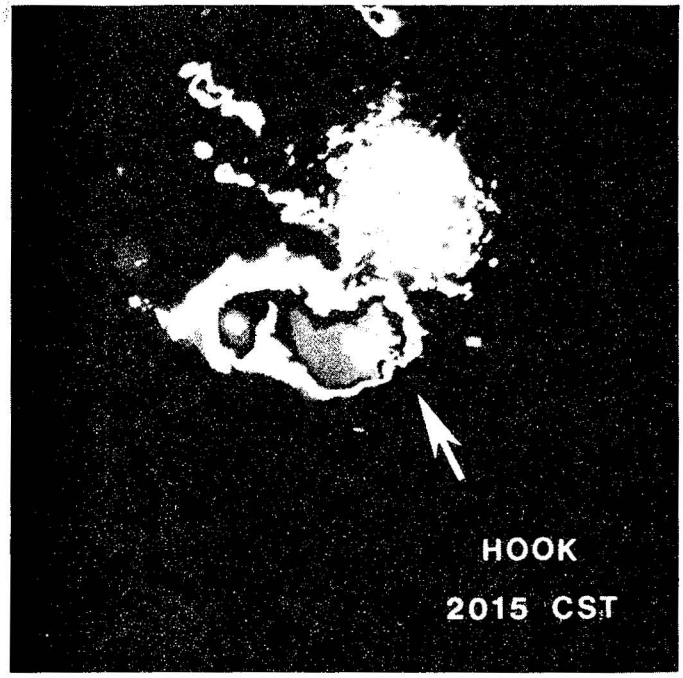
HOOK
2015 CST

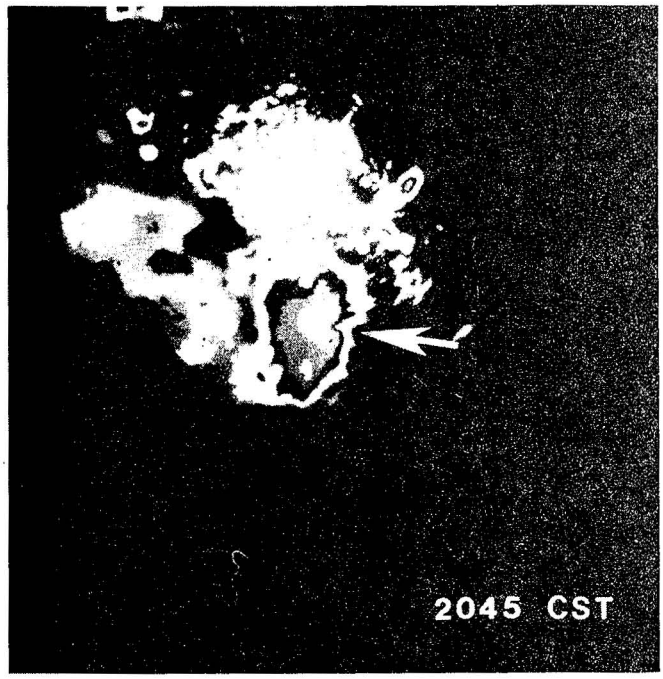
2045 CST

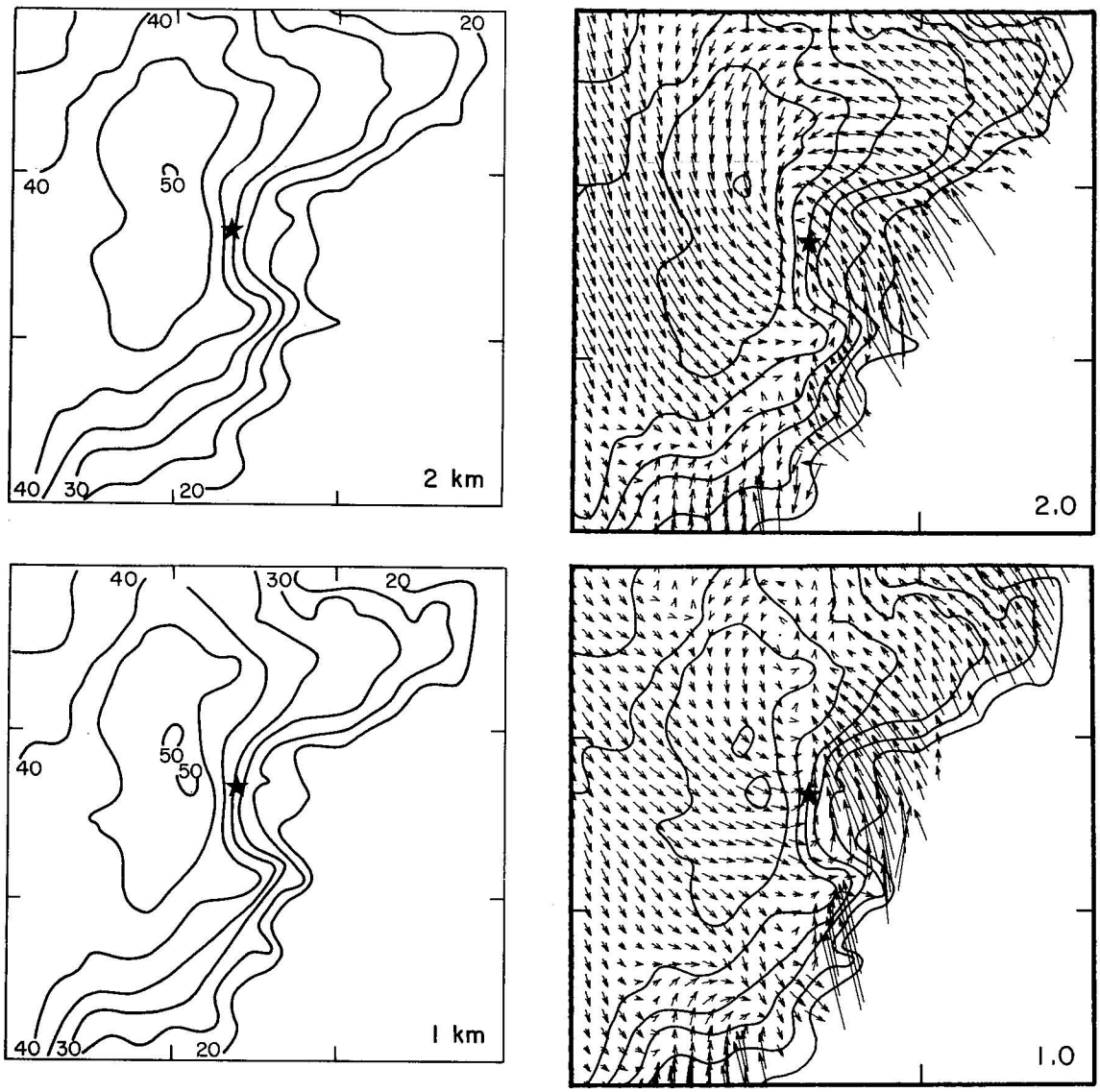

Figure 26. Reflectivity and velocity structure (relative to storm motion) of 29 May 1976 hailstorm at 2032. Data are displayed in horizontal sections at 1 km vertical intervals. Height of each section (km) is given in lower right hand corner. Tick marks are spaced 10 km apart. North is towards the top of the page and a fiducial mark (*) is given at each level. The left hand grids show reflectivities (light lines at 5 dBZ intervals) and vertical velocity. For the vertical velocities, shaded areas are updrafts $\geq$20 m s^{-1} with interior unshaded areas $\geq$40 m s^{-1}. Downdrafts $\leq$-10 m s^{-1} are cross-hatched with interior white areas $\leq$-20 m s^{-1}. The reflectivity contours (unlabeled) are repeated on the right hand grid along with horizontal velocity vectors. The vector lengths are proportional to wind speed. One km in length is equal to 10 m s^{-1} (the vectors are spaced at 1 km intervals). For reference the lower left hand corner of the grid box is located 10 km west and 75 km south of the Norman Doppler radar. The reader may wish to refer to the 2030 time of Fig. 25 to see the relationship between the storm and all three Doppler radars.

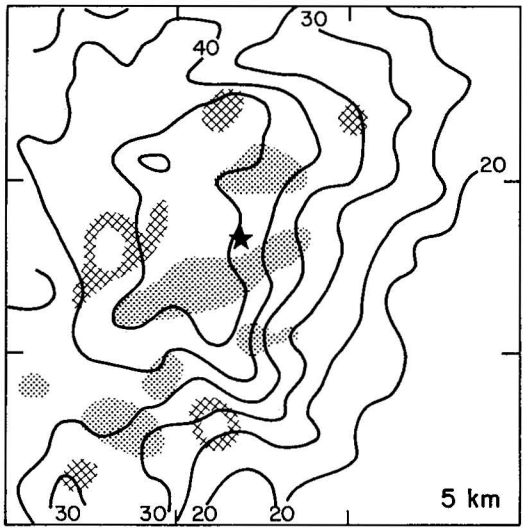
30
40
20
5 km
30
30
20
20

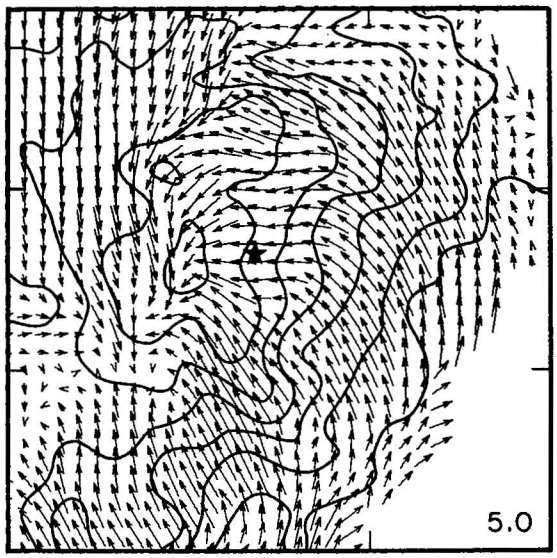
5.0

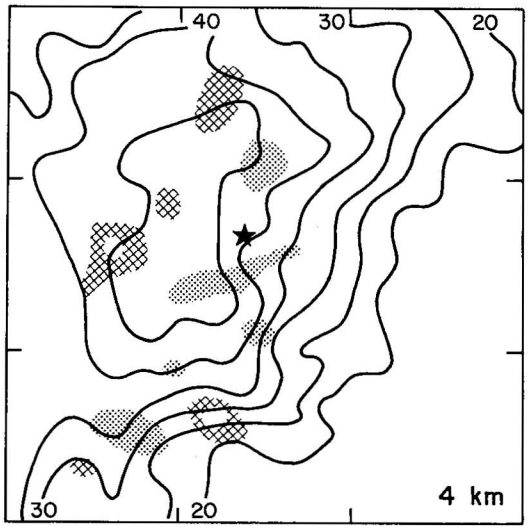
40
30
20
4 km
30
20

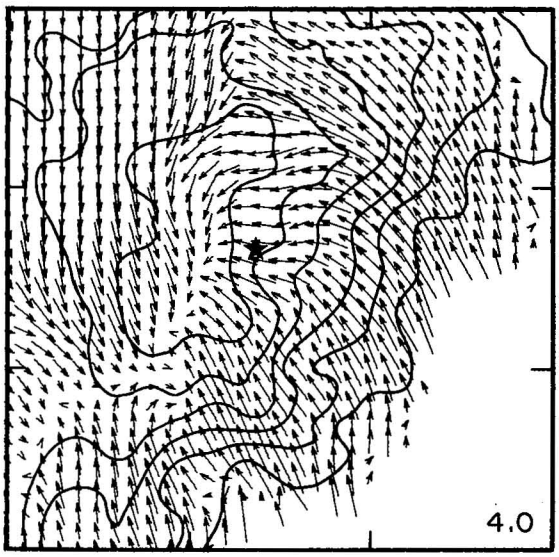
4.0

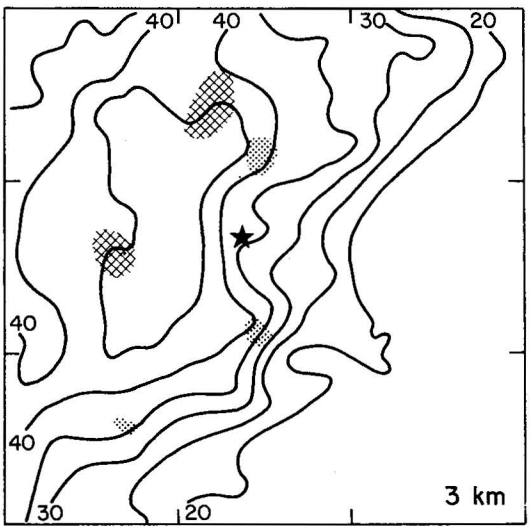
40
40
30
20
40
40
3 km
30
20

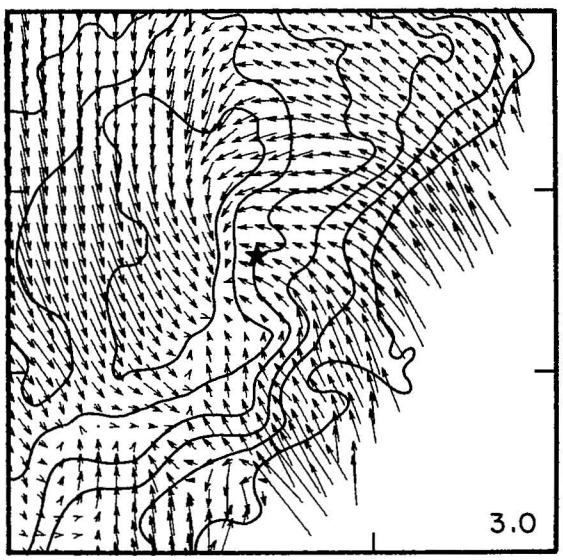
3.0

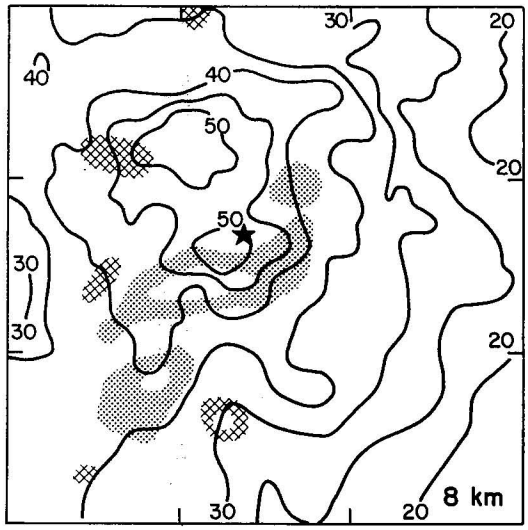
40
30
20
50
8 km

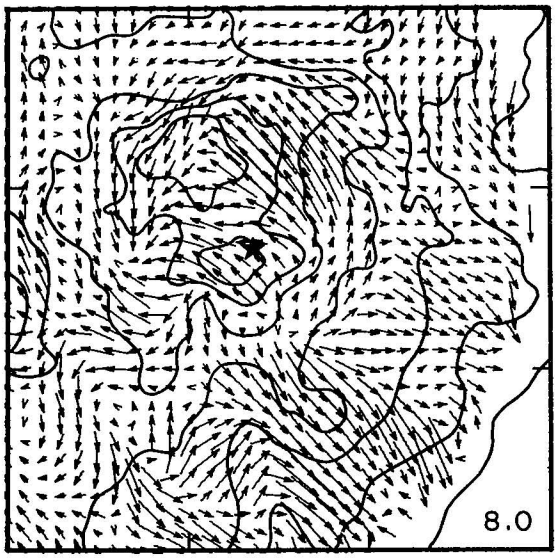
8.0

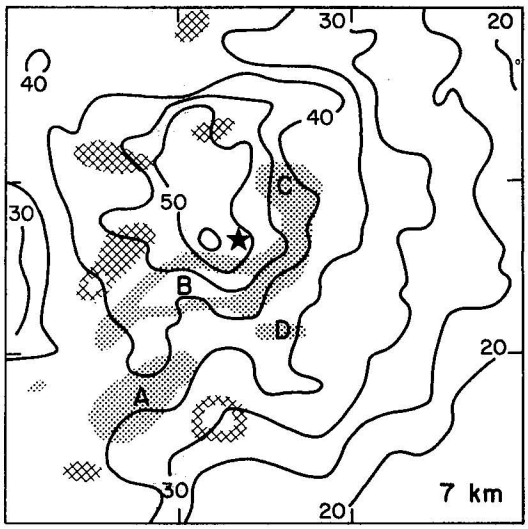
40
30
20
50
A
B
C
D
7 km

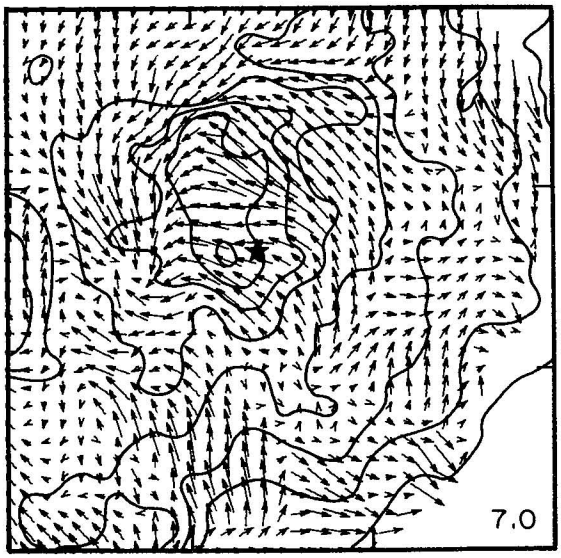
7.0

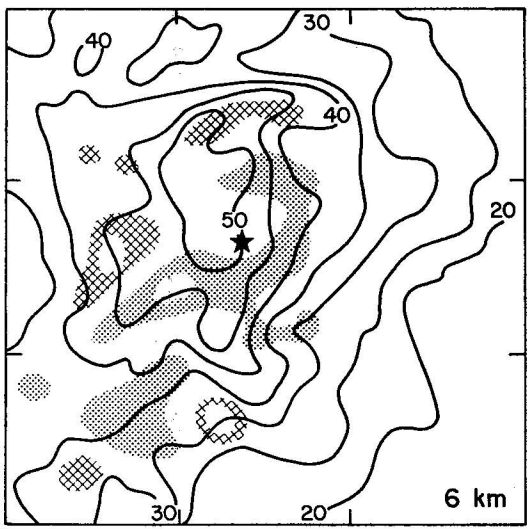
40
30
20
50
6 km

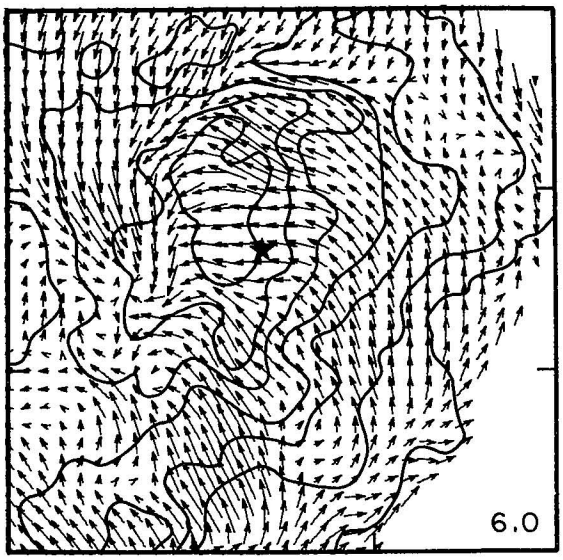
6.0

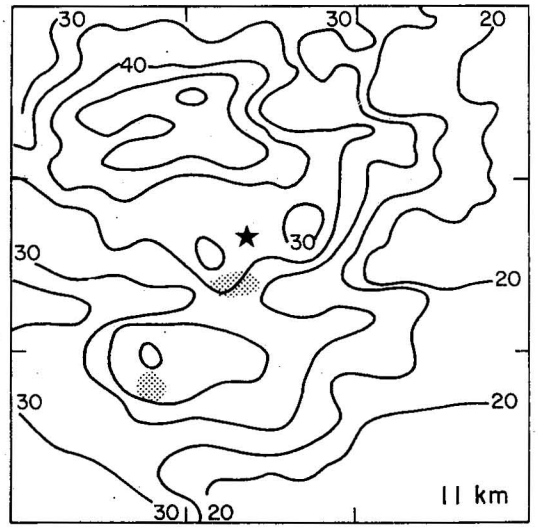
30
30
20
40
30
30
20
30
20
30
20
11 km

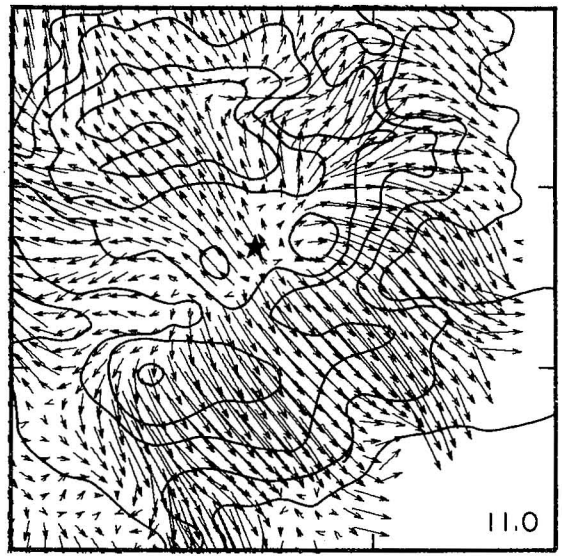
11.0

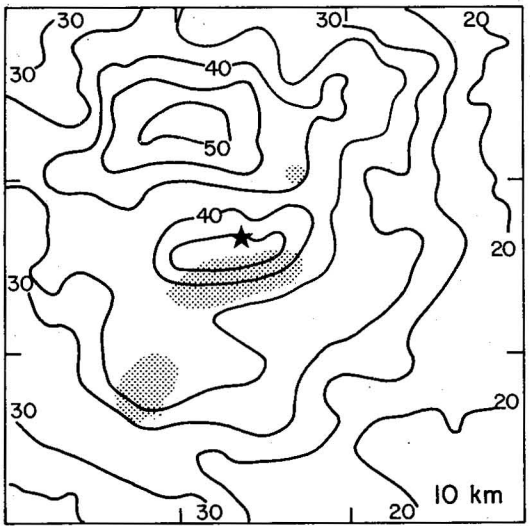
30
30
20
30
40
50
40
20
30
20
30
20
10 km

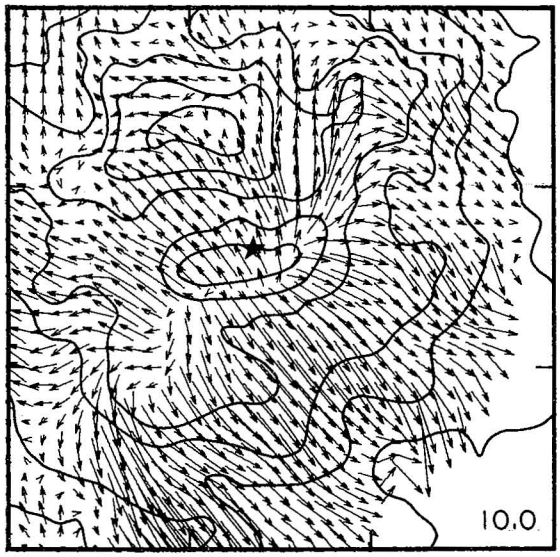
10.0

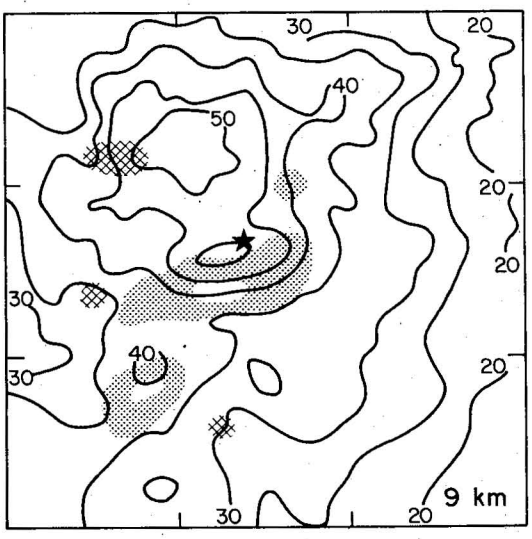
30
20
40
50
20
20
30
40
20
30
20
9 km

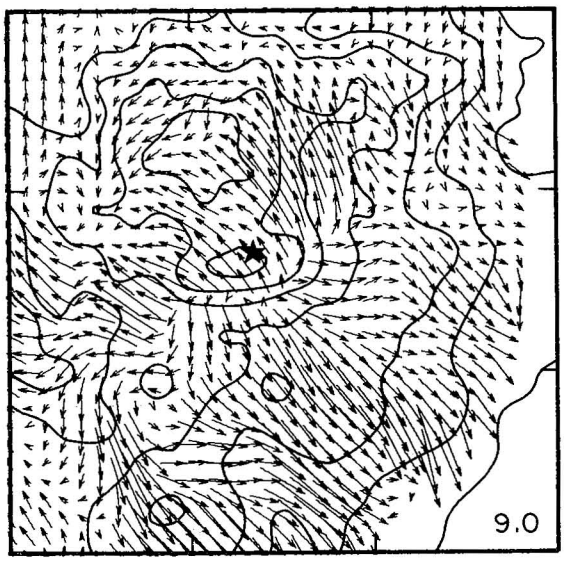
9.0

wind field was derived directly from Eq. (3) and the vertical velocities were calculated by integrating from the top down using technique 4 described in 2.5.2.

The reflectivity field is very characteristic of a supercell storm with a hook echo in the lower levels (Fig. 26) and a large overhang region aloft (Figs. 14 and 26). A weak echo region (WER) can be seen at 5-8 km in Fig. 26, appearing as an inverted "v" shaped notch just south of the high reflectivity core. The raw Doppler data (not smoothed by interpolation and not shown) shows this region is bounded (BWER) between 5 and 7 km. At and below 4 km the WER has filled in with higher reflectivity which may indicate the updraft has just begun to weaken.

The horizontal velocity vectors at 1 km indicate a moderately strong circulation associated with the reflectivity hook echo. Calculated divergence and vorticity in this region (not shown) are about equal with maximum values of 1.0 to 1.5 10^{-2} s^{-1}. A convergence line extends southwestward from the circulation forming the storm's gust front. In the middle levels, the dominant feature is the convergence area ($\approx$1.5 10-2 s^{-1}) just to the west of the high reflectivity core (see especially the 7 km level). This gives rise to the storm's main downdraft. At and above 9 km the flow is characterized by a long and strong (>1.5 10^{-2} s^{-1}) divergence line. This strong outflow is responsible for the storm's large overhang.

Four major updrafts are revealed by the Doppler analysis. Three are aligned SW-NE as can best be seen on the 7 or 8 km horizontal vertical velocity sections of Fig. 26. For discussion, the cores are identified on the 7 km section as A, B, and C progressing from SW to NE. Core D is the small updraft maximum to the southeast of core B.

The center draft (core B) is the largest and strongest with maximum vertical velocity of 51 m s^{-1} at a height of 7 km. It is associated with the BWER and appears to have its roots in the convergence area centered on the low level circulation. The companion downdraft (hence forming the classical couplet) is located just west of the updraft. The downdraft reaches a maximum speed of 25 m s^{-1} at a height of 5 km.

Core C's low level updraft roots likewise appear to be in the region of the hook echo. This updraft, however, is weak and has no well defined maximum. The greatest vertical velocities are a nearly constant 27 m s^{-1} between 6 and 9 km. There is also a weak downdraft to core C's northwest.

Core A has formed on the gust front boundary to the southwest of the convergence area associated with cores B and C. At the low levels it has two distinct updraft maxima, but above 7 km these have merged into one. While smaller and somewhat weaker than core B (maximum speed of 42 m s^{-1} at 9 km), this core appears to be actively growing. By 2045, it has formed its own high reflectivity core at the surface (Fig. 25). It continues to grow as core B declines, but it never dominates the complex. Core A has two downdrafts near it. The one to the southwest is fairly weak. A weak downdraft would be expected with a cell that is still mainly in the cumulus growth stage (Byers and Braham, 1949). The downdraft to the east of core A, however, is fairly intense. It forms aloft in response to convergence at about 7-9 km and diverges somewhere near the gust front at the surface.

Like core A, core D appears to stem from the convergence area on the storm's gust front. Analysis of the unsmoothed reflectivity data reveals a maximum associated with this updraft. This is interesting in that it shows the southern

boundary of the high reflectivity forming the hook echo is convective in nature. The updraft reaches its maximum velocity ($\geq$35 m s^{-1}; note only one grid point was ~30 m s^{-1}) between 5 and 6 km. Its magnitude decreased rapidly above 7 km.

4.3 Summary

In general, the horizontal flow and reflectivity are typical of that previously observed in other supercell type storms. There is little past data, however, on vertical velocity structure. Two studies (Heymsfield, 1978; Brandes, 1978) address in some detail vertical velocity in a supercell storm. Both were dual Doppler analyses and obtained the vertical component of motion by integrating the continuity equation upwards. Their analyses were restricted to levels at and below 6 km. These studies showed not only one strong updraft and a weaker downdraft, but also other substructures. The maximum updraft values in both cases were around 40 m s^{-1} at their top analyses levels (~6 km). It is likely these solutions are suffering from the error amplification described in Chapter 2. They do, however, agree with maximum values found in this study at the 6 km level. Conceptual models usually show only one strong and broad updraft with an accompanying downdraft. For this storm, the dominant vertical draft structures (core B and its downdraft) do exhibit these classical characteristics. There are, however, other updrafts.

It is difficult to interpret the nature and/or importance of updraft cells A, C, and D without several complete three-dimensional views spaced at close time intervals. Some speculation on the roles of these three updrafts, however, is appropriate. Core C appears to stem from the same low level convergence region as the main updraft (core B). These two cells may be pulsations on a general updraft region (Nelson and Braham, 1975). If this is the case, then data with good temporal resolution and an analysis that allows time variations would be necessary to ascertain the effects, if any, of such pulsations. Inspection of the reflectivity data shows that, for most hail growth times (10-20 min), the basic storm structure in this area changes little. The hail growth model (see Chapter 5) also reveals that core C has little effect on hail production.

Cores A and D are probably more important to hail growth. They both form on the gust front in an area where either "feeder" (flanking line) or "daughter" cells would normally grow (Browning, 1977). Core D has the instantaneous appearance of a feeder cloud. It is small, in close proximity to the main updraft, and imbedded in flow that would cause it to merge with the main updraft. It is not known if this merger occurs. Cell A is larger in extent and eventually forms its own high reflectivity core (Fig. 25, 2045 and 2100). This core, however, does not merge with the main cell as a feeder cloud normally would, nor does it grow to dominate the complex as a daughter cloud. Its evolution may be altered from what normally may have occurred due to the demise of the entire storm complex after about 2100. In any event, at our analysis time (2032) cells A and D are configured very much like feeder and/or daughter cells and will be considered as such for the discussion of the hail growth processes.

Figure 27 is a three-dimensional composite of important storm features. At the surface, the gust front has advanced well ahead of the main updraft's position aloft (core B). This may account for the decay of this portion of the storm over the next half hour. Core D appears to be growing in the area of enhanced convergence along this portion of the gust front. The 7 km section shows that, at least aloft, updraft B still dominates the complex. A weak echo region is evident in the 40 dbZ contour near core B's center. Interestingly, while the absolute updraft

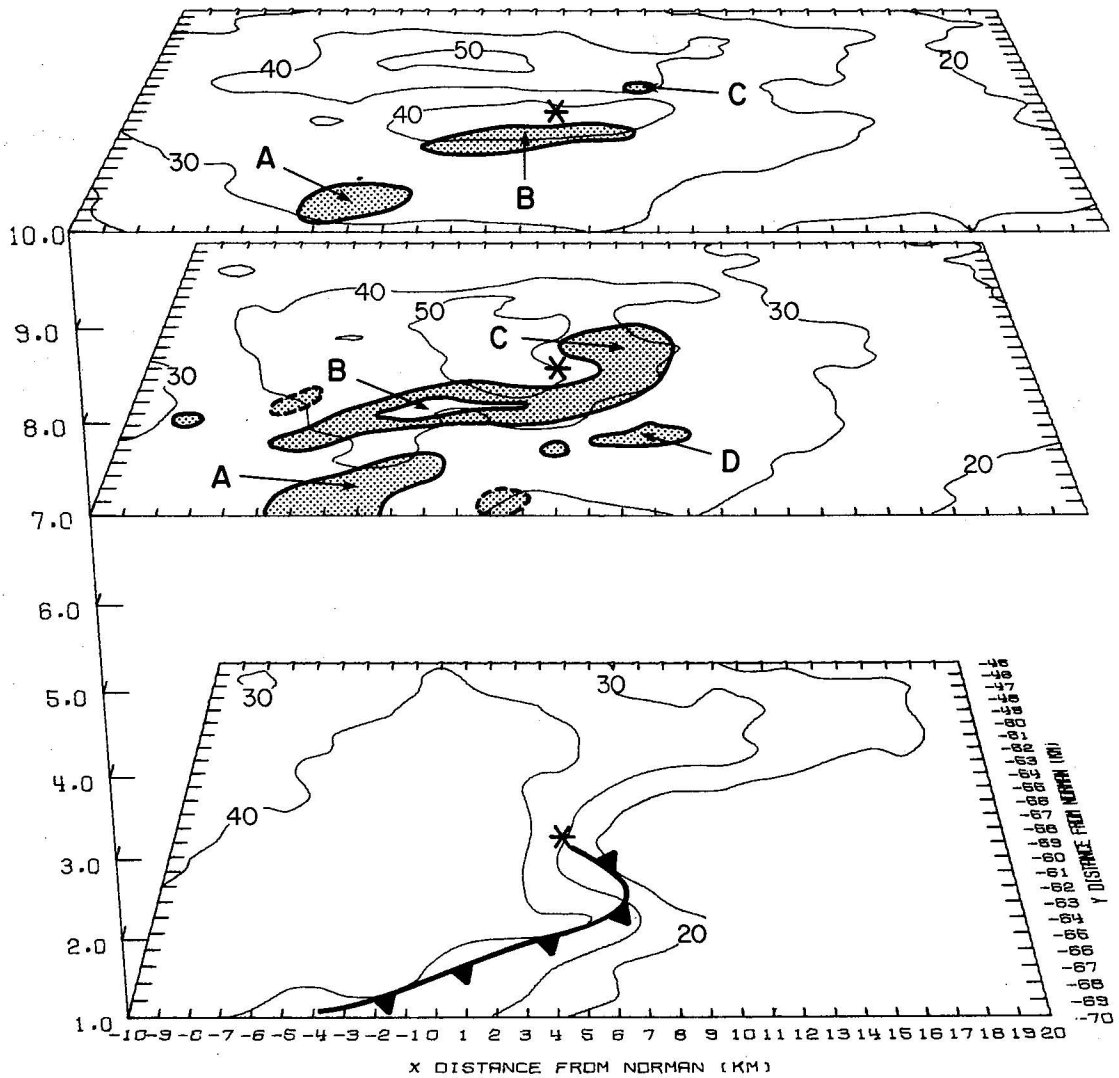

Figure 27. Three-dimensional perspective view of important features of 29 May 1976 storm at 2032. The vertical scale has been expanded by a factor of three. The viewer is looking directly towards the north. Data are shown at three levels (1, 7, and 10 km). Light lines are reflectivity labeled at 10 dBZ intervals. Shaded regions outlined with heavy black lines are updrafts greater than 20 m s^{-1}. Unshaded areas interior to these are updrafts greater than 40 m s^{-1}. Shaded areas with dashed outlines are downdrafts greater than -20 m s^{-1}. Low level gust front is shown at 1 km by heavy black line with barbs. Indicated updraft cores and fiducial marks are the same as those in Fig. 26.

maximum is near the weak echo region, updraft B is quite extensive. The importance of this large updraft area will be elaborated on in Chapter 5.

5. HAIL GROWTH MODEL: RESULTS

5.1 Introduction

Basic model features were described in Chapter 3. The analysis technique used begins embryo growth at 2 km intervals in the horizontal and at 1 km intervals in the vertical throughout a subgrid of the volume displayed in Fig. 26. In the horizontal, the subgrid is a 22x22 km area centered on the 30x30 km analysis

region (see Fig. 28). In the vertical, the subgrid lies between 4 and 10 km (inclusive). This subgrid was chosen partially because of computer storage limitations and partially because it includes the major storm updraft regions. Initial embryo diameters are 2, 6, and 10 mm which encompass the usually observed embryo sizes (Knight and Knight, 1970). Total number of stones grown were 1008 for each of the three initial embryo diameters.

In the subsequent subsections several topics are discussed pertaining to the model results. First the model output is checked for realism. It is of little value if it can not reproduce the salient hail characteristics of the storm. The following two sections describe general hail growth characteristics and specific trajectories. This leads to speculation on embryo sources and important factors for favorable hail growth.

5.2 Model Realism

Unfortunately, the storm was not in a location where detailed hail fallout information could be obtained from the NSSL volunteer observer network (Nelson and Young, 1979). NOAA Storm Data (U.S. Department of Commerce, 1976) did report maximum hailstone diameters of 4 to 5 cm, but provided no information on areal extent. Maximum diameter hail produced by the model was 5.8 cm. Considering that melting is not included in the model, this is in good agreement with the NOAA report.

Another factor to be checked is whether the large hail falls out in the storm's high reflectivity core. Figure 28 shows, at the lowest analysis level (1.0 km AGL), the storm reflectivity field and horizontal location of each hailstone that grows to a diameter ≥1.0 cm for initial embryos of 2 and 6 mm, and diameters ≥1.5 cm for 10 mm embryos.[3] All trajectories are computed with winds relative to

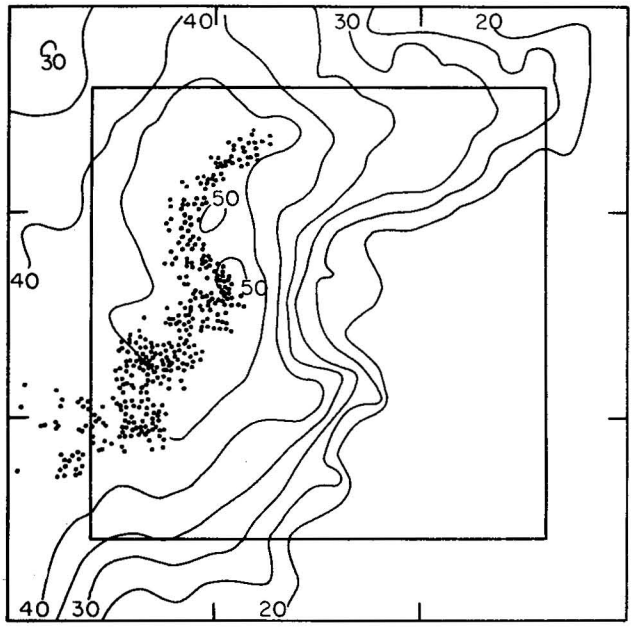

Figure 28. Position of model hailstones at 1 km AGL as they exit the model domain ("fallout" positions). The dots represent hailstones with diameters ≥1.0 cm for D_o's of 2 and 6 mm, and diameters ≥1.5 cm for D_o's of 10 mm. The reflectivity field (dBZ) is also shown. The interior 22 22 km box shows the horizontal extent of embryo starting locations (vertical extent was 4 to 10 km). Tick marks are at 10 km intervals.

[3] In the analysis of the hail model, only model hailstones that grow "significantly" will be discussed. For initial embryos of 2 or 6 mm, significant growth is arbitrarily defined as having occurred if the hailstones reach diameters ≥1.0 cm. For embryos with initial diameters of 10 mm, this limit is 1.5 cm.

storm motion; therefore, even though the hailstones do not fall out at the same time, their locations are correct relative to the reflectivity field. The interior 22x22 km box shows the horizontal extent of the starting embryo locations for each height. Considering the large horizontal and vertical extents of these starting locations, the concentration of hailstones is quite remarkable. In general, they fall along the Norman radar's 45 dBZ core axis. (The reader should remember that this Z_e value is about 10 dBZ too low.) The stones that fall to the reflectivity core's southwest mostly originate near updraft core A. They arrive at the surface about 10 min after the model start time (2032). Note on Fig. 25 this area of the storm has formed a high reflectivity core by 2045.

Nelson and Young (1979) found that supercell storms in Oklahoma produce hailswaths with mean widths of 18.1 km (standard deviation, 7.6 km). Using the measured storm motion (275°/157 m s^{-1}) and assuming steady state conditions, the model predicts the storm would produce a swath 18 km in width (Fig. 29) in excellent agreement with Nelson and Young.

5.3 Embryo Source Regions and General Hail Growth Characteristics

It is not necessarily to be expected that hail embryos of different sizes are distributed uniformly throughout the storm volume as has been assumed in this model. This technique, however, does identify potential hail producing areas and reveals general growth characteristics. Using reasoning based on knowledge of storm structures, this analysis leads to speculation on natural embryo sources. It also points out locations where artificially induced embryos can be injected to compete for available liquid water whether natural embryos are present or not.

A summary of the mean growth characteristics are given in Table 4. The listed data apply only to hailstones that reach diameters ≥1.0 cm for D_0's of 2 and 6 mm, and ≥1.5 cm for D_0 of 10 mm. The number of hailstones that grow to these sizes is really quite small considering there were initially 1,008 in each

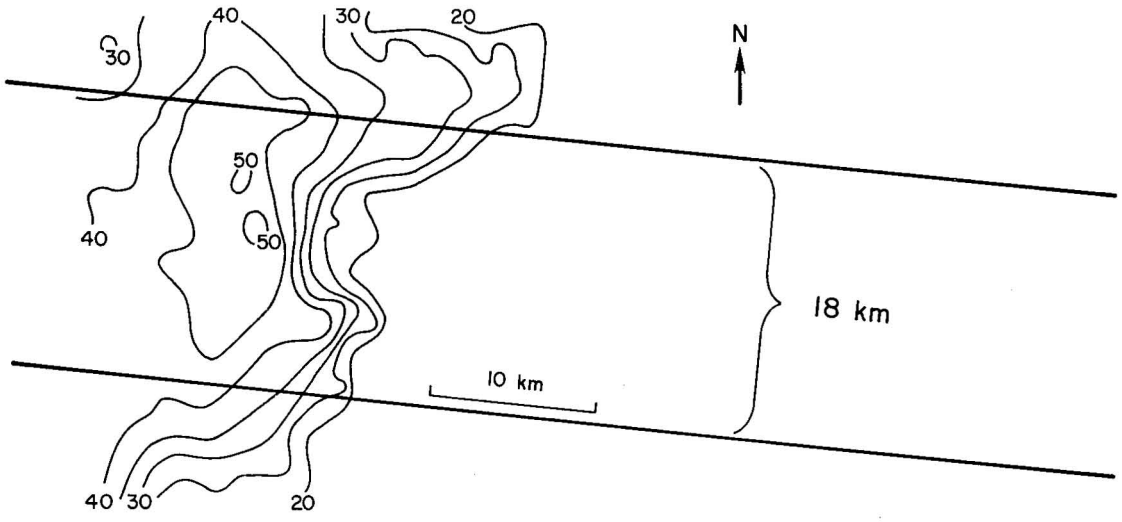

Figure 29. Hailswath (heavy black lines) predicted by model using storm motion of 275°/15.7 m s^{-1}. Reflectivities are repeated from Fig. 28.

Table 4. Mean growth characteristics for hailstones with final diameters ≥1.0 cm for D_o's of 2 and 6 mm, and for final diameters ≥1.5 cm for D_o of 10 mm. The numbers shown in parenthesis are standard deviations.

D_o (mm)	Number	Mean Diameter (cm)	Mean Growth Time (min)	% of Stones that Experience Wet Growth	Mean % of Time in Wet Growth	Mean % of Mass Accumulated in Wet Growth
2	114	1.3(0.45)	13.3(5.1)	60.5	17.7(13.0)	26.8(21.6)
6	189	1.3(0.56)	8.6(3.8)	76.2	35.5(18.9)	45.7(23.6)
10	134	1.9(0.59)	7.3(3.2)	84.3	41.5(23.7)	52.3(27.4)

size category. This implies only a small volume of the storm can produce large hail. Interestingly, the spread in the mean final diameters is much less than the spread of D_0. In fact, the mean diameters for D_0's of 2 and 6 mm are both 1.3 cm. Expectedly, the mean growth times (interval between the model's start time and the fall of the hailstone below the melting level) show an inverse relationship with D_0. Overall, these times are fairly short which lends credence to the assumption of stationarity of the Doppler derived wind field over the hail growth periods.

A key factor in hail production is the occurrence of wet growth due to its significance to modification attempts. During wet growth, ice crystals are collected as readily as liquid water. In mixed phase growth zones, therefore, enough liquid water must be converted to ice to prevent wet growth. If the wet growth cannot be prevented, then the total amount of water mass available for hail growth remains constant. In addition, since the cloud ice has already undergone a phase change, there is no latent heat associated with its collection, and the growth may actually proceed at an accelerated rate. This process will be elaborated on later. Table 4 lists the percentage of hailstones that experience "significant" wet growth. "Significant" is defined as wet growth of duration >30 sec that occurs other than in the last 30 seconds just prior to the hailstone falling through the 0° level (almost all hailstones undergo wet growth during this time period). As can be seen, the percentage increases with increasing D_0, but is high in all cases. The actual time spent in wet growth regimes is relatively low (mean percentages of 17.7, 35.5, and 41.5), but the mean percentage of mass acquired by the hailstones during these times is significant (26.8, 45.7, and 52.3%). Certainly, wet growth plays a significant part in hail growth in this storm.

Contours of final hailstone diameter as a function of initial embryo diameter (D_0) and location are given in Fig. 30. For example, the 1.5 cm contour on the middle panel of the 5 km section of Fig. 30 surrounds the beginning locations of all hailstones that grow to a diameter ≥1.5 cm. For orientation, radar reflectivity and updraft areas are also indicated. The top, middle, and bottom panels are for D_0's of 2, 6, and 10 mm, respectively. Heights of each level and the environmental and adiabatic core temperatures are shown at the top of each sequence. In addition, Table 5 summarizes the number of grid locations (hence areas) that produce hail of a given size as a function of initial height and D_0.

For D_0 = 6 mm the initial growth area that produces hail ≥1.0 cm maximizes in the 6 to 7 km range (Table 5 and Fig. 30). This area lies to the southeast of the three major updraft cores in a corridor (hereafter called embryo corridor) that is aligned from southwest to northeast. Note this is upwind of the updraft cores with respect to the prime growth height around 6 to 7 km (T_a = -8 to -15°C). The embryo corridor's width gradually grows and then narrows with height. Embryos that are too near the updraft's center are usually carried aloft where growth is limited by low liquid water content. Embryos too far to the southeast cannot be supported by the weak updrafts. They, therefore, sink to lower levels where the water content is too low, the temperatures too warm, and the updrafts too weak to allow much growth.

This pattern also prevails for the other two D_0's although, as a general rule the smaller D_0, the further away its initial position must be from the updraft core in order to produce large hail. It should be noted that except for a few cases to be discussed later, the largest hail always starts several kilometers from the major updraft cores. One interesting point for D_0 = 2 mm is the lack of a preferred initial growth level above 5 km (see Table 5). This implies a very deep layer over which small embryos can begin their growth to become large hail.

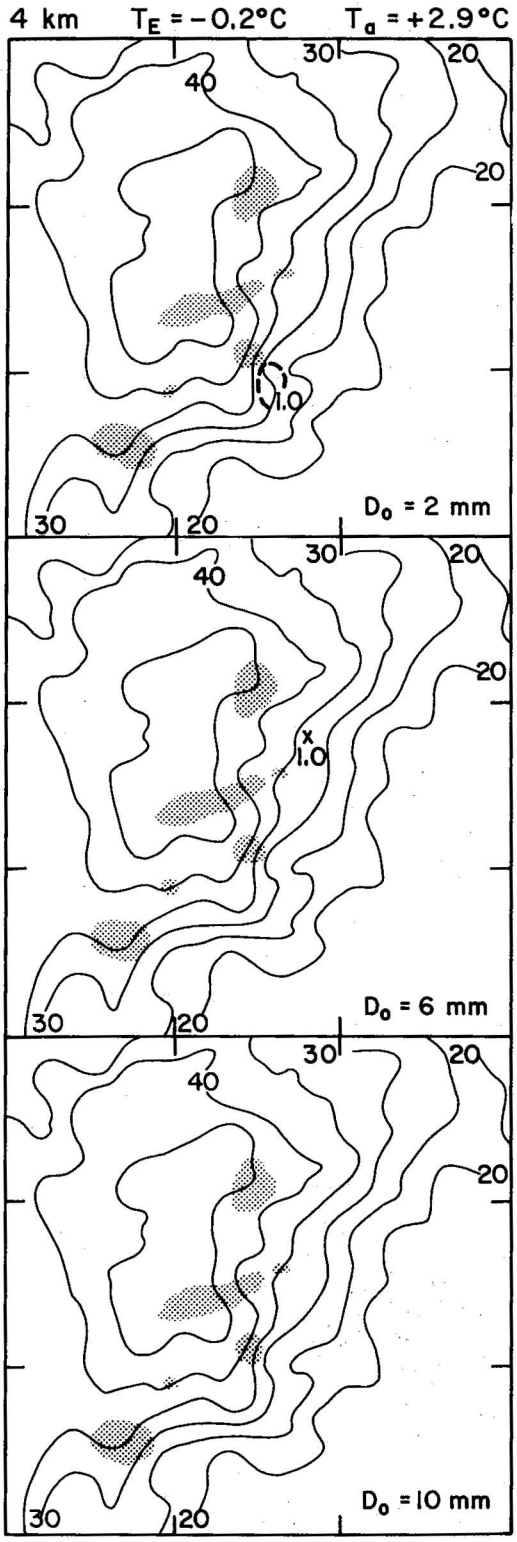

Figure 30. Contoured values of final hailstone diameters (cm, dashed heavy lines) as a function of initial embryo size and location. That is, the contours enclose regions from which embryos emanate and eventually grow to diameters indicated by the contour magnitude. The thin lines are reflectivity (dBZ). Shaded areas denote updrafts ≥20 m s^{-1} with interior unshaded areas representing updrafts ≥40 m s^{-1}. For the top, middle and bottom panels D_O=2, 6, and 10 mm, respectively. Cross-section heights, environmental and adiabatic core temperatures (T_E, T_a) are shown at the top of each sequence.

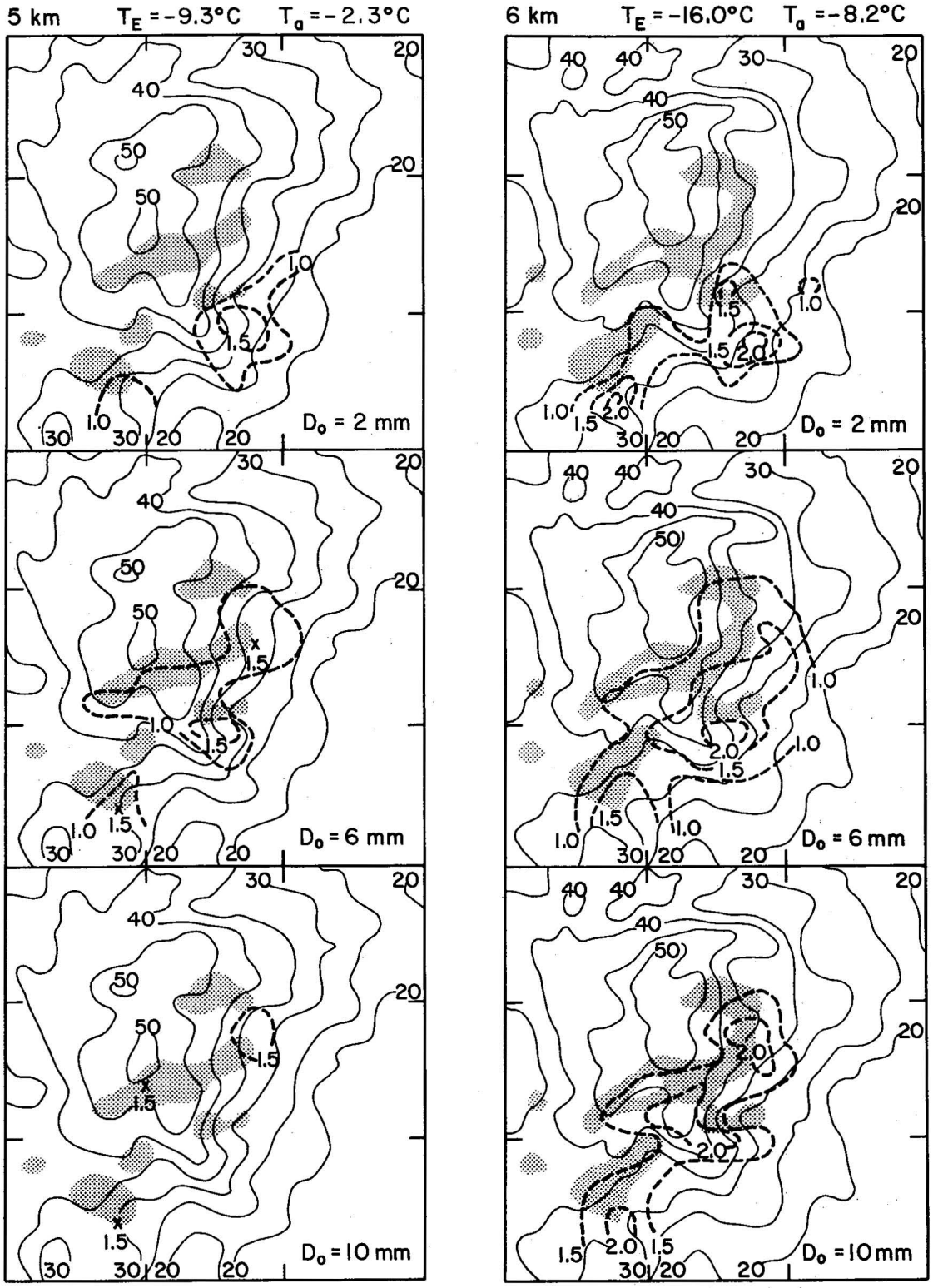
5 km T_E = -9.3°C T_a = -2.3°C
6 km T_E = -16.0°C T_a = -8.2°C
D_o = 2 mm
D_o = 6 mm
D_o = 10 mm

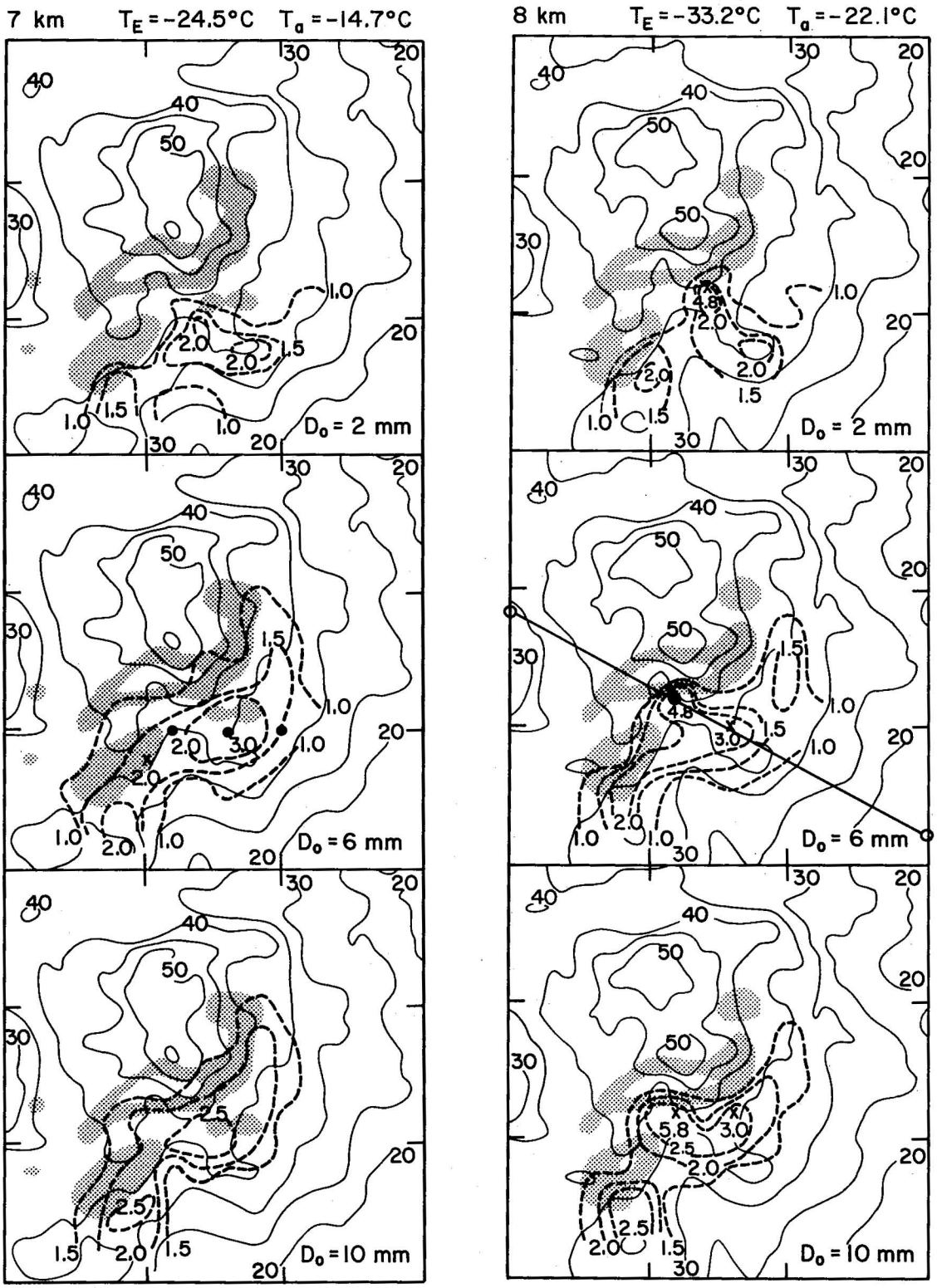
7 km T_E = -24.5°C T_a = -14.7°C
D_o = 2 mm
D_o = 6 mm
D_o = 10 mm
8 km T_E = -33.2°C T_a = -22.1°C
D_o = 2 mm
D_o = 6 mm
D_o = 10 mm

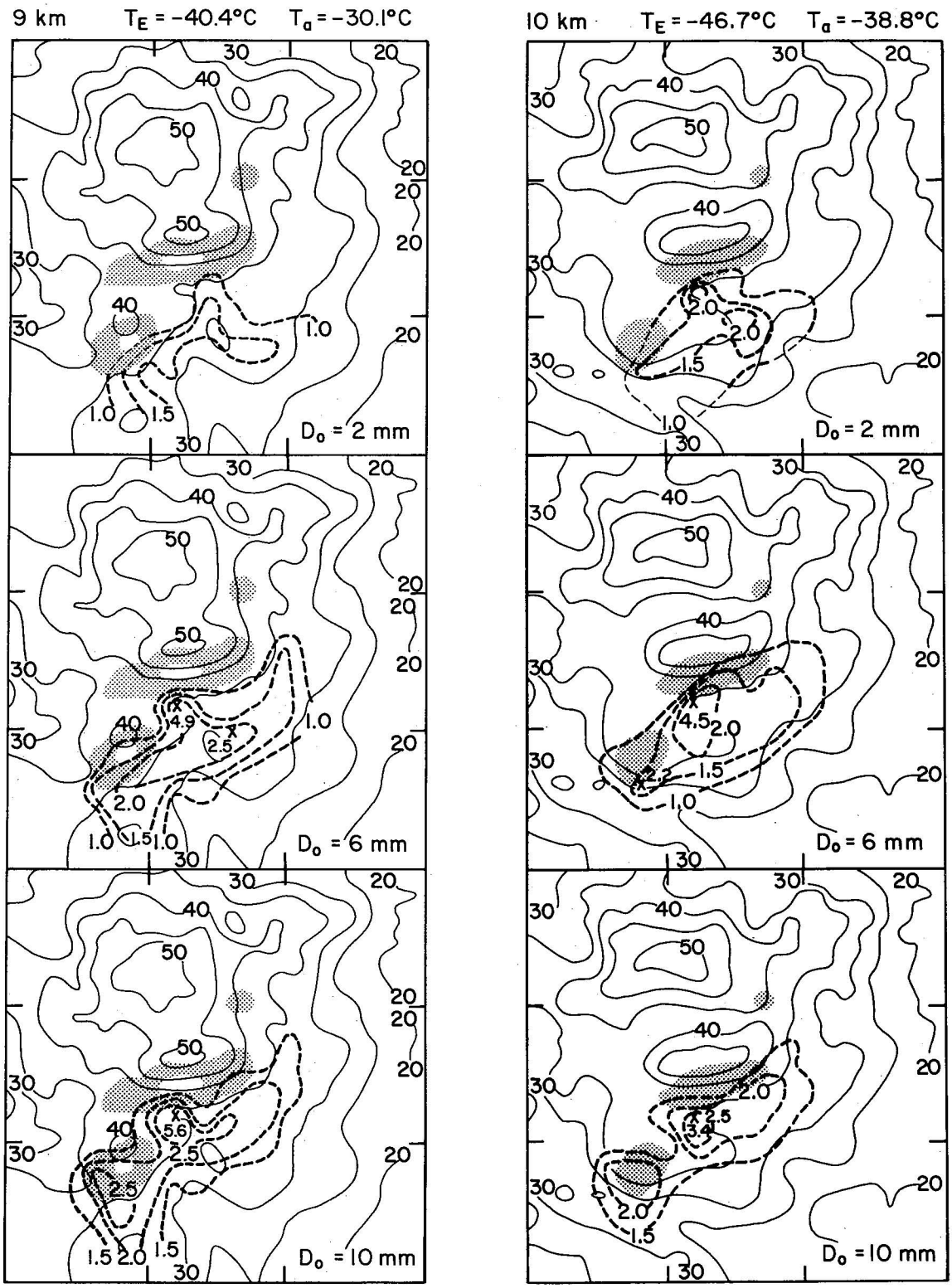
9 km
T_E = -40.4°C
T_a = -30.1°C
D_o = 2 mm
D_o = 6 mm
D_o = 10 mm
10 km
T_E = -46.7°C
T_a = -38.8°C
D_o = 2 mm
D_o = 6 mm
D_o = 10 mm

Table 5. Number of model grid positions that produce hail of a given size as a function of initial height and diameter (D_o).

Height (km)	1.0	1.5	2.0	2.5	3.0	3.5	4.0	4.5	5.0	5.5	Total	%
					D_o = 2 mm							
					Final Hailstone Diameter (cm)							
4	2										2	1.8
5	9	3									12	10.5
6	13	3	2								18	15.8
7	12	6	1	1							20	17.5
8	8	9	2					1			20	17.5
9	13	8									21	18.4
10	13	6	2								21	18.4
Total	70	35	7	1				1			114	
%	61.4	30.7	6.1	0.9				0.9				
					D_o = 6 mm							
4	1										1	0.5
5	23	2									25	13.2
6	24	17	1								42	22.2
7	24	10	6		1						41	21.7
8	15	8	5	1	1			1			31	16.4
9	12	7	4	1				1			25	13.2
10	10	11	2					1			24	12.7
Total	109	55	18	2	2			3			189	
%	57.7	29.1	9.5	1.1	1.1			1.6				

Table 5 (Cont'd)

D_o = 10 mm

Height (km)	1.0	1.5	2.0	2.5	3.0	3.5	4.0	4.5	5.0	5.5	Total	%
4	-										0	0.0
5	-	6									6	4.5
6	-	19	9								28	20.9
7	-	11	14	5							30	22.4
8	-	9	5	8	1					1	24	17.9
9	-	10	9	6						1	26	19.4
10	-	10	7	2	1						20	14.9
Total	-	65	44	21	2					2	134	
%	-	48.5	32.8	15.7	1.5					1.5		

In general, for a given point the larger D_0 the larger the final hailstone. There are, however, exceptions. For example, at 6 km the largest hail produced by core A (southwesternmost updraft) are from D_0's of 2 and 10 mm. This illustrates the complex feedback mechanisms in the hail growth process.

There are interesting substructures imbedded in the embryo corridor. In general, the largest hail at each level is produced in the dominant updraft (core B), even though fairly large hail (~2.5 cm) also grows in core A. (Note that almost all hailstones advect towards the northwest as they grow). Core C does produce some hail >1.0 cm, but it is not a prolific hail producer.

Anomalously large hail is formed in small areas close to the main updraft as illustrated in Fig. 30 at 8 km where 4.8, 4.8, and 5.8 cm hail are formed from D_0's of 2, 6, and 10 mm. These localized maxima (hereafter called the giant hail area, GHA) also occur at 9 and 10 km for D_0's of 6 and 10 mm. These hailstones grow to extremely large sizes while their immediate neighbors do not because of an ideal balance between several factors. Details of the growth of these as well as other hailstones are given in the next section.

5.4 Selected Growth Trajectories

The complexity of the interactions between the hailstones and the storm's thermal, moisture, and wind fields make each hailstone's growth trajectory unique. A few examples, however, demonstrate how the growth patterns shown in Fig. 30 evolved.

Figure 31 gives a three-dimensional perspective view[4] of three hailstone trajectories that grow from initial embryo diameters of 6 mm. The initial positions of these three stones, one at each side and one in the center of the embryo corridor, are shown by the dots at 7 km in Fig. 30. In Fig. 31, the initial position of the stone and its subsequent positions at two minute intervals are circled. The circles are drawn in perspective so that they become larger as the trajectory approaches the viewer and smaller as it recedes. The position of a stone as it enters a reference plane is indicated by a cross. Horizontal plan views of the same trajectories are given in Fig. 32 along with the radar reflectivity and vertical velocity fields at 7 km. Selected growth parameters are given in Fig. 33.

Trajectory 1 shows the path of the hailstone whose initial position is closest to the center of the main updraft. After 2 min, the hailstone is just entering updraft >20 m s^{-1} with a diameter of 0.8 cm and at a height of 6 km (Figs. 32 and 33). As shown in Fig. 33, the growth rate increases steadily for the first 4 minutes as the hailstone encounters the adiabatic water content and begins to decline thereafter. The decrease in the growth rate is explained by the corresponding decline in the amount of liquid water available as the environmental temperature drops below -15°C. After 4 min of growth, the hailstone has reached the center of the updraft and continues to rise rapidly in it even though the hailstone diameter is now 1.8 cm. After 5 min the hailstone has risen to 8 km where the environmental temperature is colder than -25°C and all growth has stopped due to the lack of liquid water.

---

[4] All three-dimensional graphics in this dissertation were produced by programs written by Vincent Wood of NSSL.

Figure 31. Three-dimensional perspective view of hailstone trajectories. Initial locations are marked by closed circles in the 7 km level of Fig. 30 (D_o=6 mm). Open circles show the hailstone positions at 2 min. intervals. Note these circles appear larger or smaller as the trajectory moves towards or away from the observer. Crosses show where the trajectories cross the indicated planes. The vertical scale has been expanded by a factor of two. The observer is looking towards the NNW (343°). Growth parameters of these hailstones are shown in Fig. 33.

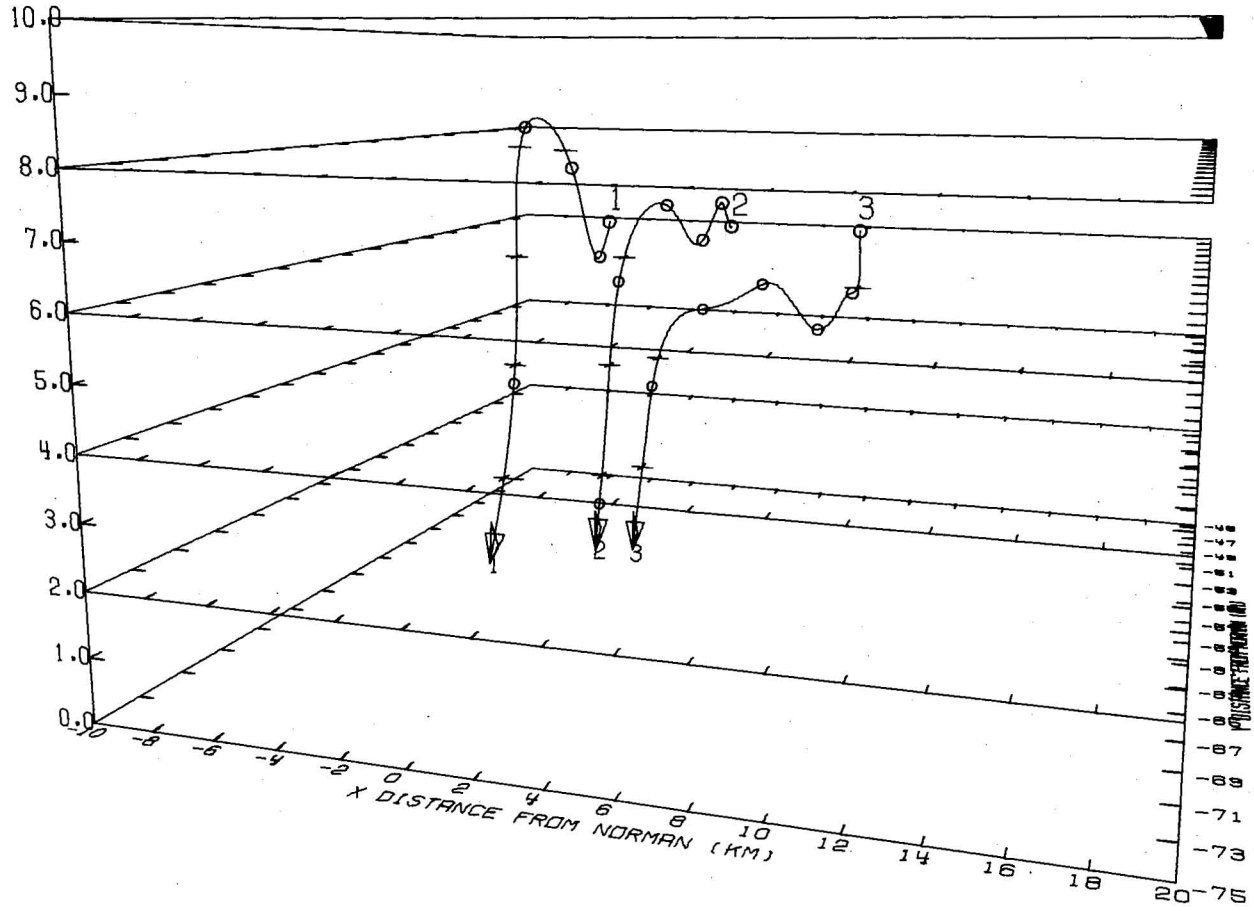

In contrast to the trajectory described above, the growth history of hailstone 3 is limited by opposite factors, as shown in Figs. 31, 32, and 33. It encounters the liquid water rich updraft following about 4 minutes of growth, but at this time it has descended to 5 km where the environmental temperature (~-2°C) is too warm to allow much of the accreted water to freeze.

Several factors favorably affect the growth of hailstone 2 (Figs. 31, 32, 33). From 0 to 3 min it is carried aloft and experiences some growth in core D. By the time it reaches the main updraft, it is still above 6 km and is 1.8 cm in diameter. The residence time of this hailstone in the main updraft (4-7 min) is at a fairly constant height and in a temperature regime (-10 to -20°C) that favors growth. This results because it is growing rapidly enough that its higher terminal velocity somewhat counteracts the progressively stronger updrafts it experiences. This balance is extremely important and without it the hailstone will not grow to a large size. In addition, the liquid water it encounters is sufficient to cause wet growth over a long time period and, thus, it is able to grow by collecting ice as well.

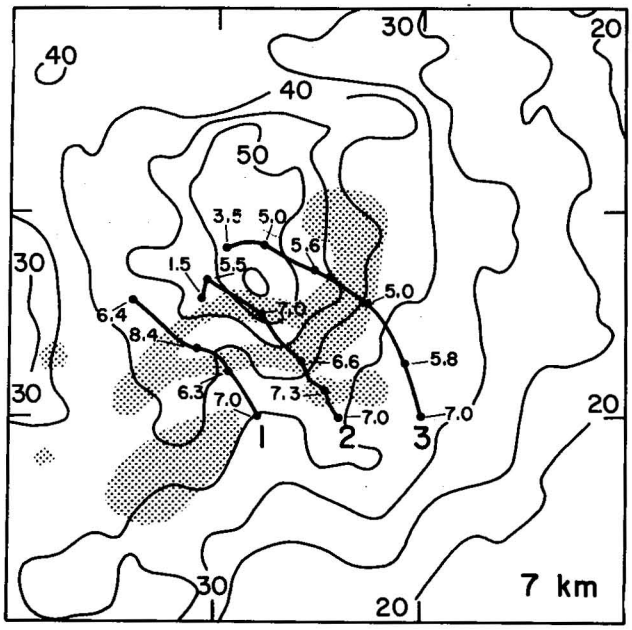

Figure 32. Plan view of three hail trajectories shown in Fig. 31. Heights of the hailstones are shown at two minute intervals along the trajectories. For reference the 7 km reflectivity and vertical velocity fields are superimposed (see Fig. 26). Tick marks are at 10 km intervals.

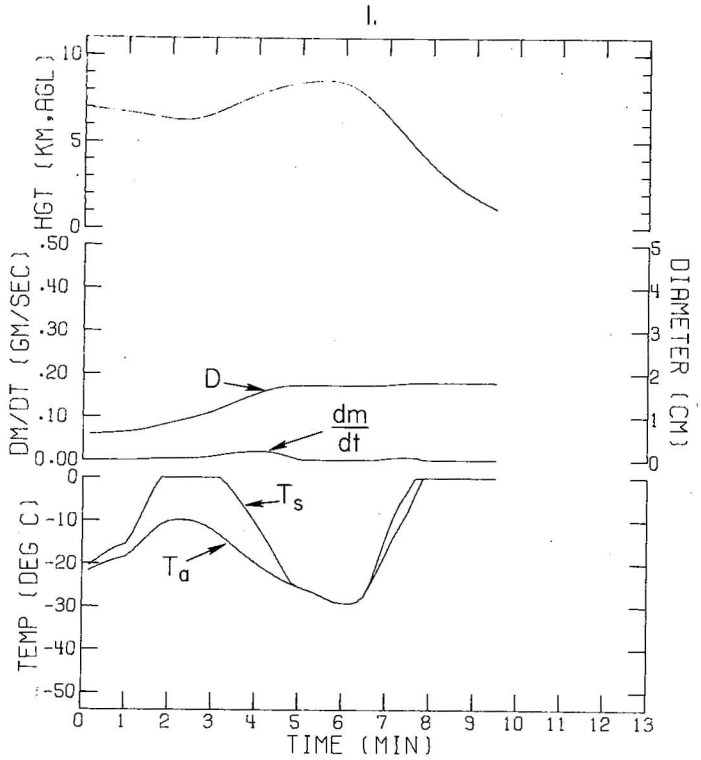

Figure 33. Time history of hailstone height and growth parameters. D - diameter (cm); dm/dt - mass time rate of change (g s^{-1}); T_s,T_a - temperature of hailstone surface and growth environment (°C). The T_a curve terminates when the hailstone falls below the 0°C level. (1), (2), and (3) are for hailstone trajectories 1, 2, and 3 shown in Figs. 31 and 32. (Continued on next page.)

Figures 34- 37 give the trajectory, growth parameters, and model output of a hailstone from the giant hail area (GHA) described in 5.3. The initial location of this stone is shown at 8 km of Fig. 30 (D_0 = 6 mm). In this location, the horizontal flow is fairly weak and the hailstone remains in a small region on the eastern edge of the updraft for 6 min (Fig. 35). During this time it grows at a moderate rate to over 2 cm in diameter. It then rises above 7.5 km and is caught in flow that carries it across the updraft where its maximum growth occurs (6-10 min). Because the hailstone is quite large it grows in the wet mode even though the environmental temperature is less than -15°C (Fig. 37), and collects almost as much ice as supercooled liquid water. In fact, because no latent heat is associated with the collection of ice crystals, the hailstone grows larger than it would have had all the water mass been liquid. That is, for a given set of environmental conditions there is a maximum amount of liquid water that can be frozen due to the hailstone's heat budget. If all the cloud water per unit volume that cannot be frozen is converted to ice, before collection then all water mass, whether liquid or solid, will be collected. This is true as long as there is enough liquid water to allow the hailstone to grow in a wet mode. A major role of ice collection in hail production has not been established, but laboratory experiments indicate that it can not be dismissed (Ashworth and Knight, 1978). An important part of the growth of the giant hailstone discussed above and a few other hailstones from the model may be attributed to the collection of ice crystals. For glaciation modification efforts, this implies a possible hail growth enhancement if insufficient liquid water is frozen to prevent wet growth. It should be noted this argument ignores any dynamical effects on the storm when the latent heat is released as this excess liquid water freezes.

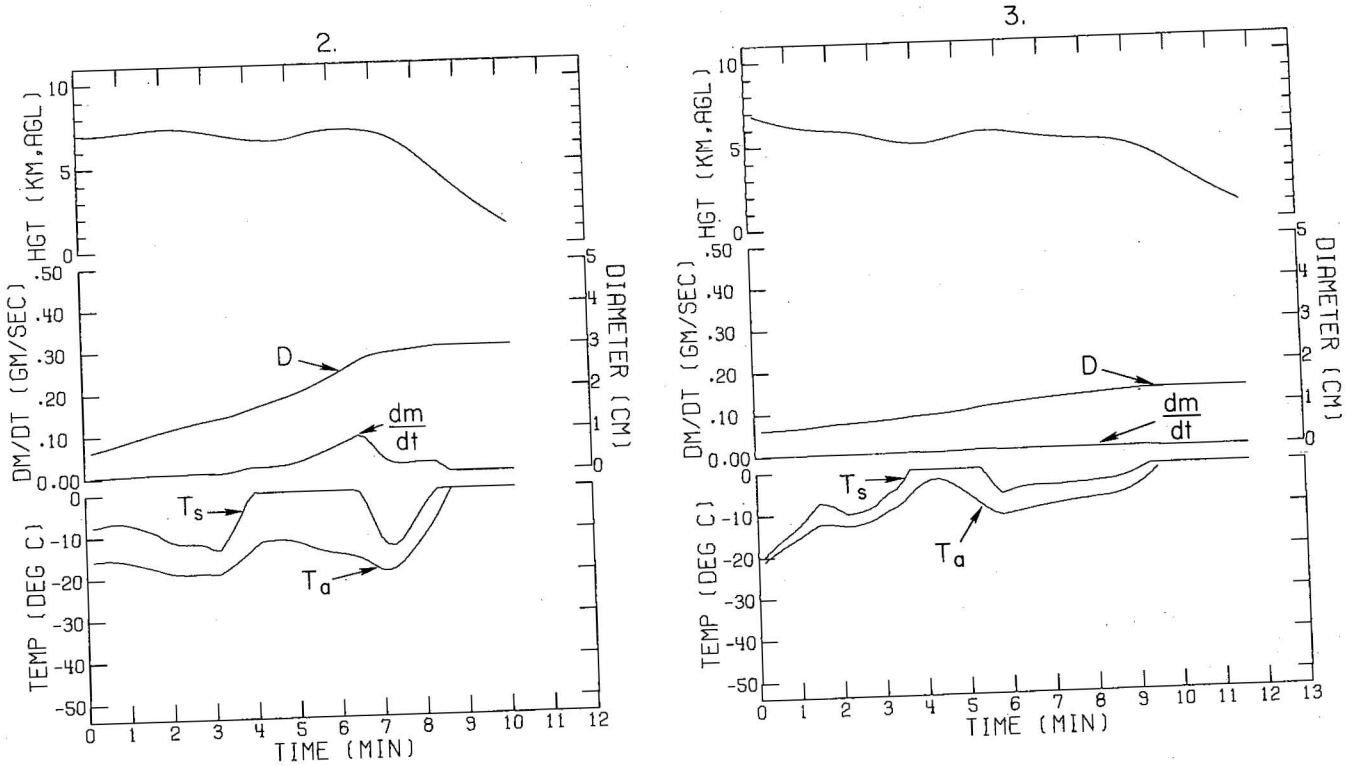

(Figure 33 Continued)

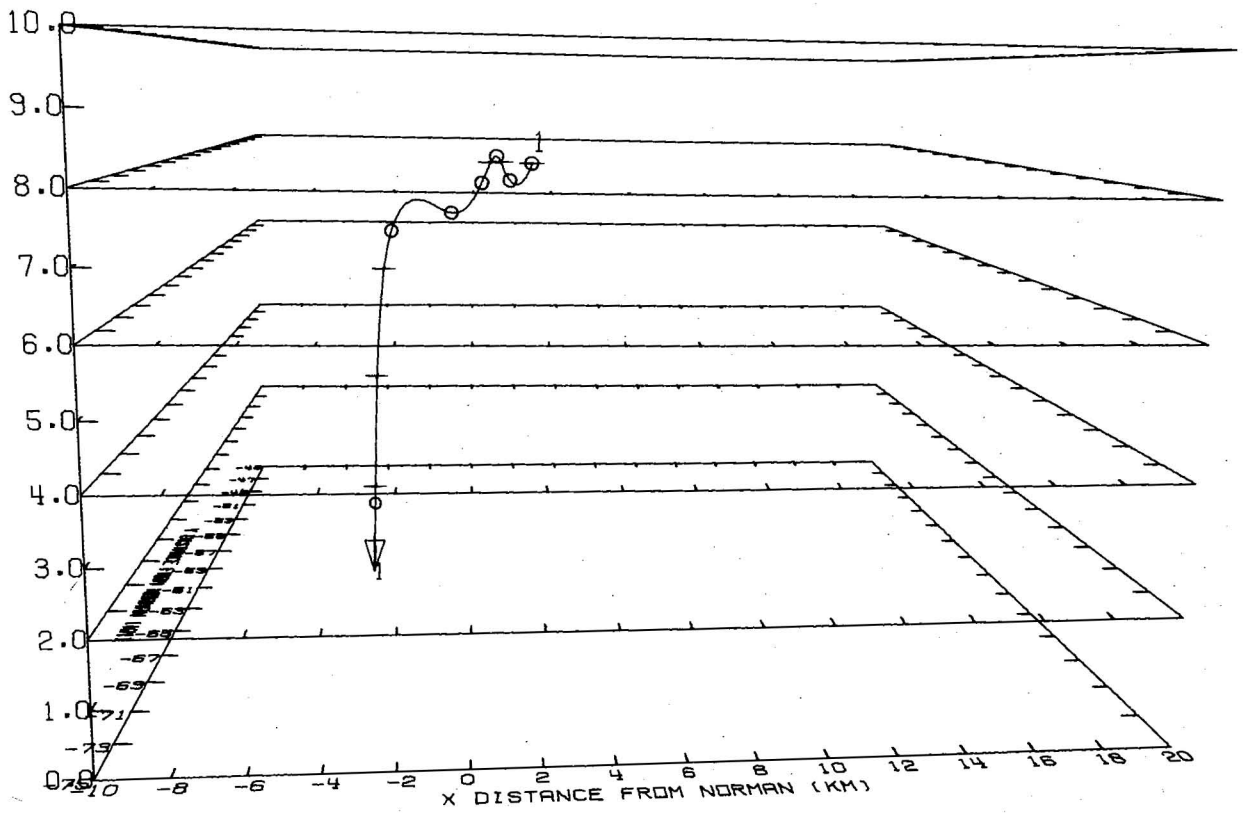

Figure 34. Three-dimensional trajectory of a hailstone in the giant hail area. Starting location is shown by the closed circle on the 8 km section of Fig. 30 (D_o=6 mm). Growth parameters are shown in Fig. 36. The observer is looking towards the north (6°). See Fig. 31 for further explanation.

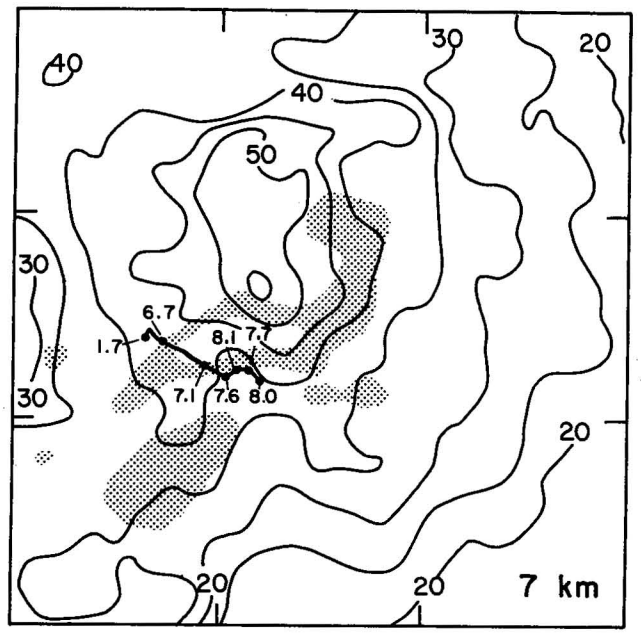

Figure 35. Plan view of hail trajectory shown in Fig. 34. See Fig. 32 for further explanation.

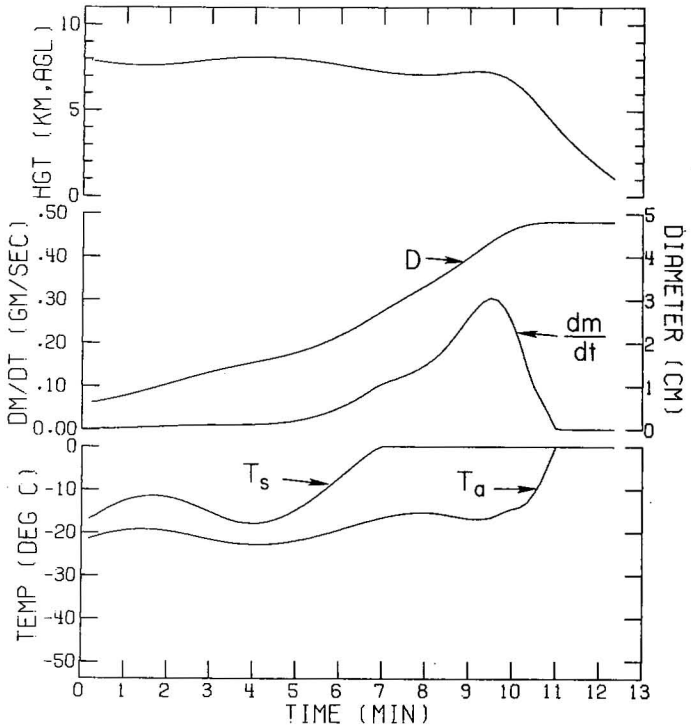

Figure 36. Time history of height and growth parameters of hailstone shown in Fig. 34 and 35. See Fig. 33 for further explanation.

5.5 Possible Embryo Sources

The model indicates two regions through which large hail embryos could pass--the GHA and embryo corridor. The GHA does not produce a large enough hail area at the surface to account for swath widths typically observed in these storms. Consequently, it is logical to assume that the embryos of some significant hail (>1.0 cm) reaching the surface must at some time pass through the embryo corridor.

Figures 38 and 39 are vertical sections of the wind and hail data shown in Figs. 26 and 30, respectively. Both are constructed along the line shown in the 8 km section of Fig. 30 (D_0 = 6 mm). This vertical plane was chosen because it intersects the GHA, embryo corridor, and updraft cores B and D. In addition, above 5 km the flow perpendicular to this section is small; therefore, hydrometeors in this plane tend to remain there.

One mechanism by which embryos find their way into the embryo corridor is by transport from above. Figure 38 indicates a flow structure whereby small hydrometeors could grow as they are carried aloft and then advected to the east or southeast in the outflow and into the critical regions. Once the particles are carried to very cold temperatures and away from the updraft, most growth would stop. Significant growth would not begin again until the hydrometeors re-enter the updraft through sedimentation and advection. This hypothesis provides the often observed discontinuity in growth characteristics between embryos and hail (Knight and Knight, 1970). In general, this injection mechanism agrees with those proposed by several authors (e.g., Browning, 1963; Nelson and Braham, 1975; Browning and Foote, 1976; and Bensch, 1976). There is, however, a significant difference from the Browning and Foote model described in 1.2.2. They postulate that embryos form in a small region near the stagnation point between environmental flow and storm updraft. This model suggests the particles which become embryos

PARTICLE NUMBER 2

TIME (SEC)	DIAM (CM)	MASS (GM)	LOCATION(KM) X	Y	Z	GROWTH MODE	XMUW	F-FROZ	TEMP-A (DEG C)	TEMP-S (DEG C)	RW (GM/CM**3)	RI (GM/CM**3)	AWM (GM)	AIM (GM)	TAWM (GM)	TAIM (GM)
0	0.60	0.102	12.000	12.000	8.000		0.000	1.00	999.99	-27.00	0.9990E 02	0.9990E 02	0.0000	0.0000	0.000	0.000
10	0.61	0.109	11.951	12.026	7.912	DRY	0.000	1.00	-21.45	-16.92	0.1545E-05	0.4985E-05	0.0073	0.0000	0.007	0.000
20	0.64	0.124	11.898	12.063	7.842	DRY	0.000	1.00	-20.93	-16.07	0.1771E-05	0.4758E-05	0.0082	0.0071	0.015	0.007
30	0.67	0.143	11.841	12.108	7.779	DRY	0.000	1.00	-20.46	-15.02	0.1974E-05	0.4554E-05	0.0102	0.0084	0.026	0.016
40	0.71	0.165	11.781	12.161	7.725	DRY	0.000	1.00	-20.06	-14.09	0.2148E-05	0.4378E-05	0.0124	0.0101	0.038	0.026
50	0.74	0.192	11.718	12.218	7.680	DRY	0.000	1.00	-19.74	-13.29	0.2290E-05	0.4234E-05	0.0149	0.0120	0.053	0.038
60	0.78	0.224	11.653	12.279	7.647	DRY	0.000	1.00	-19.49	-12.62	0.2397E-05	0.4125E-05	0.0176	0.0142	0.070	0.052
70	0.82	0.261	11.587	12.342	7.625	DRY	0.000	1.00	-19.32	-12.10	0.2469E-05	0.4053E-05	0.0206	0.0167	0.091	0.068
80	0.86	0.305	11.521	12.403	7.614	DRY	0.000	1.00	-19.24	-11.74	0.2504E-05	0.4017E-05	0.0237	0.0196	0.115	0.088
90	0.91	0.354	11.456	12.463	7.614	DRY	0.000	1.00	-19.24	-11.52	0.2504E-05	0.4018E-05	0.0269	0.0229	0.142	0.111
100	0.96	0.411	11.392	12.517	7.625	DRY	0.000	1.00	-19.32	-11.46	0.2469E-05	0.4053E-05	0.0301	0.0266	0.172	0.138
110	1.00	0.475	11.330	12.566	7.645	DRY	0.000	1.00	-19.48	-11.57	0.2402E-05	0.4120E-05	0.0331	0.0308	0.205	0.168
120	1.05	0.546	11.271	12.608	7.675	DRY	0.000	1.00	-19.69	-11.79	0.2308E-05	0.4216E-05	0.0359	0.0353	0.241	0.204
130	1.10	0.624	11.215	12.641	7.712	DRY	0.000	1.00	-19.97	-12.16	0.2190E-05	0.4335E-05	0.0384	0.0401	0.279	0.244
140	1.15	0.710	11.163	12.665	7.754	DRY	0.000	1.00	-20.28	-12.65	0.2054E-05	0.4473E-05	0.0403	0.0451	0.319	0.289
150	1.19	0.802	11.115	12.680	7.800	DRY	0.000	1.00	-20.62	-13.23	0.1905E-05	0.4623E-05	0.0417	0.0500	0.361	0.339
160	1.24	0.899	11.072	12.686	7.849	DRY	0.000	1.00	-20.98	-13.88	0.1749E-05	0.4780E-05	0.0425	0.0546	0.403	0.393
170	1.29	1.000	11.032	12.682	7.898	DRY	0.000	1.00	-21.34	-14.59	0.1592E-05	0.4938E-05	0.0426	0.0588	0.446	0.452
180	1.33	1.105	10.995	12.670	7.945	DRY	0.000	1.00	-21.69	-15.31	0.1441E-05	0.5090E-05	0.0423	0.0622	0.488	0.514
190	1.37	1.211	10.962	12.650	7.988	DRY	0.000	1.00	-22.01	-16.01	0.1300E-05	0.5230E-05	0.0415	0.0648	0.530	0.579
200	1.41	1.317	10.931	12.624	8.026	DRY	0.000	1.00	-22.31	-16.71	0.1165E-05	0.5331E-05	0.0403	0.0663	0.570	0.645
210	1.45	1.424	10.899	12.596	8.056	DRY	0.000	1.00	-22.55	-17.26	0.1060E-05	0.5431E-05	0.0395	0.0671	0.610	0.713
220	1.48	1.531	10.868	12.567	8.078	DRY	0.000	1.00	-22.73	-17.68	0.9836E-06	0.5503E-05	0.0391	0.0678	0.649	0.780
230	1.52	1.639	10.836	12.538	8.092	DRY	0.000	1.00	-22.84	-17.91	0.9350E-06	0.5549E-05	0.0396	0.0688	0.688	0.849
240	1.55	1.751	10.804	12.508	8.098	DRY	0.000	1.00	-22.89	-17.98	0.9135E-06	0.5569E-05	0.0410	0.0708	0.729	0.920
250	1.58	1.869	10.771	12.478	8.097	DRY	0.000	1.00	-22.88	-17.85	0.9184E-06	0.5565E-05	0.0435	0.0740	0.773	0.994
260	1.62	1.995	10.738	12.449	8.088	DRY	0.000	1.00	-22.80	-17.57	0.9492E-06	0.5535E-05	0.0475	0.0791	0.820	1.073
270	1.65	2.134	10.703	12.421	8.072	DRY	0.000	1.00	-22.68	-17.12	0.1005E-05	0.5482E-05	0.0531	0.0860	0.873	1.159
280	1.69	2.290	10.667	12.393	8.049	DRY	0.000	1.00	-22.49	-16.49	0.1086E-05	0.5404E-05	0.0606	0.0951	0.934	1.254
290	1.74	2.467	10.630	12.367	8.019	DRY	0.000	1.00	-22.25	-15.70	0.1191E-05	0.5306E-05	0.0704	0.1067	1.004	1.361
300	1.78	2.672	10.592	12.342	7.982	DRY	0.000	1.00	-21.97	-14.77	0.1321E-05	0.5210E-05	0.0829	0.1217	1.087	1.483
310	1.83	2.908	10.552	12.320	7.939	DRY	0.000	1.00	-21.65	-13.78	0.1459E-05	0.5071E-05	0.0975	0.1386	1.185	1.621
320	1.89	3.181	10.509	12.304	7.889	DRY	0.000	1.00	-21.28	-12.65	0.1620E-05	0.4909E-05	0.1159	0.1576	1.301	1.779
330	1.95	3.500	10.463	12.293	7.833	DRY	0.000	1.00	-20.86	-11.42	0.1800E-05	0.4728E-05	0.1385	0.1796	1.439	1.958
340	2.02	3.870	10.414	12.288	7.772	DRY	0.000	1.00	-20.41	-10.10	0.1997E-05	0.4531E-05	0.1658	0.2044	1.605	2.163
350	2.09	4.300	10.361	12.289	7.707	DRY	0.000	1.00	-19.93	-8.73	0.2205E-05	0.4320E-05	0.1985	0.2318	1.804	2.395
360	2.17	4.799	10.305	12.297	7.639	DRY	0.000	1.00	-19.43	-7.33	0.2422E-05	0.4101E-05	0.2373	0.2614	2.041	2.656
370	2.25	5.374	10.245	12.311	7.570	DRY	0.000	1.00	-18.92	-5.93	0.2643E-05	0.3877E-05	0.2827	0.2930	2.324	2.949
380	2.34	6.036	10.181	12.331	7.501	DRY	0.000	1.00	-18.41	-4.53	0.2863E-05	0.3653E-05	0.3353	0.3264	2.659	3.275
390	2.43	6.793	10.113	12.356	7.434	DRY	0.000	1.00	-17.91	-3.20	0.3078E-05	0.3433E-05	0.3957	0.3615	3.055	3.637
400	2.53	7.655	10.042	12.385	7.369	DRY	0.000	1.00	-17.43	-1.92	0.3283E-05	0.3224E-05	0.4642	0.3976	3.519	4.034
410	2.64	8.631	9.968	12.417	7.309	DRY	0.000	1.00	-16.99	-0.72	0.3474E-05	0.3028E-05	0.5408	0.4352	4.060	4.470
420	2.74	9.687	9.888	12.454	7.253	WET	0.044	0.93	-16.58	0.00	0.3649E-05	0.2848E-05	0.6260	0.4744	4.641	4.944
430	2.84	10.813	9.802	12.495	7.204	WET	0.142	0.86	-16.21	0.00	0.3806E-05	0.2686E-05	0.7168	0.5059	5.261	5.450
440	2.94	11.995	9.710	12.541	7.161	WET	0.296	0.81	-15.89	0.00	0.3939E-05	0.2548E-05	0.8111	0.5247	5.918	5.975
450	3.04	13.237	9.610	12.591	7.128	WET	0.505	0.77	-15.65	0.00	0.4043E-05	0.2441E-05	0.9058	0.5468	6.614	6.522
460	3.14	14.550	9.502	12.643	7.105	WET	0.767	0.74	-15.48	0.00	0.4114E-05	0.2367E-05	0.9990	0.5748	7.352	7.096
470	3.23	15.944	9.387	12.697	7.094	WET	1.073	0.72	-15.40	0.00	0.4149E-05	0.2331E-05	1.0887	0.6118	8.134	7.708
480	3.33	17.437	9.263	12.752	7.096	WET	1.415	0.71	-15.41	0.00	0.4145E-05	0.2336E-05	1.1731	0.6612	8.966	8.369
490	3.43	19.050	9.130	12.807	7.110	WET	1.778	0.71	-15.51	0.00	0.4101E-05	0.2381E-05	1.2507	0.7263	9.853	9.096
500	3.53	20.811	8.988	12.863	7.136	WET	2.148	0.72	-15.71	0.00	0.4017E-05	0.2468E-05	1.3198	0.8109	10.803	9.906
510	3.64	22.750	8.835	12.920	7.175	WET	2.507	0.74	-15.99	0.00	0.3896E-05	0.2592E-05	1.3799	0.9181	11.824	10.825
520	3.75	24.889	8.673	12.983	7.216	WET	2.849	0.76	-16.30	0.00	0.3767E-05	0.2724E-05	1.4397	1.0417	12.921	11.866
530	3.87	27.254	8.502	13.053	7.259	WET	3.166	0.79	-16.62	0.00	0.3631E-05	0.2866E-05	1.4988	1.1827	14.103	13.049
540	3.99	29.845	8.320	13.134	7.289	WET	3.475	0.80	-16.84	0.00	0.3536E-05	0.2964E-05	1.5774	1.3223	15.372	14.371
550	4.11	32.642	8.126	13.225	7.299	WET	3.811	0.80	-16.91	0.00	0.3506E-05	0.2995E-05	1.6895	1.4432	16.725	15.815
560	4.23	35.605	7.920	13.329	7.283	WET	4.214	0.78	-16.82	0.00	0.3535E-05	0.2946E-05	1.8365	1.5308	18.158	17.345
570	4.35	38.656	7.708	13.446	7.228	WET	4.735	0.74	-16.53	0.00	0.3615E-05	0.2785E-05	2.0172	1.5540	19.655	18.899
580	4.45	41.654	7.502	13.575	7.117	WET	5.455	0.68	-15.92	0.00	0.3778E-05	0.2463E-05	2.2512	1.4673	21.186	20.367
590	4.55	44.454	7.307	13.717	6.945	WET	6.397	0.62	-15.12	0.00	0.3911E-05	0.2025E-05	2.4649	1.2764	22.709	21.643
600	4.64	46.937	7.129	13.868	6.708	WET	7.328	0.57	-14.49	0.00	0.3936E-05	0.1554E-05	2.3919	1.0222	24.170	22.665
610	4.70	48.971	6.972	14.026	6.390	WET	7.871	0.71	-14.10	0.00	0.2761E-05	0.1032E-05	1.8726	0.7048	25.499	23.370
620	4.75	50.425	6.839	14.184	5.999	WET	8.007	0.89	-13.09	0.00	0.1835E-05	0.4760E-06	1.2624	0.3275	26.625	23.698
630	4.78	51.417	6.738	14.314	5.547	WET	8.161	0.86	-10.93	0.00	0.1561E-05	0.1028E-06	1.0743	0.0708	27.546	23.768
640	4.80	52.105	6.660	14.394	5.065	WET	8.293	0.84	-8.27	0.00	0.1204E-05	0.0000E 00	0.8213	0.0000	28.235	23.768
650	4.81	52.477	6.602	14.422	4.569	WET	8.628	0.53	-4.32	0.00	0.1051E-05	0.0000E 00	0.7061	0.0000	28.607	23.768
660	4.81	52.502	6.561	14.390	4.083	WET	9.213	0.04	-0.29	0.00	0.9247E-06	0.0000E 00	0.6109	0.0000	28.632	23.768
670	4.81	52.502	6.536	14.299	3.617	MLT	9.723	0.00	3.54	0.00	0.7888E-06	0.0000E 00	0.5098	0.0000	28.632	23.768
680	4.81	52.502	6.523	14.166	3.182	MLT	10.136	0.00	7.11	0.00	0.6517E-06	0.0000E 00	0.4130	0.0000	28.632	23.768
690	4.81	52.502	6.517	13.997	2.778	MLT	10.455	0.00	10.27	0.00	0.5133E-06	0.0000E 00	0.3190	0.0000	28.632	23.768
700	4.81	52.502	6.517	13.808	2.401	MLT	10.684	0.00	13.09	0.00	0.3749E-06	0.0000E 00	0.2288	0.0000	28.632	23.768
710	4.81	52.502	6.519	13.612	2.046	MLT	10.824	0.00	15.75	0.00	0.2345E-06	0.0000E 00	0.1407	0.0000	28.632	23.768
720	4.81	52.502	6.521	13.410	1.706	MLT	10.917	0.00	16.66	0.00	0.1570E-06	0.0000E 00	0.0927	0.0000	28.632	23.768
730	4.81	52.502	6.523	13.212	1.378	MLT	10.968	0.00	17.28	0.00	0.8713E-07	0.0000E 00	0.0505	0.0000	28.632	23.768
740	4.81	52.502	6.523	13.019	1.060	MLT	10.976	0.00	17.89	0.00	0.1423E-07	0.0000E 00	0.0081	0.0000	28.632	23.768

Figure 37. Hail growth model output for hailstone in Figs. 34 and 35. See Fig. 22 for further explanation.

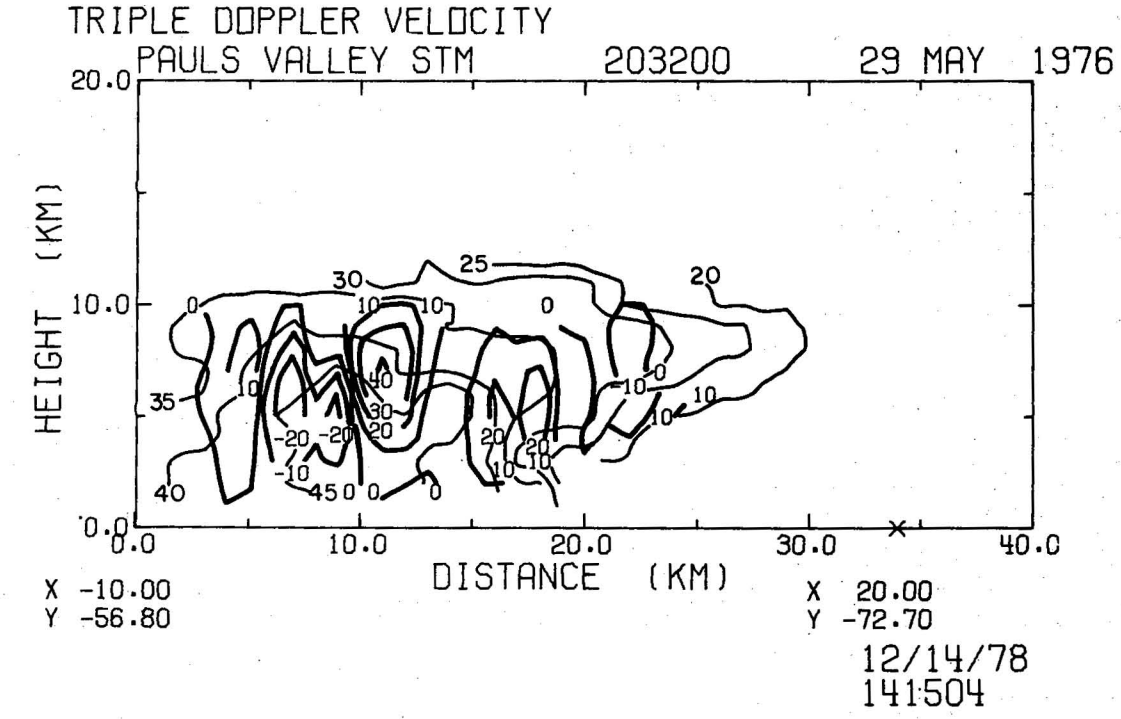

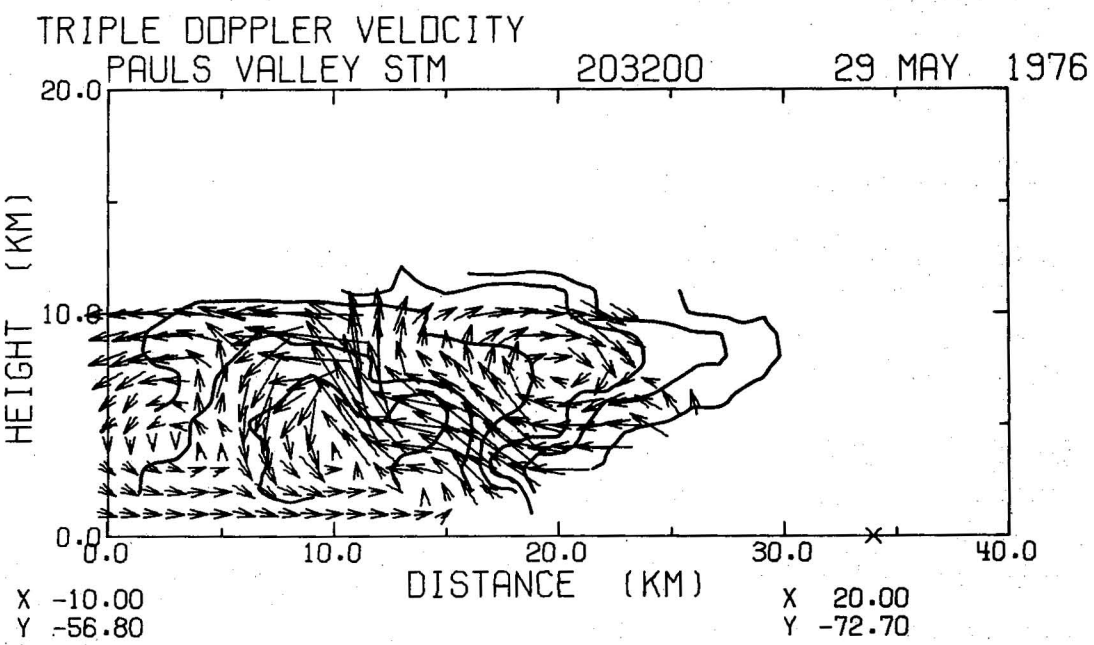

Figure 38. Vertical section of reflectivity and vertical velocity (top, m s^{-1}) and reflectivity and wind vectors (bottom). This vertical section is shown on the 8 km horizontal plane in Fig. 30. For the wind vectors a 1 km length represents 10 m s^{-1} in speed. The reflectivity field is contoured at 5 dBZ intervals and labeled in the top section only.

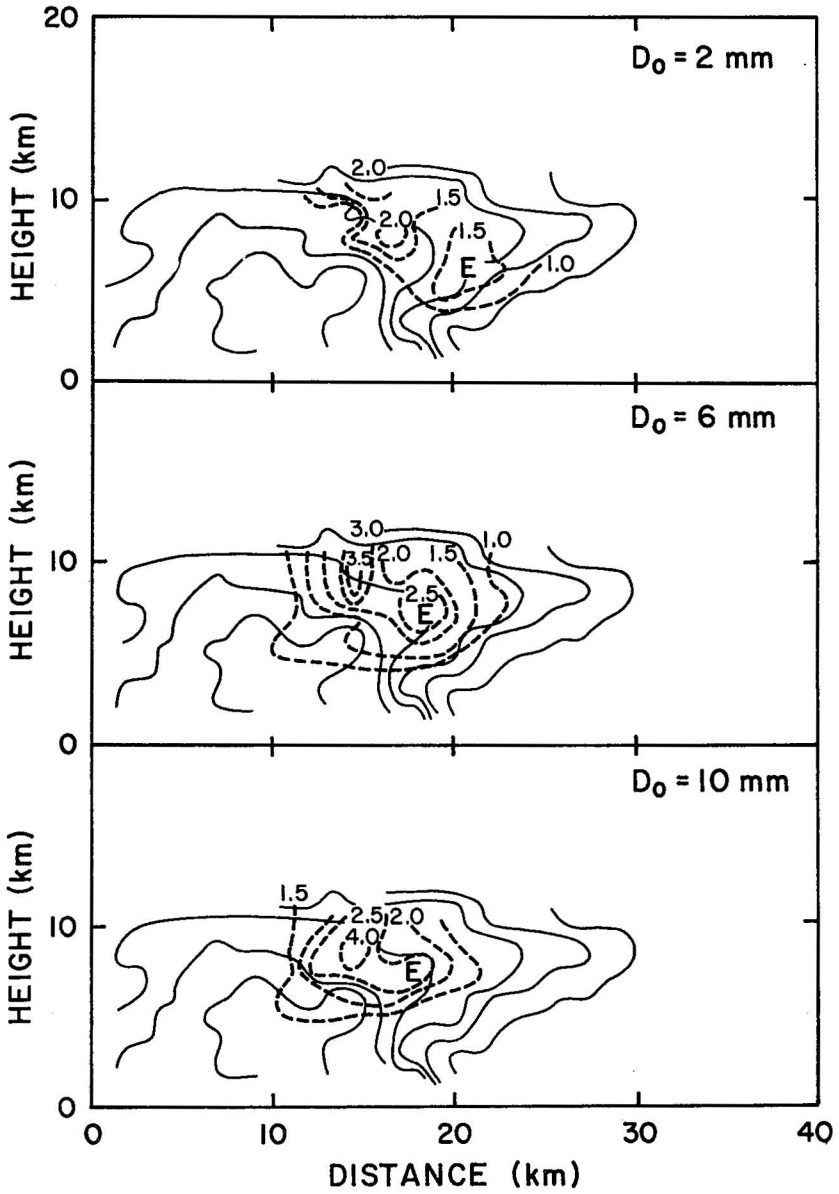

Figure 39. Vertical sections of data shown in Fig. 30. Dashed lines are final hail sizes in cm; light lines are reflectivity contoured every 5 dBZ. These sections are the same as in Fig. 38. The "E" marks the embryo corridor.

could form over a much larger volume in the upper level outflow/overhang because a wide range of hydrometeor growth rates (hence V_t) and storm flow can produce correctly sized embryos in locations critical to the production of large hail.

Another similar mechanism for embryo injection is the transfer of hydrometeors from the flanking line cells to the dominant core. Figures 40 and 41 show an example of this process. The particle (D_0 = 2 mm) begins at the 10 km level in the outflow of updraft core A. From here it falls and drifts to the northeast until it is caught in core D. By the time it exits core D, it has grown to about 4-5 mm in diameter. Further growth is similar to trajectory 1 of Fig. 31. This particular particle has a long growth time (>30 min); therefore, its growth history may not be valid since this violates the stationarity assumption of the wind field.

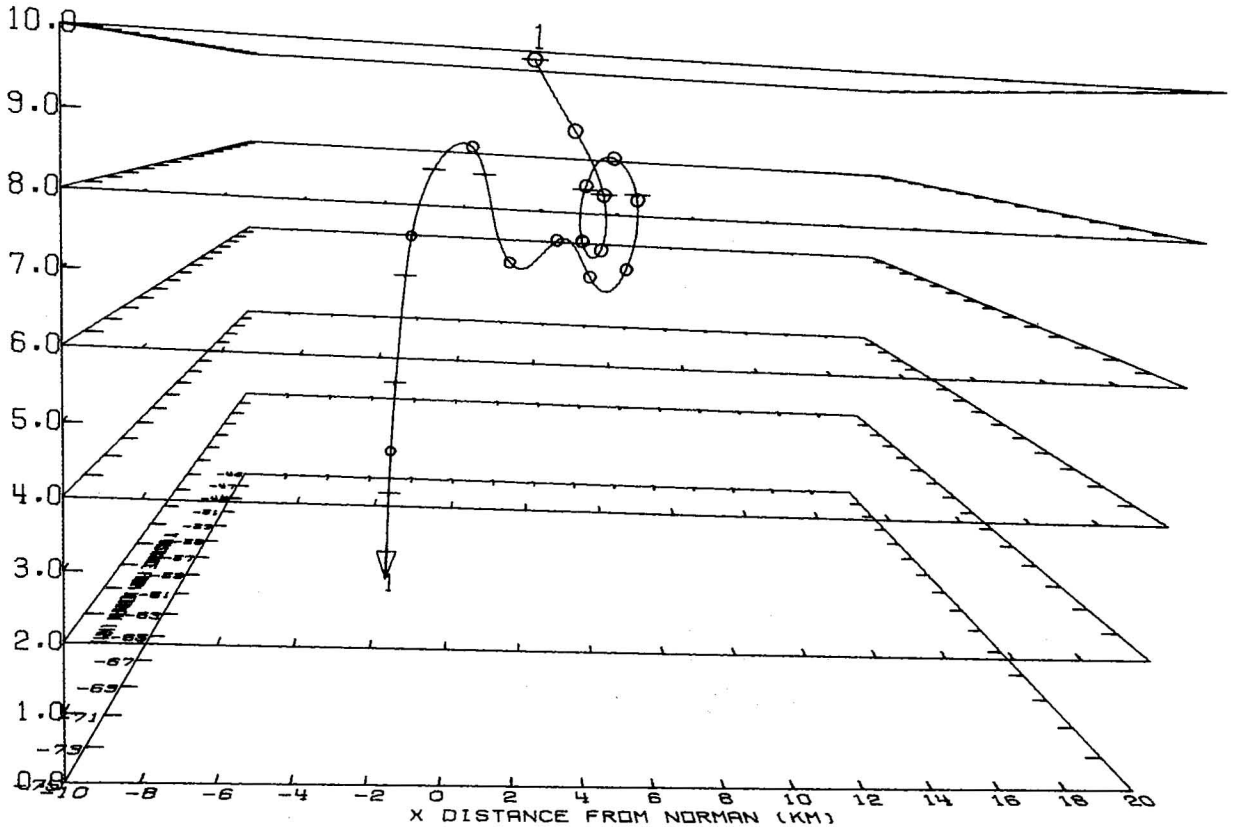

Figure 40. Three-dimensional trajectory of embryo that originates in outflow of core A. Growth parameters are given in Fig. 41. The observer is looking towards the north (6°). See Fig. 31 for further explanation.

In a multicellular Colorado hailstorm, Heymsfield et al. (1980) found embryo transfer between cells, rather than from the upper level outflow, to be the more important embryo source. Their storm possessed a much smaller outflow than the supercell storm presented here. The very large outflow in this case appears to be as likely an embryo source as the feeder clouds. The upper level outflow is also more likely to provide a continuous supply of embryos in agreement with the continuous hail production characteristics of supercell storms.

Both the upper level outflow and cell transfer embryo injection hypotheses imply the embryos are mainly graupel. This is at odds with the findings of Knight and Knight (1978) that the majority of embryos in Oklahoma are frozen drops. Their data is not stratified as to storm structure, but the case for mostly frozen drop embryos in Oklahoma is quite strong. Figure 38 suggests two ways that frozen drop embryos might be formed. The first is that graupel embryos from the outflow might sink below the melting level (4-5 km) before being carried aloft again. Another possibility is that a few giant particles might be grown in the relatively weak updrafts of core D and then carried aloft to freeze. Indeed, it is possible that both graupel and frozen drop embryos are produced and then carried to the common growth area. This scenario is in agreement with the embryo studies of Rosinski et al. (1979).

The GHA is an interesting phenomenon. Its existence depends on an ideal balance between the initial embryo size, hailstone growth rate, and three-dimensional wind field. The key growth characteristic is the collection of substantial ice mass in a mixed phase growth region. While it is not unreasonable to believe such a region could exist, its lifetime and location would probably be transient.

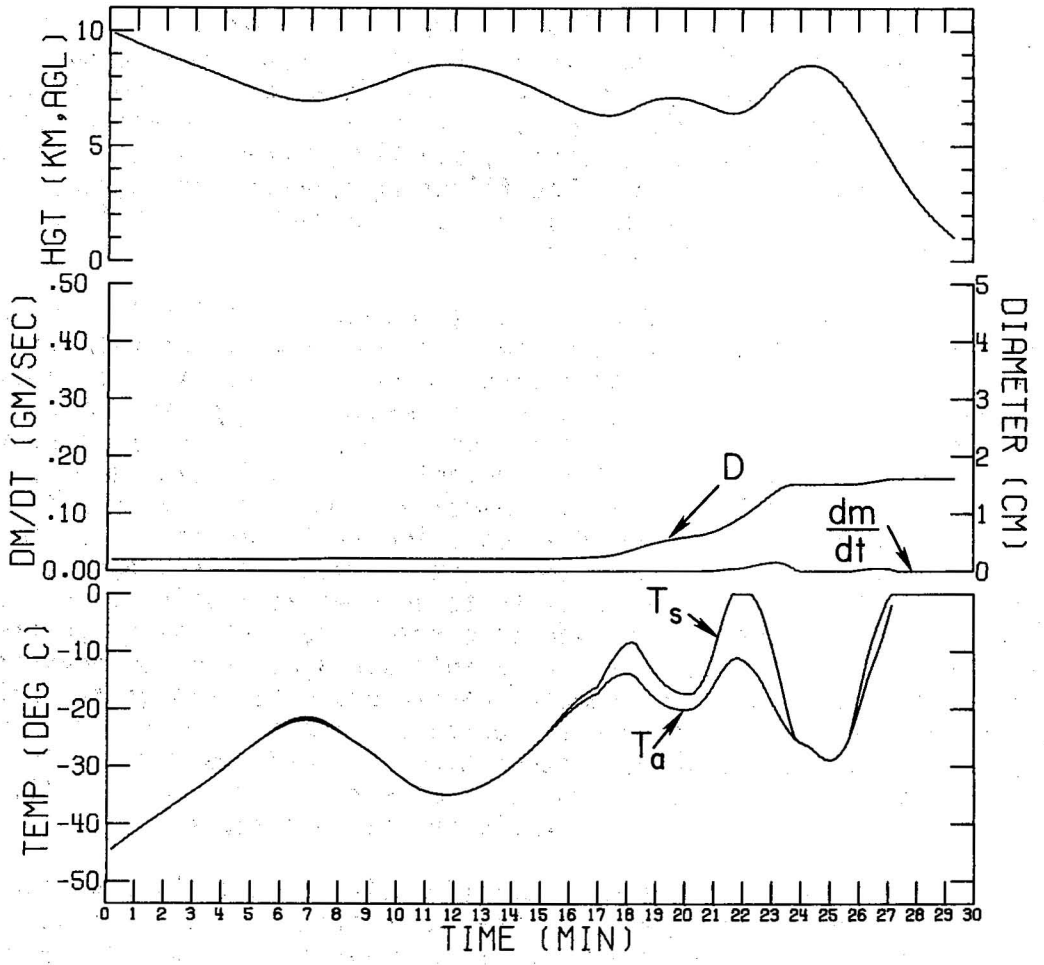

Figure 41. Time history of height and growth parameters of hailstone shown in Fig. 40. See Fig. 33 for further explanation.

There is also the question of where the proper sized embryos originate. It is difficult to demonstrate the GHA's existence on indirect evidence and indeed it may be strictly an artifact of this model. The point most in its favor is that it produces hail fairly close to the maximum size observed at the surface. The GHA and ice mass collection certainly warrant further study.

6. SUMMARY AND DISCUSSION

Hail production in a supercell-type storm is studied in depth using a numerical hail growth model, environmental sounding data, and wind fields from a triple Doppler synthesis. The study concentrates on identifying embryo source regions and analyzing the interaction between the growing hailstone and the storm's thermal, moisture and wind fields.

6.1 Doppler Analysis Techniques

Triple Doppler data available for this storm are of rather poor quality. The angle between the three radar beams is far from optimum and data is missing from the lowest and highest storm levels. This is of little consequence for obtaining the horizontal velocities, but is of prime importance in deriving the

vertical velocity (w). A detailed analysis is made of the errors associated with solving the continuity equation to obtain w. Possible errors due to numerical approximations dictate filtering the data in three dimensions to remove scales less than about four times the data spacing. Since the exact nature of the filtering properties of interpolating schemes is usually unknown, a separate three-dimensional filter should be applied. The filtering process, of course, places a limit on the smallest velocity scales that can be resolved successfully. For this particular case, this limit is about 4 km.

Further investigation showed that the direction of integration is important. The constraint of mass continuity causes small errors in vertical velocity to grow to large errors as they are integrated upward. When the direction of integration is downward, vertical velocity errors become increasingly less important. Errors in vertical velocity can come from several sources--noisy or incorrect radial velocities, incorrect boundary conditions, numerical approximation errors. The important point is that for like vertical velocity inaccuracies downward integration suppresses the errors while upward integration amplifies them. In some cases this amplification can completely mask the signal. Even though integration downward suppresses errors, they can still accumulate to unacceptable values. Following O'Brien (1970), a formulation was derived to correct the vertical velocities using the constraint that w goes to zero at the earth's surface. A major advantage of this adjustment is that it does not require continuous data through the entire storm depth, only that data exist near the earth's surface. In the area of echo overhangs no adjustment is possible. Integrating downward however, the number of integration steps and, hence, the accumulation of errors, should be small. Using upward integration, any solution at all would be most difficult.

The main problem with downward integration lies in establishing the top boundary condition. Four techniques have been described in 2.5.2 but others are certainly possible. Although there are definite advantages to using these solution techniques an exception occurs when the researcher is interested only in the lowest few kilometers. In such a case, integration upward is preferred since the boundary condition would be good and any accumulated errors would be minimal. If, however, w at middle and higher levels is desired, downward integration would provide more accurate results especially if the data are of low quality or incomplete.

6.2 Storm Structure

The storm's reflectivity and horizontal wind fields are very similar to other supercell storms reported previously in the literature. The lower levels exhibit a circulation about a vertical axis with its concomitant hook echo. In the midlevels, a weak echo region is present and aloft an extensive overhang is associated with strong divergence. The vertical draft structure, however, is fairly complex and differs in some respects from previous conceptual models. The classical updraft/downdraft couplet is present with maximum values of +51 m s^{-1} at 7 km and -25 m s^{-1} at 5 km, respectively. There are, however, other major updrafts. To the northeast of the dominant core is a relatively weak updraft with no well defined maximum. The role of this draft is not known. One possibility is that it is a remnant of a pulsation on the general updraft region. The other two updrafts (cores A and D), while smaller than the main updraft, are quite vigorous--+42 and +35 m s^{-1}, respectively. Both of these cells formed on a gust front that initially extended eastward and then turned southwestward from the primary circulation marked by the hook echo. It is assumed that these are what have been termed "flanking line cells."

Figure 42 shows a revised conceptual supercell storm model based on the results of this study. The reader may wish to contrast this with the Browning-Foote model shown in Fig. 3c. In regards to storm structure, two features are emphasized in the new model. First is the quite large extent of the dominant updraft at midlevels. Note that it extends much beyond the weak echo region. The second feature is the addition of a flanking line cell that has formed on the low level gust front. The importance of these features to hail growth is discussed below.

6.3 Hail Production

The question of how this storm produces large hail is addressed using a continuous collection growth model. The hail model's wind field is taken from the Doppler synthesis and is assumed to be stationary during the growth process. For

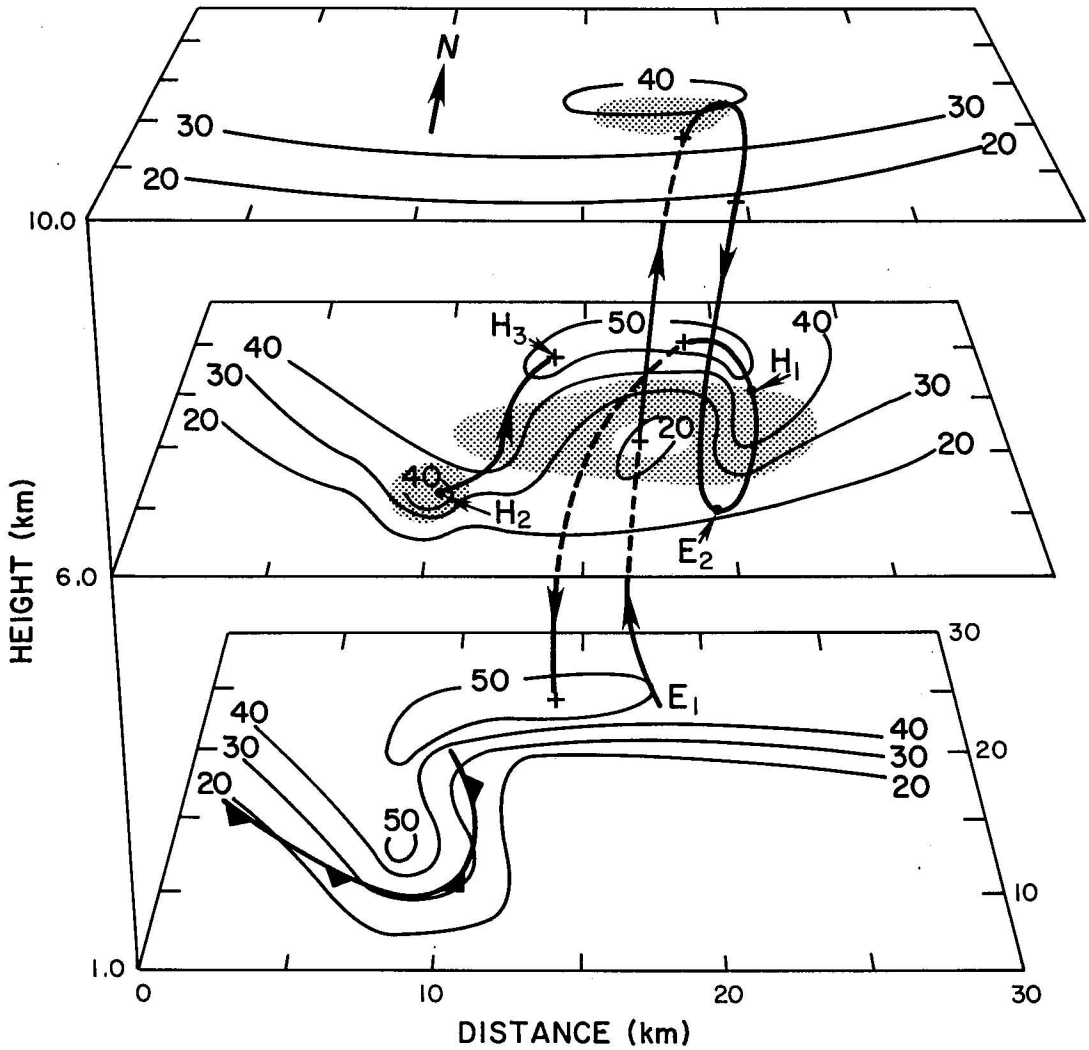

Figure 42. Revised conceptual supercell hailstorm model. Light lines are reflectivity (dBZ), shaded areas updraft ≥20 m s^{-1} with interior unshaded ≥40 m s^{-1}. Heavy lines show embryo and hailstorm trajectories. Solid line with barbs at the 1 km shows the gust front position. See text for further explanation.

most hailstones, this is probably valid since average growth times are typically less than 10 min. An attempt is made to simulate the three-dimensional variations of the thermal and moisture fields. This is accomplished based on an environmental sounding and the few in situ observations on updraft characteristics reported in the literature. Embryos of three different sizes (D_0 = 2, 6, and 10 mm) are distributed at 2 km intervals over a 22x22 km grid centered on the storm between 4 and 10 km. In actuality, embryos are probably not distributed uniformly across the storm. This approach does identify the area through which embryos must pass in order to produce large hail. This region, termed the embryo corridor, should not be emphasized since it has no real microphysical significance. That is, the embryo corridor denotes only one point in a continuous growth process. Knowing this location, however, allows speculation on embryo growth and sources. A likely mechanism is simply by particles advecting from above. Figure 42 shows hypothetical embryo and hail growth trajectories superimposed on the conceptual storm model. The embryo shown by $\overline{E_1E_2}$ grows in the updraft until it reaches the upper level outflow and is carried away from the updraft where most growth stops. From here the particle may either descend directly into the embryo corridor or perhaps fall below the freezing level, before being caught in the updraft and rising again.

The flanking line cells may also provide a source of embryos. For example, one model embryo in the upper level outflow of a flanking line cell did find its way into the embryo corridor (position E_2 on Fig. 42). Another particle (not previously shown) took a lower trajectory and grew to 2.2 cm in diameter along a trajectory similar to $\overline{H_2H_3}$ on Fig. 42. The transfer of embryos between cells is supported by Heymsfield et al. (1980) who found similar processes in a Colorado multicellular storm.

As described in Chapter 1, Browning and Foote suggest embryos of large hail begin their growth in a fairly small area near the stagnation point between environmental flow and the storm. In the present model, it is not possible to narrow the embryo source region to a particular area. To begin with, the embryo corridor area is fairly large. Embryos of the correct size can enter the corridor via an almost infinite number of growth rates in combination with the storm's flow structure. Add to this the possibility of embryos originating in flanking line cells, and the sources of embryos and their growth histories are likely quite varied. This view is supported by Rosinski et al. (1979) who reported that actual embryos from a given storm appeared to originate in different locales.

The embryos grow into hail by advecting into the main updraft. Significant growth does not begin until they encounter the cloud water rich updraft which may explain the observed growth discontinuity between the embryo and hailstone. A hailstone grows to its maximum size if it remains at a level where the temperatures are very cold, and there is a significant amount of liquid water. As the hailstone enters the updraft, it experiences two conflicting factors. Its newly added mass causes the particle to sink, while the increasingly stronger updraft has the opposite effect. The greatest growth in the updraft occurs where the gradient of increased terminal velocity (i.e., mass) is nearly balanced by the gradient of stronger updraft. This region is shown in Fig. 42 by $\overline{E_1H_1}$ and also $\overline{H_2H_3}$. Any stone in the very strongest updraft cannot increase its terminal velocity quickly enough to avoid rising to regions with colder temperatures and less liquid water. A hailstone in relatively weak updraft sinks to warmer temperatures because of its increased terminal velocity. This description agrees with the results of a one-dimensional detailed microphysical model by Danielsen et al. (1972). They found that the largest hailstones grow in 15 to 30 m s^{-1} updrafts. Browning and Foote (1976) also allude to this affect in their conceptual model. Their explanation

disagrees with this case in one important aspect. They hypothesize the hailstones traverse the updraft by turning away from the "embryo curtain" and advecting across the weak echo region (Fig. 3). In the storm reported here, the Doppler wind and reflectivity fields show the embryo curtain is aligned perpendicular to the updraft's major axis. The growth trajectories also show that the largest hail grows in this region. It seems likely that the embryo curtain actually demarcates the region of maximum hail growth. It seems appropriate, therefore, to rename this area as the "hail curtain." The hail curtain has important implications for modification attempts that will be mentioned later. Because of the possibility of large hail, this region should be penetrated with extreme caution by in situ sensors such as the T-28 armored aircraft (Sand and Schleusener, 1974).

The model also reveals one way in which a hailstone could grow very rapidly at fairly cold temperatures (<-15°C). The critical factor is that the hailstone must be large enough to grow in the wet mode in a mixed phase region even with relatively little liquid cloud water. If this occurs, the hailstone can actually grow at a faster rate than if the environmental water were all liquid. This is because when the hailstone surface is wet, any ice encountered will likely stick to the hailstone. Since there is no latent heat of fusion to be dissipated, more mass can be added than if the hailstone were collecting only supercooled liquid water. This situation occurrs in this model with a few hailstones caught in light horizontal flow on the southeastern updraft edge. The hailstones remain there for about 6 min while they grow to about 2 cm in diameter. They finally traverse across the updraft and grow in the wet mode despite the decreasing liquid and increasing ice water contents. The growth rate during the short traverse across the updraft is quite remarkable. The critical balance necessary for this type of growth occurs only in very restrictive model locations and may be an artifact. It is not unreasonable, however, to believe such ice crystal collection could occur. The possible enhanced growth potential makes this subject worthy of further study.

6.4 Implications for Modification

The model results provide insight into modification strategies for this storm type. In the following discussions it is assumed the modification goal will be to reduce the maximum hail size. Such side effects as decreased precipitation, more and smaller hailstones, and increased latent heat are not addressed.

Three hail suppression methods are currently in the forefront of modification techniques--glaciation, beneficial competition, and trajectory lowering. Glaciation involves freezing the supercooled water so that little is available for hail growth. The glaciation concept is generally regarded as unfeasible in storms with strong updrafts because of the high seeding rates required to freeze the liquid water. For example, Young (1977) calculated that an AgI seeding rate of between 0.1 and 1.0 kg min^{-1} km^{-2} would be required to glaciate 50% of cloud water between cloud base and the -15°C level. If the prime growth area is defined by the width of the hail curtain and the updraft, the horizontal area would be about 5x5 km, yielding a seeding rate of between 2.5 and 25 kg min^{-1}. Assuming a 30 min lifetime this requires 75 to 750 kg of seeding material.

The basis of beneficial competition is the production of additional embryos to compete with natural ones for the available liquid water. Targeting the seeding material to produce the artifical embryos is critical. This study shows that identifying these formation regions may prove to be quite difficult. If there is one locale from which large hail embryos emerge, it is not obvious from the presented data. Overall this approach looks quite difficult.

Trajectory lowering is essentially a form of competition. It differs in that the artifically induced and natural embryos are not colocated. Rather, the artificial embryos are targeted to grow in a lower trajectory so they deplete the liquid water before it reaches the prime growth region (Young, 1977). It is suggested that none of the artificial embryos will grow into large hail since they spend little or no time in the prime growth region. The critical problem is to find an area below the prime growth level where artificial embryos can grow to an optimally moderate size. In addition, artificial embryo trajectories should not be too far below the prime growth region. If they are, the greatest percentage of liquid water in the prime growth zone could come from condensation rather than advection from the lower levels. The 5 km level of Fig. 30 suggests a suitable area may exist in this supercell storm. If a sufficient number of embryos 2 to 6 mm in diameter can be produced southeast of core D, they could significantly decrease the liquid water available in the 6 to 8 km range. Figures 43 and 44 demonstrate the basis for this process. They show the growth history of two 6 mm embryos--one beginning at 5 km and the other directly above it at 7 km. Note that the two trajectories are basically parallel, but the lower hailstone only grows to 1.6 cm while the higher one exceeds 3 cm. Can appropriately sized embryos in sufficient quantity be created at the critical locations? Questions such as this can only be answered by detailed microphysical models and experimentation. This work shows, however, that the possibility does exist for successful suppression through trajectory lowering.

7. ACKNOWLEDGMENTS

Without the broad-based support of the National Severe Storms Laboratory (NSSL), headed by Dr. Edwin Kessler, this research effort would not have been possible. The following groups within NSSL were involved with the collection and reduction of data used in this study: Advanced Techniques, headed by Dr. Richard Doviak; Operations and Technology Transfer, headed by Mr. Ken Wilk; Engineering Support headed by Mr. Dale Sirmans, Computer and Data Processing headed by Ms. Kathryn Gray and later by Mr. William Bumgarner. The members of these groups are sincerely thanked for their expertise and effort. Mr. Michael Weible is especially acknowledged for his assistance on various programming efforts. Additional data were obtained from the University of Chicago/University of Illinois CHILL Doppler radar. A debt of gratitude is owed to the personnel of these two institutions for their cooperation and assistance.

The author has benefited from interactions with his colleagues at NSSL. Conversations with Messrs. Ed Brandes, Rodger Brown, Don Burgess, John Weaver, and Dr. Carl Hane were especially helpful. Dr. Ron Alberty took a keen interest in this work and his advice has been most useful. Ms. Nancy C. Knight is also thanked for her review of this dissertation.

Mr. Charles Clark, Mr. Robert Goldsmith, and Ms. Joan Kimpel performed the photography and graphics. Their technical skills and advice were of great benefit in figure construction. All three-dimensional perspective view graphics were produced by programs written by Mr. Vincent Wood.

Preliminary and final dissertation drafts were typed by Ms. Sandy Mudd and Ms. Terry Snodgrass. Their patience and thoroughness is much appreciated.

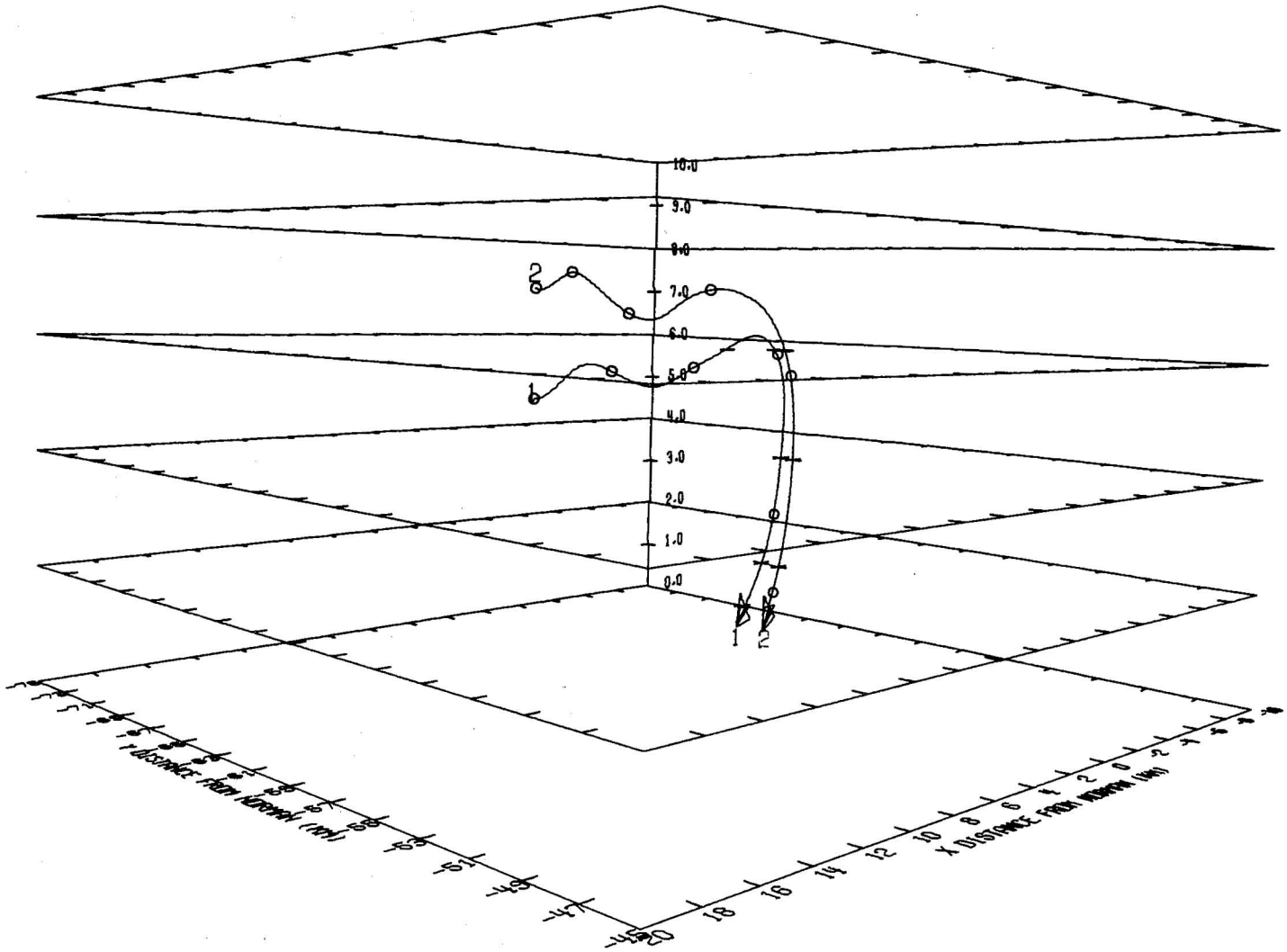

Figure 43. Three-dimensional hailstone trajectories. Trajectory 2 begins its growth 2 km directly above trajectory 1. Growth parameters are shown in Fig. 44. The observer is looking towards the south-southwest (225°). See Fig. 31 for further details.

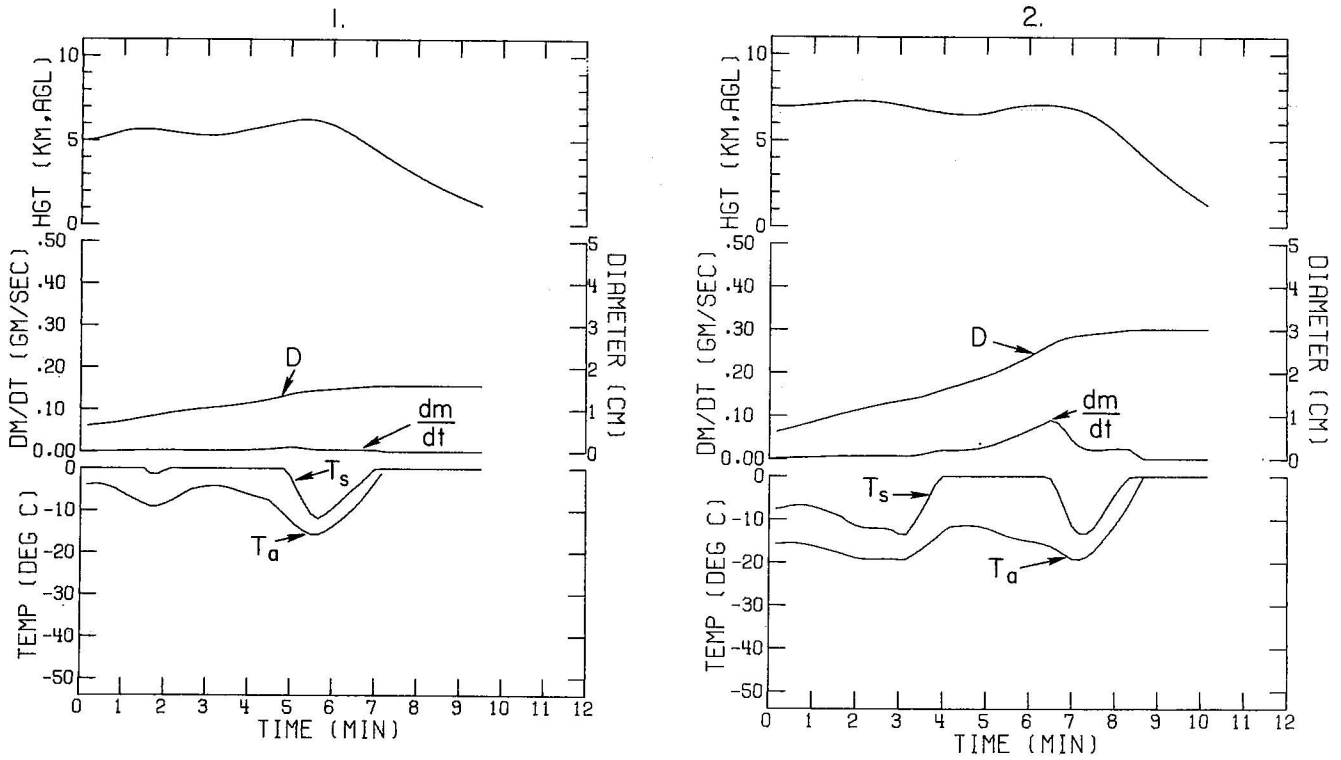

Figure 44. Time history of height and growth parameters of hailstone shown in Fig. 43. (1) Trajectory 1; (2) Trajectory 2. See Fig. 33 for further explanation.

The members of the dissertation committee, Drs. Stanley Barnes, Richard Doviak, Rex Inman, Martin Jischke, and Edwin Kessler, are thanked for their guidance and constructive criticism. The author especially acknowledges the Committee Chairman, Dr. John McCarthy, for his continuing interest and support. John was the perfect combination of mentor and devil's advocate.

The work in this dissertation was partially supported by National Science Foundation Grants ATM #74-03406A02 and ATM #781241 issued to the University of Oklahoma.

Certainly, my academic career could not have progressed this far without the initial support and encouragement of my parents, Price and Dorothy Nelson. To them I owe a great deal.

Finally, this work would never have been completed without the understanding of my wife, Marsha. I trust her tenure as editor, counselor, taskmaster, and friend was worth the effort.

8. REFERENCES

Alberty, R., J Weaver, D. Sirmans, J. Dooley, B. Bumgarner, 1977: Spring Program '76. NOAA Tech. Memo. ERL NSSL-83, National Severe Storms Lab., Norman, Okla., 130 pp.

Alusa, A. L., 1976: The occurrence and nature of hailstorms in Kericho, Kenya. Preprints, 2nd WMO Conf. on Weather Modification, Boulder, Colo., WMO No. 443, 299-256.

Armijo, L., 1969: A theory for the determination of wind and precipiation velocities with Doppler radars. J. Atmos. Sci., 26 (3), 570-573.

Ashworth, T., and Charles A. Knight, 1978: Cylindrical ice accretions as simulations of hail growth: I. Effects of rotation and of mixed clouds. J. Atmos. Sci., 35 (10), 1987-1996.

Atlas, D., 1977: The paradox of hail suppression. Science, 195, 139-145.

Bachelor, G. K., 1967: An introduction to fluid dynamics. Cambridge University Press, 615 pp.

Bailey, I. H., and W. C. Macklin, 1967: The surface configuration and internal structure of artificial hailstones. Quart. J. R. Meteorol. Soc., 94, 1-11.

Barge, B. L., and F. Bergwall, 1976: Fine scale structure of convective storms associated with hail production. Atmos. Sci. Div. Rept. 76-2, Alberta Research Council, 43 pp.

Barnes, S. L., 1978: Oklahoma thunderstorms on 29-30 April 1970. Part I: Morphology of a tornadic storm. Mon. Wea. Rev. 106 (5), 673-684.

_____, and S. P. Nelson, 1978: Oklahoma thunderstorms on 29-30 April 1970: Part IV. Study of a dissipating severe storm. Mon. Wea. Rev., 106 (5), 704-712.

Bensch, R. R., 1976: Airflow and thermodynamic features of a short-lived supercell hailstorm. Master Thesis, University of Oklahoma, Norman.

Bohne, A. R., and R. C. Srivastava, 1975: Random errors in wind and precipitation fall speed measurement by a triple Doppler radar system. Lab. for Atmospheric Probing Tech. Rept. No. 37, Univ. of Chicago-Illinois Institute of Technology, Chicago, 44 pp.

Borland, S. W., 1977: Hail: A review of hail science and hail suppression. Part II. Hail Suppression. Progress in assessing its costs and benefits. Edited by G. Brant Foote and Charles A. Knight. Meteor. Monogr. 16 (38), Amer. Meteor. Soc., Boston, 155-176.

Braham, R. R., 1963: Some measurements of snow pellet bulk-densities. J. Appl. Meteor. 2 (4), 498-500.

Brandes, E. A., 1977: Flow in severe thunderstorms observed by dual-Doppler radar. Mon. Wea. Rev., 105, 113-120.

_____, 1978: Mesocyclone evolution and tornadogenesis: Some observations. Mon. Wea. Rev., 106 (7), 995-1011.

Brown, R. A., 1976: Single Doppler radar data acquisition and analysis. Appendix E in The Union City, Oklahoma Tornado of 24 May 1973, R. A. Brown, Ed. NOAA Tech. Memo. ERL NSSL-80, 215-228 [NTIS PB269443/AS].

_____ and R. L. Peace, Jr., 1968: Mesoanalysis of convective storms utilizing observations from two Doppler radars. Proceedings, 13th Radar Meteorology Conf., Montreal, Amer. Meteor. Soc., Boston, 188-191.

_____, D. W. Burgess, J. K. Carter, L. R. Lemon, and D. Sirmans, 1975: NSSL dual Doppler radar measurements in tornadic storms: A preview. Bull. Amer. Meteor. Soc., 56 (5), 524-526.

_____, C. R. Safford, S. P. Nelson, D. W. Burgess, W. C. Bumgarner, M. L. Weible, L. C. Fortner, and R. J. Hilbert, 1980: Multiple Doppler radar analysis of severe thunderstorms: Designing a general analysis system. (To be published).

Browning, K. A., 1963: The growth of large hail within a steady updraught. Quart J. R. Meteorol. Soc., 89, 490-506.

_____, 1977: Hail: The structure and mechanisms of hailstorms. A Review of hail science and hail suppression, Meteor. Monogr., No. 38, G. B. Foote and C. A. Knight, Eds., Amer. Meteor. Soc., Boston, 1-39.

_____, J. Hallett, T. W. Harrold, and D. Johnson, 1968: The collection and analysis of freshly fallen hailstones. J. Appl. Meteor., 7 (4), 603-612.

_____ and G. B. Foote, 1976: Airflow and hail growth in supercell storms and some implications for hail suppression. Quart. J. R. Meteorol. Soc., 102, 499-533.

_____ and D. Atlas, 1977: Some new approaches in hail suppression experiments. J. Appl. Meteor., 16 (4), 327-332.

Burgess, D. W., R. A. Brown, L. R. Lemon, and C. R. Safford, 1977: Evolution of a tornadic thunderstorm. Preprints, Tenth Conf. on Severe Local Storms, Omaha, Amer. Meteor. Soc., Boston, 84-89.

Byers, H. R., and R. R. Braham, 1949: The thunderstorm. U.S. Government Printing Office, 287 pp.

Carnahan, B., H. Luther, and J. Wilkes, 1969: Applied numerical methods. John Wiley and Sons, Inc., New York, 604 pp.

Carras, J. N., and W. C. Macklin, 1975. The opacity of accreted ice. Quart. J. R. Meteorol. Soc., 101, 203-206.

Changnon, S. A., R. J. Davis, B. C. Farhar, J. E. Haas, J. L. Ivers, M. V. Jones, D. A. Klein, D. Mann, G. M. Morgan, Jr., S. T. Sonka, E. R. Swanson, C. R. Taylor, J. Van Blokland, 1977: Hail suppression. Impacts and issues. Final Rpt. Tech. Assessment of the Suppression of Hail. ERP 75-09980. Office of Exploratory Research and Problem Assessment. RANW-NSF, 430 pp.

Chisholm, A. J., and J. H. Renick, 1972: The kinematics of multicell and supercell Alberta hailstorms. Hail Studies Rpt. 72-2, Research Council of Alberta, 24-31.

Danielsen, E., R. Bleck, and D. Morris, 1972: Hail growth by stochastic collection in a cumulus model. J. Atmos. Sci., 29, 135-155.

Davies-Jones, R. P., 1974: Discussion of measurements inside high speed thunderstorm updrafts. J. Appl. Meteor., 13, 710-717.

Dennis, A. S., 1977: Hail A review of hail science and hail suppression. Part II. Hail suppression. Hail suppression concepts and seeding methods. Meteor. Monogr., 16 (38), Amer. Meteor. Soc., Boston, 181-191.

_____, C. A. Schock, and A. Koscielski, 1970: Characteristics of hailstorms of Western South Dakota. J. Appl. Meteor., 9, 127-135.

Doviak, R. J., P. S. Ray, R. G. Strauch, and L. J. Miller, 1976: Error estimation in wind fields from dual Doppler radar measurements. J. Appl. Meteor., 15 (8), 868-878.

English, M., 1973: Alberta hailstorms. Part II. Growth of large hail in the storm. Meteor., Monogr., 14 (36), 37-98.

Environmental Science Services Administration - National Aeronautics and Space Administration, 1966: U.S. standard atmosphere supplements, 1966. U.S. Government Printing Office, Washington, D.C.

Federer, B., 1977: Hail: A review of hail science and hail suppression. Part II. Hail suppression methods and results in Europe and in the U.S.S.R. Meteor. Monogr., 16 (38). Edited by G. Brant Foote and Charles A. Knight, Amer. Meteor. Soc., Boston, 215-223.

Fletcher, N. H., 1966: The physics of rainclouds. Cambridge University Press, 390 pp.

Foote, G. B., and C. A. Knight (Eds.), 1977: Hail: A review of hail science and hail suppression. Meteor. Monogr., 16 (38), Amer. Meteor.Soc., Boston, 277 pp.

Gal-Chen, T., 1978: A method for the initialization of the anelastic equations: Implications for matching models with observations. Mon. Wea. Rev., 106 (5), 587-606.

Galway, J. G., 1956: The lifted index as a predictor of latent instability. Bull. Amer. Meteor. Soc., 37, 528-529.

Goff, R. C., 1976: Vertical structure of thunderstorm outflows. Mon. Wea. Rev., 104 (11), 1429-1440.

____, J. T. Lee, and E. A. Brandes, 1977: Gust front analytical study. FAA Rept. No. RD-77-119, Federal Aviation Administration, Washington, D.C., 126 pp.

Haltiner, G. J., 1971: Numerical weather prediction. John Wiley & Sons, Inc., New York, 317 pp.

Hane, C. E., and B. C. Scott, 1978: Temperature and pressure perturbations within convective clouds derived from detailed air motion information: Preliminary testing. Mon. Wea. Rev., 106 (5), 654-661.

Harris, F. I., J. C. Fankhauser, and J. R. Miller, 1978: A complex convective storm system studied by multiple Doppler radar analysis. Preprints, 18th Conf. on Radar Meteor., Amer. Meteor., Soc., Boston, 252-259.

Heymsfield, A. J., 1978: The characteristics of graupel particles in northeastern Colorado cumulus congestus clouds. J. Atmos. Sci., 35, 284-295.

_____, P. N. Johnson, and J. E. Dye, 1978a: Observations of moist adiabatic ascent in northeast Colorado cumulus congestus clouds. J. Atmos. Sci., 35 (9), 1689-1703.

_____, D. J. Musil, and G. B. Foote, 1978b: The Colorado hailstorm of 22 July 1976: III. Characteristics of the updraft region. Preprints, 18th Conf. on Radar Meteorology, Amer. Meteor. Soc., Boston, 226-231.

_____, C. A. Knight, and J. E. Dye, 1979: Ice initiation in unmixed cores in northeast Colorado cumulus congestus clouds. J. Atmos. Sci., 36 (11), 2216-2229.

_____, A. Jameson, and H. Frank, 1980: Hail growth mechanisms in a Colorado storm: Part II. Hail formation processes. J. Atmos. Sci., to be published.

Heymsfield, G. M., 1978: Kinematic and dynamic aspects of the Harrah tornadic storm analyzed from dual-Doppler radar data. Mon. Wea. Rev., 106 (2), 233-254.

Hoerner, S. F., 1958: Fluid-dynamic drag. Box 342, Brick Town, New Jersey, published by the author, 259 pp.

Kelly, T. J., H. W. Frank, G. B. Foote, and C. G. Wade, 1978: The Colorado hailstorm of 22 July 1976: II. Internal circulation. Preprints, 18th Conf. on Radar Meteorology, Amer. Meteor. Soc., Boston, 219-225.

Kessler, E., 1969: On the distribution and continuity of water substances in atmospheric circulations. Meteor. Monogr., 10 (32), Amer. Meteor. Soc., Boston, 84 pp.

Knight, C. A., and N. C. Knight, 1970: Hailstone embryos. J. Atmos. Sci., 27 (4), 659-666.

_____, T. Ashworth, and N. C. Knight, 1978: Cylindrical ice accretions as simulations of hail growth: II. The structure of fresh and annealed accretions. J. Atmos. Sci., 35 (10), 1997-2009.

Knight, N. C., 1980: The climatology of hailstone embryos. Submitted to the J. Atmos. Sci.

_____ and C. A. Knight, 1978: South African lowveld hailstone embryos. Preprints, Conf. on Cloud Physics and Atmospheric Electricity, Issaquah, Amer. Meteor. Soc., Boston, 194-197.

Kropfli, R. A., and L. J. Miller, 1975: Thunderstorm flow patterns in three dimensions. Mon. Wea. Rev., 103, 70-71.

Latham, J., and C. P. R. Saunders, 1970: Experimental measurements of the collection efficiencies of ice crystals in electric fields. Quart. J. R. Meteorol. Soc., 96, 257-265.

Lemon, L. R., and C. A. Doswell III, 1979: Severe thunderstorm evolution and mesocyclone structure as related to tornadogenesis. Mon. Wea. Rev., 107 (9), 1184-1197.

Levi, L. and A. Aufdermaur, 1970: Crystallographic orientation and crystal size in cylindrical accretions of ice. J. Atmos. Sci., 27 (3), 443-452.

Lhermitte, R. M., 1970: Dual-Doppler radar observations of convective storm circulation. Preprints, 14th Conf. on Radar Meteorology, Tucson, Amer. Meteor. Soc., Boston, 139-144.

List, R., 1963: General heat and mass exchange of spherical hailstones. J. Atmos. Sci., 20, 189-197.

____, R. B. Charlton, and P. I. Buttulus, 1968: A numerical experiment on the growth and feedback mechanisms of hailstones in a one-dimensional steady-state model cloud. J. Atmos. Sci., 25 (6), 1016-1074.

____, P. I. Joe, G. Lesins, P. R. Kry, M. R. deQuervain, J. D. McTaggart-Cowan, P. W. Stagg, E. P. Lozowski, E. Freire, R. E. Stewart, C. G. List, M. C. Steiner, and J. Von Niederhausern, 1976: On the variation of the collection efficiencies of icing cylinders. Preprints, Intl'l. Conf. on Cloud Physics, Boulder, Amer. Meteor. Soc., Boston, 233-239.

Ludlam, F. H., 1958: The hail problem. Nubila, 1, 12-96.

Macklin, W. C., 1963: Heat transfer from hailstones. Quart. J. R. Meteorol. Soc., 89, 360-369.

_____, 1963: Hail A review of hail science and hail suppression. Part I. Hail physic. The characteristics of natural hailstones and their interpretation. Meteor. Monogr., 16 (38), Ed. by G. Brant Foote and Charles A. Knight, Amer. Meteor. Soc., Boston, 65-88.

_____ and F. H. Ludlam, 1961: The fallspeed of hailstones. Quart. J. R. Meteorol. Soc., 87, 72-81.

_____ and I. H. Bailey, 1966: On the critical liquid water concentrations of large hailstones. Quart. J. R. Meteorol. Soc., 92, 297-300.

Marwitz, J. D., 1972: The structure and motion of severe hailstorms. Part I. Supercell storms. J. Appl. Meteor., 11, 166-179.

Mason, B. J., 1971: The physics of clouds. Clarendon Press, Oxford, 671 pp.

Matson, R., and A. W. Huggins, 1979: Field observations of the kinematics of hailstones. NCAR Tech. Note NCAR/TN-139+STR, 68 pp.

Morgan, G. M., Jr., 1973: A general description of the hail problem in the Po Valley of Northern Italy. J. Appl. Meteor., 12 (2), 338-353.

Mueller, E., and E. Silha, 1978: Unique features of the CHILL radar system. 18th Conf. on Radar Meteorology, Amer. Meteor. Soc., Boston, 381-382.

Musil, D. J., A. S. Dennis, and W. Sand, 1975: Hailstone growth in a two dimensional kinematic cloud model. Proceedings, Ninth Conf. on Severe Local Storms, Norman, Amer. Meteor Soc., Boston, 452-453.

_____, P. L. Smith, J. R. Miller, J. H. Killinger, and J. L. Halvorson, 1977: Characteristics of vertical velocities observed in T-28 penetrations of hailstorms. Preprints, Sixth Conf. on Planned and Inadvertent Weather Modification, Amer. Meteor. Soc., Boston, 166-169.

Nelson, S. P., and R. R. Braham, 1975: Detailed observational study of a weak echo region. Pageoph, 113, 735-746.

_____ and S. K. Young, 1979: Characteristics of Oklahoma hailfalls and hailstorms. J. Appl. Meteor., 18 (3), 339-347.

O'Brien, J. J., 1970: Alternate solutions to the classical vertical velocity problem. J. Appl. Meteor., 9 (2), 197-203.

Orville, H. D., 1977: Hail: A review of hail science and hail suppression. Part I. Hail physics. A review of hailstone-hailstorm numerical simulations. Meteor. Monogr., 16 (38). Edited by G. Brant Foote and Charles A. Knight, Amer. Meteor. Soc., Boston, 49-62.

_____, R. D. Farley, D. J. Musil, F. J. Kopp, and M. M. Bradley, 1979: Numerical simulations of hailstorms and hailstones. Institute of Atmospheric Sciences, Rpt. No. 79-3, South Dakota School of Mines and Technology, Rapid City, 96 pp.

Paluch, I. R., 1978: Size sorting of hail in a three-dimensional updraft and implications for hail suppression. J. Appl. Meteor., 17 (6), 763-777.

Passarelli, R. E., Jr., 1978: Theoretical and observational study of snow size spectra and snowflake aggregation efficiencies. J. Atmos. Sci., 35 (5), 882-889.

Petterssen, S., 1956: Weather analysis and forecasting. Volume II. Weather and weather systems. McGraw-Hill Book Co., New York, 266 pp.

Pflaum, J. C. J. J. Martin, and H. R. Pruppacher, 1978: A wind tunnel investigation of the hydrodynamic behavior of growing, freely falling graupel. Quart. J. R. Meteorol. Soc., 104, 179-187.

Ray, P. S., 1976: Vorticity and divergence fields within tornadic storms from dual-Doppler observations. J. Appl. Meteor., 15 (8), 879-890.

___ and K. K. Wagner, 1976: Multiple Doppler radar observations of storms. Geophys. Res. Letters, 3 (3), 189-191.

___, R. J. Doviak, G. B. Walker, D. Sirmans, J. Carter, and W. C. Bumgarner, 1975: Dual-Doppler observations of a tornadic storm. J. Appl. Meteor., 14 (8), 1521-1530.

___, K. K. Wagner, K. W. Johnson, J. J. Stephens, W. C. Bumgarner, E. A. Mueller, 1978: Triple Doppler observations of a convective storm. J. Appl. Meteor., 17, 1201-1212.

Rogers, D. C., 1974: The aggregation of natural ice crystals. Rept. No. AR110, Dept. Atmos. Resources, Univ. of Wyoming, 35 pp.

Rosinski, J., C. A. Knight, C. T. Nagamoto, G. M. Morgan, and N. C. Knight, 1979: Further studies of large, water-insoluble particles within hailstones. J. Atmos. Sci. 35 (5), 882-891.

Ryan, B. F., 1974: Growth of drops by coalescence: The effect of different collection kernals and of additional growth by condensation. J. Atmos. Sci., 31 (7), 1942-1948.

Sand, W. R., 1976: Observations in hailstorms using the T-28 aircraft system. J. Appl. Meteor., 15 (8), 641-650.

____, and R. A. Schleusener, 1974: Development of an armored T-28 aircraft for probing hailstorms. Bull. Amer. Meteor. Soc., 55, 1115-1122.

Sansom, H. W., 1968: A four year hail suppression experiment using explosive rockets. Proceedings, Intl'l. Conf. on Cloud Physicas, Toronto, 768-772.

Sartor, J. D., and T. W. Cannon, 1977: Collating airborne and surface observations of the microstructure of precipitating continental convective clouds. J. Appl. Meteor., 16 (7), 697-707.

_____ and T. W. Cannon, 1977: The observed and computed microstructure of hail-producing clouds in northeastern Colorado. J. Appl. Meteor., 16 (7), 708-714.

Sasaki, Y., 1958: An objective analysis based on the variational method. J. Meteor. Soc., Japan, 36, 77-88.

Sax, R. I., S. A. Changnon, L. O. Grant, W. F. Hitschfeld, P. V. Hobbs, A. M. Kahan, and J. Simpson, 1975: Weather modification: Where are we now and where should we be going? An editorial overview. J. Appl. Meteor., 14 (5), 652-672.

Schumann, T. E., 1938: The theory of hailstone formation. Quart. J. R. Meteorol. Soc., 64, 3-17.

Shapiro, R., 1970: Smoothing, filtering, and boundary effects. Review of Geophys. and Space Phy., 8 (2), 359-387.

Shuman, Frederic G., 1957: Numerical methods in weather prediction: II. Smoothing and filtering. Mon. Wea. Rev., 85 (11), 357-361.

Twomey, S., 1966: Computations of rain formation by coalescence. J. Atmos. Sci., 23 (4), 405-411.

U.S. Department of Commerce, 1976: Storm Data. Vol. 18 (5), Environmental Data Service, NOAA, Asheville.

Weaver, J. F., 1979: Private communications.

Wilhelmson, R. B., and J. B. Klemp, 1978: A numerical study of storm splitting that lends to long-lived storms. J. Atmos. Sci., 35 (10), 1974-1986.

Wilson, D. A., 1970: The kinematic behavior of spherical particles in an accelerating environment. NOAA Tech. Rpt. ERL 187-WPL-13, Wave Propagation Lab., Boulder, Colo., 25 pp.

Wood, V. T., D. W. Burgess, and R. A. Brown, 1979: Single Doppler radar evolution of the Del City, Oklahoma tornado cyclone. Preprints, 11th Conf. on Severe Local Storms, Amer. Meteor. Soc., Boston, 545-548.

Young, K. C., 1977: Hail: A review of hail science and hail suppression. Part II. Hail suppression. A numerical examination of some hail suppression concepts. Meteor. Monogr., 16 (38), Edited by G. Brante Foote and Charles A. Knight, Amer. Meteor. Soc., Boston, 195-214.

_____, 1978: On the role of mixing in promoting competition between growing hailstones. J. Atmos. Sci., 35 (11), 2190-2193.

Young, R. G. E., and K. A. Browning, 1967: Wind tunnel tests of simulated spherical hailstones with variable roughness. J. Atmos. Sci., 24 (1), 58-62.

Ziegler, C. L., 1978: A dual Doppler variational objective analysis as applied to studies of convective storms. NOAA Tech. Memo. ERL NSSL-85, Norman, 116 pp.

APPENDIX A

MULTIPLE DOPPLER PROGRAMMING SYSTEM

The triple Doppler synthesis techniques described in Chapter 2 represent only one step in the complex process of multiple Doppler data analysis. The following briefly describes procedures used in analysis of data in this study. This discussion closely follows that of Brown et al., 1980. The reader is referred to this reference for a more complete treatment.

Figure A.1 (after Brown et al., 1980) shows the various steps necessary to process multiple Doppler data. These are:

1. Consolidation
2. Editing
3. Interpolation to a Grid
4. Synthesis
5. Kinematic Analysis
6. Display

Programs to perform editing and triple Doppler synthesis were contributed by this author.

A.1 Consolidation

The first step is to read the data from the input tapes. At this stage all data formats are standardized. Spatial limits are set to retain only data necessary to perform the desired analyses. This procedure saves time in the following processing steps.

A.2 Editing

This is one of the most critical steps in the synthesis procedure. Data errors are most easily recognized at this stage. Editing is an all encompassing procedure that involves checking and/or correcting various aspects of the data. Most required modifications can be accomplished at the same time. Specifically, the following are checked.

1. Equipment Problems - This includes dropped bits on the digital recording, incorrect dates, times, elevations, azimuths, etc. Under normal circumstances, the tapes should be free of such problems before being released to the user. Problems do creep through, however, and the user must check for them.

2. Noisy Data - Incorrect mean velocity estimates usually occur because of low signals. The obvious solution is to allow only data with high signal-to-noise (SNR) ratios into the analysis. A high SNR cut eliminates most bad data but it also deletes many good velocity estimates. A low cut retains most good estimates but allows many bad points into the analysis. If the user is not interested in portions of the storm with low signal, then the SNR should be set quite high. If analysis in such areas as weak echo regions is desired, then the cut should be low. In the latter case, the user must inspect the data carefully and eliminate points that appear to be in error. This requires a great amount of time and subjectivity. In almost all cases some bad data will escape detection. This results in anomalous velocities often on the echo's periphery.

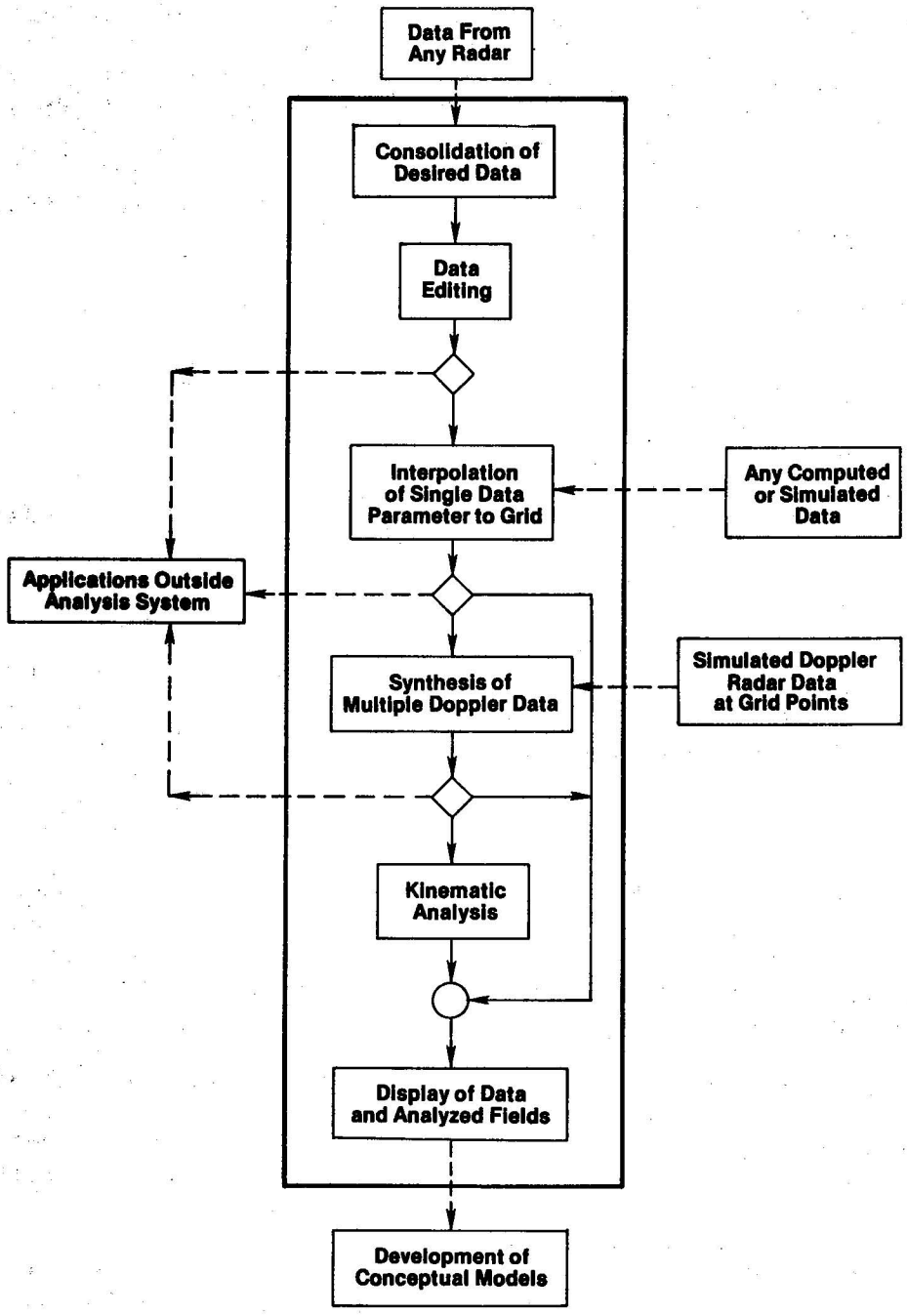

Figure A1. Steps involved in processing multiple Doppler data (after Brown et al., 1980). The multiple Doppler programming system is enclosed within the heavy black line.

3. Velocity Aliasing - Each radar is characterized by a maximum unambiguous velocity ($\pm v_a$). If the measured velocity exceeds $\pm v_a$, it will "fold" and appear as a velocity in error by $2v_a$. For example, v_a for the Norman Doppler is ± 35 m s^{-1}. A +40 m s^{-1} velocity will appear as -30 m s^{-1} (40 - 2 x 35 m s^{-1}). Routines exist to automatically detect and unfold these aliased velocities. The most commonly used method is a shear check between radial data points. This is based on the assumption that naturally occurring radial shears will always be less than those caused by velocity folding. This technique sometimes fails because of noisy data or, more rarely, extremely large natural shears. Because of these failures, however, the user must inspect the entire Doppler velocity field.

A.3 Interpolation to a Grid

For this study the analysis domain is typically 60x60x20 km or smaller. True north is aligned through the grid center. The "horizontal" planes are actually curved concentric arcs at constant heights above the ground. The three dimensional locations of each grid and data point are known in relationship to a fixed origin (usually one of the radars). Data are interpolated to the grid using a Cressman weighting function (Brown, 1976) with a variable radius of influence proportional to the data spacing. Typically 10 to 20 data points are used in computing a grid point value. Since a tilt sequence is completed over a finite time period (~5 min), the data are adjusted before interpolation to a common reference time by a time-to-space correction using storm motion as the displacement vector. These spatial corrections are typically less than 1 km. For further analysis these quasi-horizontal planes are assumed to be flat, rectilinear grids. This results in distortions of less than 10 m. Such distortions are much smaller than uncertainties in data positioning due to finite beam widths, antenna alignment, etc.

A.4 Synthesis

The synthesis techniques used are described in Chapter II.

A.5 Kinematic Analysis/Display

Using the computed u,v,w, and ω fields, the kinematic and display programs compute such quantities as divergence, vorticity, wind vectors, etc., and display them on any horizontal or vertical section. Examples of these can be seen in Chapter 4.

APPENDIX B

THREE DIMENSIONAL SHUMAN FILTER

B.1 Introduction

It is beneficial to filter data not only to suppress numerical problems due to noisy data (see Chapter 2), but sometimes also for aesthetic reasons. Because of its widespread use, the Shuman Filter (Shuman, 1957) was chosen for extension to three dimensions. Even though the filter is being developed for use on multi-Doppler data, it has general applicability to any scalar quantity. The main caveat is that since so much data is required to filter a point (27 points), missing data and boundary problems can be acute.

B.2 Derivation of Three Dimensional Shuman Filter

This derivation follows that of Shuman (1957) and Shapiro (1970). The "unit cell" necessary to filter the scalar "f" at point i,j,k is shown in Fig. B1. The subscripts represent the three orthogonal directions as indicated on the middle plane of Fig. B1.

The two dimensional filter is given by (Shuman, Shapiro, op. cit.)

$$\overset{-j}{\underset{-i}{f_{i,j}}} = f_{i,j,k} + (1-S)\frac{S}{2}\nabla^2 f_{i,j,k} + \frac{S^2}{4}\left(f_{i+1,j+1,k} + f_{i+1,j-1,k} + f_{i-1,j+1,k} + f_{i-1,j-1,k} - 4 f_{i,j,k}\right) \qquad (1)$$

where S is an arbitrary parameter that determines the response of the filter (R_2) and

$$\nabla^2 f_{i,j,k} = f_{i+1,j,k} + f_{i-1,j,k} + f_{i,j+1,k} + f_{i,j-1,k} - 4f_{i,j,k} \qquad (2)$$

The three dimensional filter is derived by substituting $\bar{f}^{k}$ for f in Eq. (1) where

$$\overset{-k}{f_{i,j,k}} = (1-S)\, f_{i,j,k} + \frac{S}{2}\left(f_{i,j,k+1} + f_{i,j,k-1}\right)$$

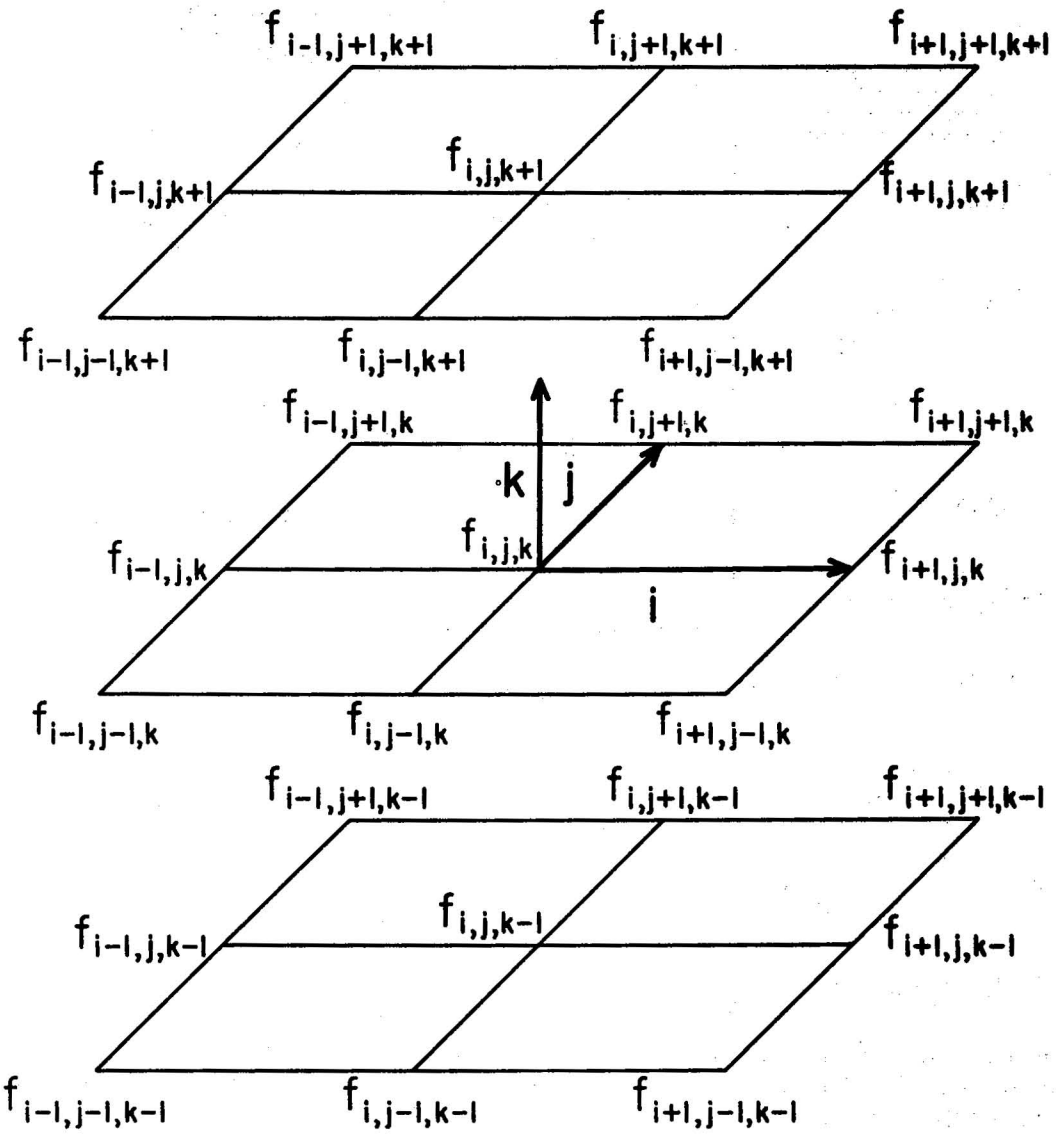

Figure B1. Unit cell needed to filter the scalar f located at point i, j, k. The subscripts refer to the three orthogonal directions indicated on the middle plane.

hence,

$$
\begin{aligned}
-k\\
-j\\
-i\\
f_{i,j,k} &= f_{i,j,k} + \frac{S}{2}\nabla^3 f_{i,j,k} + (1-S)\frac{S^2}{4}[\nabla^2 f_{i,j,k+1}\\
&+ \nabla^2 f_{i,j,k-1} - 4\nabla^2 f_{i,j,k}] - \frac{S^3}{2}\nabla^2 f_{i,j,k} \qquad (3)\\
&(1-S)\frac{S^2}{4}[f_{i+1,j+1,k} + f_{i+1,j-1,k} + f_{i-1,j+1,k} + f_{i=1,j-1,k} - 4f_{i,j,k}]\\
&+ \frac{S^3}{8}[f_{i+1,j+1,k+1} + f_{i+1,j-1,k+1} + f_{i-1,j+1,k+1} + f_{i-1,j-1,k+1}\\
&- 4f_{i,j,k+1} + f_{i+1,j+1,k-1,} + f_{i+1,j-1,k-1} + f_{i-1,j+1,k-1}\\
&+ f_{i-1,j-1,k-1} - 4f_{i,j,k-1}]
\end{aligned}
$$

where ∇^2 is given by Eq. (2) and

$$
\begin{aligned}
\nabla^3 f_{i,j,k} &= f_{i,j+1,k} + f_{i,j-1,k} + f_{i+1,j,k} + f_{i-1,j,k} + f_{i,j,k+1}\\
&+ f_{i,j,k-1} - 6f_{i,j,k}
\end{aligned}
$$

B.3 Response Function

The response function is the ratio of the amplitude of a filtered to an unfiltered wave. Following the derivation of the above references, the three dimensional response function (R_3) can be shown to be

$$R_3 = \{1-S[1-\cos(\ell_x \Delta x)]\}\ \{1-S[1-\cos(\ell_y \Delta y)]\}\ \{1-S[1-\cos(\ell_z \Delta z)]\}$$

where ℓ_x, ℓ_y, ℓ_z are the i,j,k wave numbers ($\frac{2\pi}{L}$ where L is the wavelength); Δx, Δy, Δz are the grid spacing in the i,j,k directions. Table B1 shows R_3 as a function of $L(L=L_x=L_y=L_z)$ for S=0.5, S=-0.5, and for the two used in tandem (T). One pass with the tandem filter reduces $4\Delta x$ waves to 42% of their original amplitude while maintaining 90% of the waves as small as $7\Delta x$. The response for multiple passes with the tandem filter (T^n) are also shown in Table B1. For most circumstances, only one tandem pass is used for the Doppler analysis.

No. 23 Purposes and Programs of the National Severe Storms Laboratory, Norman, Oklahoma. Edwin Kessler. December 1964. 17 p. (PB-166675)

No. 24 Papers on Weather Radar, Atmospheric Turbulence, Sferics and Data Processing. August 1965. 139 p. (AD-621586)

No. 25 A Comparison of Kinematically Computed Precipitation with Observed Convective Rainfall. James C. Fankhauser. September 1965. 28 p. (PB-168445)

No. 26 Probing Air Motion by Doppler Analysis of Radar Clear Air Returns. Roger M. Lhermitte. May 1966. 37 p. (PB-170636)

No. 27 Statistical Properties of Radar Echo Patterns and the Radar Echo Process. Larry Armijo. May 1966. The Role of the Kutta-Joukowski Force in Cloud Systems with Circulation. J. L. Goldman. May 1966. 34 p. (PB-170756)

No. 28 Movement and Predictability of Radar Echoes. James Warren Wilson. November 1966. 30 p. (PB-173972)

No. 29 Notes on Thunderstorm Motions, Heights, and Circulations. T. W. Harrold, W. T. Roach, and Kenneth E. Wilk. November 1966. 51 p. (AD-644899)

No. 30 Turbulence in Clear Air Near Thunderstorms. Anne Burns, Terence W. Harrold, Jack Burnham, and Clifford S. Spavins. December 1966. 20 p. (PB-173992)

No. 31 Study of a Left-Moving Thunderstorm of 23 April 1964. George R. Hammond. April 1967. 75 p. (PB-174681)

No. 32 Thunderstorm Circulations and Turbulence from Aircraft and Radar Data. James C. Fankhauser and J. T. Lee. April 1967. 32 p. (PB-174860)

No. 33 On the Continuity of Water Substance. Edwin Kessler. April 1967. 125 p. (PB-175840)

No. 34 Note on the Probing Balloon Motion by Doppler Radar. Roger M. Lhermitte. July 1967. 14 p. (PB-175930)

No. 35 A Theory for the Determination of Wind and Precipitation Velocities with Doppler Radars. Larry Armijo. August 1967. 20 p. (PB-176376)

No. 36 A Preliminary Evaluation of the F-100 Rough Rider Turbulence Measurement System. U. O. Lappe. October 1967. 25 p. (PB-177037)

No. 37 Preliminary Quantitative Analysis of Airborne Weather Radar. Lester P. Merritt. December 1967. 32 p. (PB-177188)

No. 38 On the Source of Thunderstorm Rotation. Stanley L. Barnes. March 1968. 28 p. (PB-178990)

No. 39 Thunderstorm - Environment Interactions Revealed by Chaff Trajectories in the Mid-Troposphere. James C. Fankhauser. June 1968. 14 p. (PB-179659)

No. 40 Objective Detection and Correction of Errors in Radiosonde Data. Rex L. Inman. June 1968. 50 p. (PB-180284)

No. 41 Structure and Movement of the Severe Thunderstorms of 3 April 1964 as Revealed from Radar and Surface Mesonetwork Data Analysis. Jess Charba and Yoshikazu Sasaki. October 1968. 47 p. (PB-183310)

No. 42 A Rainfall Rate Sensor. Brian E. Morgan. November 1968. 10 p. (PB-183979)

No. 43 Detection and Presentation of Severe Thunderstorms by Airborne and Ground-based Radars: A Comprehensive Study. Kenneth E. Wilk, John K. Carter, and J. T. Dooley. February 1969. 56 p. (PB-183572)

No. 44 A Study of a Severe Local Storm of 16 April 1967. George Thomas Haglund. May 1969. 54 p. (PB-184970)

No. 45 On the Relationship Between Horizontal Moisture Convergence and Convective Cloud Formation. Horace R. Hudson. March 1970. 29 p. (PB-191720)

No. 46 Severe Thunderstorm Radar Echo Motion and Related Weather Events Hazardous to Aviation Operations. Peter A. Barclay and Kenneth E. Wilk. June 1970. 63 p. (PB-192498)

No. 47 Evaluation of Roughness Lengths at the NSSL-WKY Meteorological Tower. Leslie D. Sanders and Allen H. Weber. August 1970. 24 p. (PB-194587)

No. 48 Behavior of Winds in the Lowest 1500 ft in Central Oklahoma: June 1966-May 1967. Kenneth C. Crawford and Horace R. Hudson. August 1970. 57 p. (N71-10615)

No. 49 Tornado Incidence Maps. Arnold Court. August 1970. 76 p. (COM-71-00019)

No. 50 The Meteorologically Instrumented WKY-TV Tower Facility. John K. Carter. September 1970. 18 p. (COM-71-00108)

No. 51 Papers on Operational Objective Analysis Schemes at the National Severe Storms Forecast Center. Rex L. Inman. November 1970. 91 p. (COM-71-00136)

No. 52 The Exploration of Certain Features of Tornado Dynamics Using a Laboratory Model. Neil B. Ward. November 1970. 22 p. (COM-71-00139)

No. 53 Rawinsonde Observation and Processing Techniques at the National Severe Storms Laboratory. Stanley L. Barnes, James H. Henderson and Robert J. Ketchum. April 1971. 245 p. (COM-71-00707)

No. 54 Model of Precipitation and Vertical Air Currents. Edwin Kessler and William C. Bumgarner. June 1971. 93 p. (COM-71-00911)

No. 55 The NSSL Surface Network and Observations of Hazardous Wind Gusts. Operations Staff. June 1971. 20 p. (COM-71-00910)

No. 56 Pilot Chaff Project at the National Severe Storms Laboratory. Edward A. Jessup. November 1971. 36 p. (COM-72-10106)

No. 57 Numerical Simulation of Convective Vortices. Robert P. Davies-Jones and Glenn T. Vickers. November 1971. 27 p. (COM-72-10269).

No. 58 The Thermal Structure of the Lowest Half Kilometer in Central Oklahoma: December 9, 1966-May 31, 1967. R. Craig Goff and Horace R. Hudson. July 1972. 53 p. (COM-72-11281)

No. 59 Cloud-to-Ground Lightning Versus Radar Reflectivity in Oklahoma Thunderstorms. Gilbert D. Kinzer. September 1972. 24 p. (COM-73-10050)

No. 60 Simulated Real Time Displays of Velocity Fields by Doppler Radar. L. D. Hennington and G. B. Walker. November 1972. 10 p. (COM-73-10515)

No. 61 Gravity Current Model Applied to Analysis of Squall-Line Gust Front. Jess Charba. November 1972. 58 p. (COM-73-10410)

No. 62 Mesoscale Objective Map Analysis Using Weighted Time-Series Observations. Stanley L. Barnes. March 1973. 60 p. (COM-73-10781)

No. 63 Observations of Severe Storms on 26 and 28 April 1971. Charles L. Vlcek. April 1973. 19 p. (COM-73-11200)

No. 64 Meteorological Radar Signal Intensity Estimation. Dale Sirmans and R. J. Doviak. September 1973. 80 p. (COM-73-11923/2AS)

No. 65 Radiosonde Altitude Measurement Using Double Radiotheodolite Techniques. Stephan P. Nelson. September 1973. 20 p. (COM-73-11932/9AS)

No. 66 The Motion and Morphology of the Dryline. Joseph T. Schaefer. September 1973. 81 p. (COM-74-10043)

No. 67 Radar Rainfall Pattern Optimizing Technique. Edward A. Brandes. March 1974. 16 p. (COM-74-10906/AS)

No. 68 The NSSL/WKY-TV Tower Data Collection Program: April-July 1972. R. Craig Goff and W. David Zittel. May 1974. 45 p. (COM-74-11334/AS)

No. 69 Papers on Oklahoma Thunderstorms, April 29-30, 1970. Stanley L. Barnes, Editor. May 1974. 147 p. (COM-74-11474/AS)

No. 70 Life Cycle of Florida Key's Waterspouts. Joseph H. Golden. June 1974. 147 p. (COM-74-11477/AS)

No. 71 **Interaction of Two Convective Scales Within a Severe Thunderstorm: A Case Study and Thunderstorm** Wake Vortex Structure and Aerodynamic Origin. Leslie R. Lemon. June 1974. 43 p. (COM-74-11642/AS)

No. 72 Updraft Properties Deduced from Rawinsoundings. Robert P. Davies-Jones and James H. Henderson. October 1974. 117 p. (COM-75-10583/AS)

No. 73 Severe Rainstorm at Enid, Oklahoma - October 10, 1973. L. P. Merritt, K. E. Wilk, and M. L. Weible. November 1974. 50 p. (COM-75-10583/AS)

No. 74 Mesonetwork Array: Its Effect on Thunderstorm Flow Resolution. Stanley L. Barnes. October 1974. 16 p. (COM-75-10248/AS)

No. 75 Thunderstorm-Outflow Kinematics and Dynamics. R. Craig Goff. December 1975. 63 p. (PB-250808/AS)

No. 76 An Analysis of Weather Spectra Variance in a Tornadic Storm. Philippe Waldteufel. May 1976. 80 p. (PB-258456/AS)

No. 77 Normalized Indices of Destruction and Deaths by Tornadoes. Edwin Kessler and J. T. Lee. June 1976. 47 p. (PB-260923/AS)

No. 78 Objectives and Accomplishments of the NSSL 1975 Spring Program. K. Wilk, K. Gray, C. Clark, D. Sirmans, J. Dooley, J. Carter, and W. Bumgarner. July 1976. 47 p. (PB-263813/AS)

No. 79 Subsynoptic Scale Dynamics As Revealed By The Use Of Filtered Surface Data. Charles A. Doswell III. December 1976. 40 p. (PB-265433/AS)

No. 80 The Union City, Oklahoma Tornado of 24 May 1973. Rodger A. Brown, Editor. December 1976. 235 p. (PB-269443/AS)

No. 81 Mesocyclone Evolution and Tornado Generation Within the Harrah, Oklahoma Storm. Edward A. Brandes. May 1977 28 p. (PB-271675/AS)

No. 82 The Tornado: An Engineering-Oriented Perspective. Joseph E. Minor, James R. McDonald, and Kishor C. Mehta. December 1977. 196 p. (PB-281860/AS)

No. 83 Spring Program '76. R. L. Alberty, J. F. Weaver, D. Sirmans, J. T. Dooley, and B. Bumgarner. December 1977. 130 p. (PB280745/AS)

No. 84 Spring Program '77. P. S. Ray, J. Weaver, and NSSL Staff. December 1977. 173 p. (PB-284953/AS)

No. 85 A Dual-Doppler Variational Objective Analysis as Applied to Studies of Convective Storms. Conrad L. Ziegler. November 1978. 116 p. (PB-293581/AS)

No. 86 Final Report on the Joint Doppler Operational Project (JDOP) 1976-78. Prepared by Staff of the National Severe Storms Laboratory, Environmental Research Laboratories; Weather Radar Branch, Air Force Geophysics Laboratory; Equipment Development Laboratory, National Weather Service; and Air Weather Service, United States Air Force. March 1979. 84 p. (PB80-107188/AS)

No. 87 An Analysis of the Clear Air Planetary Boundary Layer Wind Synthesized from NSSL's Dual Doppler-Radar Data. Myron I. Berger and R. J. Doviak. June 1979. 55 p. (PB-300865/AS)

No. 88 The Relationship of the 300-mb Jet Stream to Tornado Occurrence. Carolyn M. Kloth and Robert P. Davies-Jones. July 1980. 88 p.

☆ U. S. GOVERNMENT PRINTING OFFICE 1980 - 777-002/1210 Reg. 8